

Search for long-lived supersymmetric particles  
using displaced vertices and multiple jets  
in  $pp$  collisions at  $\sqrt{s} = 13$  TeV with the ATLAS detector

ATLAS 検出器での重心系エネルギー 13 TeV 陽子・陽子衝突データにおける  
ビーム衝突点から離れた崩壊点と複数のジェットを利用した  
長寿命な超対称性粒子探索

Graduate School of Science, Nagoya University  
High Energy Physics Laboratory

Moe Wakida

February 24, 2023



## Abstract

The Standard Model (SM) of particle physics describes all fundamental forces of electromagnetic, weak, and strong interactions, except for gravity in the universe. The behaviour of elementary particles predicted by the SM is in good agreement with the results of the experiments obtained so far. However, there are some problems that cannot be solved by the SM alone; the Higgs boson mass 125 GeV cannot be naturally derived and the dark matter cannot be formed from the particles in the SM. Supersymmetry (SUSY) could solve these problems. Also, SUSY possibly unifies the electroweak and strong interactions at a high energy scale.

SUSY particles have been searched for up to  $O(1)$  TeV at the Large Hadron Collider (LHC), but no SUSY particles have been found. A large parameter space for SUSY particles, which provides all above benefits, has been excluded. Therefore, I focused on the SUSY model, which solves the mass problem of the Higgs boson at least. I focused on the  $R$ -parity violating model. In this model, the lightest SUSY particles can decay to the SM particles. The coupling constants between SM and SUSY particles are predicted to be small due to proton decay constraints. Since regions with very small coupling constant have already been searched for in other analyses at the ATLAS experiment, this thesis focuses on the case where the coupling constant is  $O(10^{-4})$ – $O(10^{-3})$ . This case does not allow SUSY particles to form dark matter candidates, but the other two benefits can be kept.

This thesis presents a search for long-lived SUSY particles in events with displaced vertices and multiple jets using the  $139 \text{ fb}^{-1}$  of  $pp$  collision data collected at  $\sqrt{s} = 13 \text{ TeV}$  by the ATLAS detector at the LHC. Two signal processes are searched for, which are  $pp \rightarrow \tilde{g}\tilde{g}, \tilde{g} \rightarrow qq\tilde{\chi}_1^0 (\rightarrow qq\tilde{\chi}_1^0)$  and  $pp \rightarrow \tilde{\chi}_1^0\tilde{\chi}_1^\pm, \tilde{\chi}_1 \rightarrow qq\tilde{\chi}_1^0$ . The lightest electrowinos  $\tilde{\chi}_1$  have a long lifetime due to the small  $R$ -parity violating coupling. I focus on the models characterized by multiple jets and the decay vertex of the long-lived electrowikino being  $O(1)$ – $O(100)$  mm away from the interaction point, which is called displaced vertex. We established the analysis method using dedicated techniques to reconstruct the tracks derived from the long-lived electrowikino decay and the decay vertex of the electrowikino. A signal region (SR) is defined for each signal process. In SRs, at least one displaced vertex and multiple high momentum jets are required. The displaced vertex must be reconstructed from five or more tracks and the invariant mass calculated from the four-momenta of these tracks, obtained by assuming the pion mass for each track, must be larger than 10 GeV. The dominant background events are due to accidental reconstruction of displaced vertices by some sources. I established a new background estimation method and achieved accurate estimation. The new method estimates the background events inclusively using the relation between the number of accidentally reconstructed displaced vertices and the number of jets.

The number of observed events did not significantly exceed the background estimations in each SR. At 95% confidence level, the neutralino mass up to 1.58 TeV for lifetime of 0.1 ns is excluded. This analysis allows the search for the models in which the lightest electrowikino with lifetimes of 0.01 – 1 ns decays into light-flavour quarks, which has not been searched for to date.

# Contents

Chapter 1	Introduction	1
Chapter 2	Motivation	3
2.1	The problem of Standard Model . . . . .	3
2.1.1	Fine tuning problem of Higgs boson mass . . . . .	3
2.1.2	Dark matter . . . . .	4
2.2	Supersymmetry . . . . .	6
2.2.1	Benefit of supersymmetry . . . . .	7
2.2.2	Search results in Run 2 . . . . .	9
2.2.3	Target scenario . . . . .	10
Chapter 3	LHC-ATLAS experiment	16
3.1	The Large Hadron Collider . . . . .	16
3.2	The ATLAS detector . . . . .	16
3.2.1	Coordinate system at the ATLAS experiment . . . . .	17
3.2.2	Superconducting magnet . . . . .	18
3.2.3	Inner tracking detector . . . . .	19
3.2.4	Calorimeter . . . . .	20
3.2.5	Muon detector . . . . .	21
3.3	Trigger and data acquisition . . . . .	22
Chapter 4	Data and simulation samples	27
4.1	Data sample . . . . .	27
4.2	Simulation samples . . . . .	28
Chapter 5	Reconstruction and object definition	30
5.1	Standard track reconstruction . . . . .	30
5.1.1	Inside-out tracking . . . . .	30
5.1.2	Outside-in tracking . . . . .	31
5.2	Primary vertex reconstruction . . . . .	32
5.3	Displaced vertex reconstruction . . . . .	32
5.3.1	Large Radius Tracking . . . . .	32

5.3.2	Secondary vertex reconstruction . . . . .	34
5.4	Lepton reconstruction . . . . .	36
5.5	Jet reconstruction . . . . .	37
5.5.1	Calo jet . . . . .	37
5.5.2	Track jet . . . . .	40
5.6	Overlap removal . . . . .	41
Chapter 6	Event Selection . . . . .	42
6.1	Signal region definitions . . . . .	42
6.2	Event trigger and jet filter . . . . .	42
6.3	Jet selections . . . . .	43
6.4	DV selections . . . . .	45
6.4.1	Baseline DV selection . . . . .	45
6.4.2	DV-track selection . . . . .	46
6.4.3	Final DV selection . . . . .	47
6.5	Signal efficiencies . . . . .	48
Chapter 7	Background estimation . . . . .	53
7.1	Background classification . . . . .	53
7.2	Inclusive background estimation method . . . . .	54
7.2.1	Calculation of track jet-DV probability . . . . .	55
7.2.2	Estimation of the number of the background events in the SRs . . . . .	58
7.3	Uncertainties on background estimation . . . . .	60
7.4	Validation . . . . .	61
7.4.1	Validation in sideband regions of the SR . . . . .	62
7.4.2	Validation in the inside material regions . . . . .	62
7.4.3	Cross check with the independent background estimation method . . . . .	66
7.4.4	Additional systematic uncertainties from the validation results . . . . .	73
Chapter 8	Uncertainties . . . . .	75
8.1	Uncertainties from the track reconstruction efficiencies . . . . .	75
8.1.1	Calculation of the probability not to reconstruct tracks or DVs in data . . . . .	76
8.1.2	Propagation to the systematic uncertainty of the signal efficiency . . . . .	77
8.2	Jet uncertainties . . . . .	78
8.2.1	Uncertainties due to the jet energy scale and resolution uncertainties . . . . .	79
8.2.2	Jet response due to displacement . . . . .	79
8.3	Pile-up uncertainties . . . . .	83
8.4	Theoretical uncertainties . . . . .	84



---

Chapter 9	Results	86
9.1	Expected signal yields . . . . .	86
9.2	Observed yields . . . . .	86
Chapter 10	Discussion	90
10.1	Constraint for the focused RPV SUSY models . . . . .	90
10.2	Reinterpretation of the results . . . . .	91
10.2.1	Definition of acceptances . . . . .	93
10.2.2	Efficiencies . . . . .	95
10.2.3	Validation . . . . .	96
Chapter 11	Conclusion	105
Acknowledgments		107
References		108

# Chapter 1

## Introduction

The Standard Model (SM) of particle physics describes all fundamental forces of electromagnetic, weak, and strong interactions, except for gravity in the universe. The behaviour of elementary particles predicted by the SM is in good agreement with the results of the experiments obtained so far. However, there are some problems that cannot be solved by the SM alone; the Higgs boson mass 125 GeV cannot be naturally derived and the dark matter cannot be formed from the particles in the SM. Supersymmetry (SUSY) could solve these problems. SUSY is a symmetry between fermions and bosons. The higher-order quantum correction terms related to the unnatural derivation of the Higgs boson mass can be cancelled by SUSY. Also, in many SUSY models, the lightest and stable neutral SUSY particle can be a candidate for dark matter. In addition, SUSY also possibly unifies the electroweak and strong interactions at a high energy scale [1].

If the SUSY particles are expected to have masses in the  $O(1)$  TeV scale, they can be produced at the Large Hadron Collider (LHC) with center of mass energy of 14 TeV. The gluino (the super partner of the gluon), which has the largest cross section in the SUSY particles at  $pp$  collision [2], has been searched for up to 2.3 TeV by 2022 using  $139 \text{ fb}^{-1}$  data collected by the ATLAS detector, but it has not been found [3]. Many other SUSY particles have also been searched for up to about 1 TeV and have not been found [3]. From these results, a large parameter space for SUSY particles, which provides all of the above benefits, has been excluded [1].

Therefore, I focused on the SUSY model, which solves the mass problem of the Higgs boson at least. I focused on the  $R$ -parity violating model. If the  $R$ -parity is conserved, SUSY particles are produced in pairs from SM particles and do not decay to the SM particles only. If the  $R$ -parity is violated, the lightest SUSY particles can decay to the SM particles only, and the coupling constants between SM and SUSY particles are predicted to be small due to the constraint from the proton decay [4], and the lightest SUSY particles have a long lifetime. If the lifetimes of the long-lived SUSY particles are so long that the flying distance exceeds the ATLAS detector, the SUSY particle is not observed and is detected as a missing energy. They should be searched for by the analysis using missing energy. However, the fact that no SUSY particles were found in these analyses suggests that the SUSY particles are "long-lived but decay inside the ATLAS detector". This case does not allow SUSY particles to form dark matter candidates, but the other two benefits can be kept [5].

Most analysis methods of the ATLAS experiment assume that the final state particles originate from

regions about  $O(1)$  mm from the  $pp$  interaction point. Therefore, in order to search for long-lived SUSY particles decaying within the ATLAS detector, dedicated methods are needed to reconstruct the charged particle tracks originating from the SUSY particles and the decay vertices of the SUSY particles which decay at a distance of about  $O(10)–O(100)$  mm from the interaction point. Also, the dominant background events are due to accidental reconstruction of displaced vertices. The estimation method for these background events need to be established. We have established the analysis method using the special track and vertex reconstruction techniques, as well as a new background estimation method to search for the long-lived SUSY particle. This thesis is organized as follows:

**Chapter 2 :** Motivation of SUSY and search results to date, and target model in this analysis

**Chapter 3 :** Overview of the LHC, the ATLAS detector, and data acquisition at ATLAS experiment

**Chapter 4 :** The data and simulation samples used in the analysis

**Chapter 5 :** Event reconstruction including the special reconstruction and object definition

**Chapter 6 :** Event selection requirements and the signal efficiency

**Chapter 7 :** Background classifications and the estimation method

**Chapter 8 :** Uncertainties for simulation samples

**Chapter 9 :** Results of this search

**Chapter 10 :** Discussion of interpretation of results for target signal and reinterpretation methods for models with similar characteristics

**Chapter 11 :** Conclusion

## Chapter 2

# Motivation

### 2.1 The problem of Standard Model

The Standard Model (SM) of particle physics is the theory describing all fundamental forces (electromagnetic, weak and strong interactions) except for gravity in the universe and classifying all known elementary particles as shown in Figure 2.1. It was established theoretically in the 1970s and has been verified by many experiments. In 2012, both of the ATLAS and CMS experiments discovered the Higgs boson, the last undiscovered particle of the SM [6, 7]. The SM is successful in describing the phenomena of particles and their interactions. For example, the theoretically calculated values of the total production cross sections in  $pp$  collisions for the SM processes are in perfect agreement with the cross sections measured with the ATLAS detector as shown in Figure 2.2.

However, the SM is not a perfect theory because there are some problems that cannot be solved by the SM. For example,

- SM cannot derive Higgs boson mass naturally (Called "fine tuning problem" of Higgs boson mass)
- No dark matter candidates in the SM particles

#### 2.1.1 Fine tuning problem of Higgs boson mass

The Higgs boson is the particle with spin 0 and the measured mass of  $125.09 \pm 0.21(\text{stat}) \pm 0.11(\text{syst})$  [10]. This mass is much lighter than the Planck scale ( $10^{19}$  GeV). Although, fermions and gauge bosons also have masses lighter than Planck scale, they are allowed to have such light masses due to chirality conservation and gauge invariance, respectively [11, 12]. There are no symmetry in the SM that allows particles with spin 0 to have light masses. The Higgs boson is the only particle with spin 0, and the reason why the Higgs boson mass ( $O(10^2)$  GeV) is much smaller than the Planck scale is an open question that cannot be explained by the SM alone.

The electrically neutral part of the Higgs field in the Standard Model is a complex scalar  $H$  with a classical potential being the [1]

$$V = m_H^2 |H|^2 + \lambda |H|^4 \quad (2.1)$$

In the SM, the vacuum expectation value for  $H$  must not vanish at the minimum of the potential. It

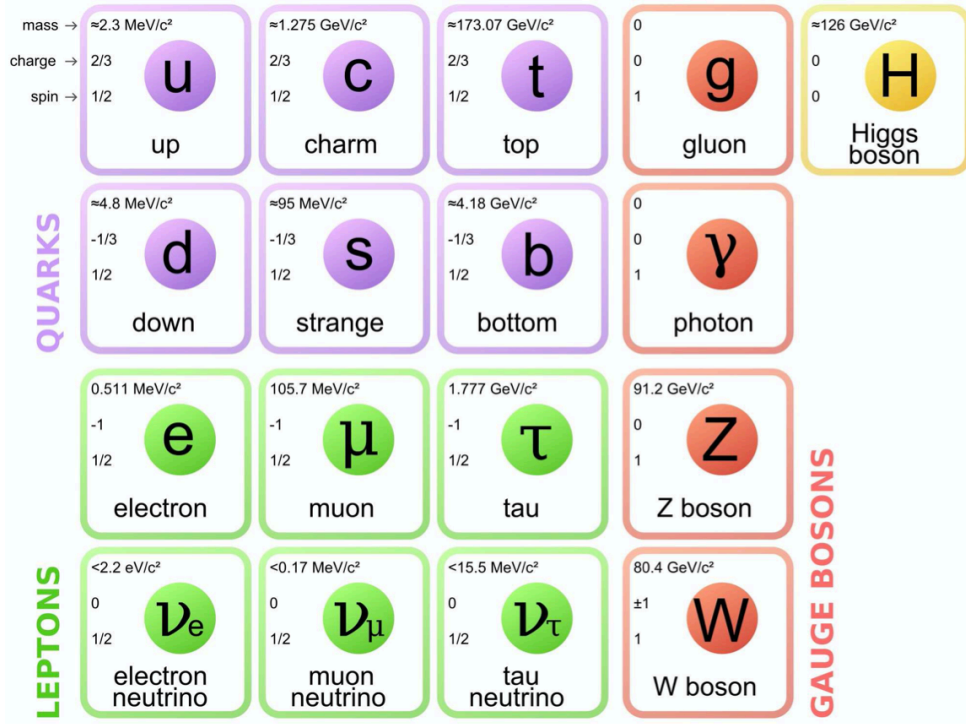


**Figure 2.1:** SM particles [8]. Three generations of six types of quarks and leptons make up matter, and gauge bosons mediate the strong ( $g$ ), electromagnetic ( $\gamma$ ) and weak forces ( $Z, W$ ). The Higgs boson is the mass origin of elementary particles.

occurs if  $m_H^2 < 0$  and  $\lambda > 0$ , the minimum of the potential is  $\sqrt{\frac{-m_H^2}{2\lambda}}$ . The discovered Higgs boson mass of 125 GeV implies  $\lambda = 0.126$  and  $m_H^2 = -(92.9 \text{ GeV})^2$ , assuming the Standard Model is correct as an effective field theory. The  $m_H^2$  receives quantum corrections due to virtual effects from all particles and other phenomena that couples directly or indirectly to the Higgs field. For example, if the Higgs field couples to the Dirac fermion  $f$  in terms of the Lagrangian  $-\lambda_f H f f$ , the correction from the loop containing fermion shown in Figure 2.3 is

$$\Delta m_H^2 = -\frac{|\lambda_f|^2}{8\pi^2} \Lambda_{UV}^2 + \dots, \quad (2.2)$$

where  $\Lambda_{UV}$  is the ultraviolet momentum cutoff used to regulate the loop integral, and it is interpreted as the energy scales to which the Standard Model can be applied. The largest correction among SM particles comes when  $f$  is the top quark with  $\lambda_f \approx 0.94$ . If the SM applies to the Planck scale, the scale of  $\Lambda_{\text{cut-off}}$  should be the order of the Planck scale, and the tuning of magnitude larger than 30 order is required to derive the required value of  $m_H^2 \approx (92.9 \text{ GeV})^2$ . This unnatural tuning is called the "fine tuning problem".

### 2.1.2 Dark matter

Cosmological observations indicate the existence of dark matter. An example is the measurement of the galaxy rotation curves [13]. It measures the rotational velocity, which is the orbital velocity of

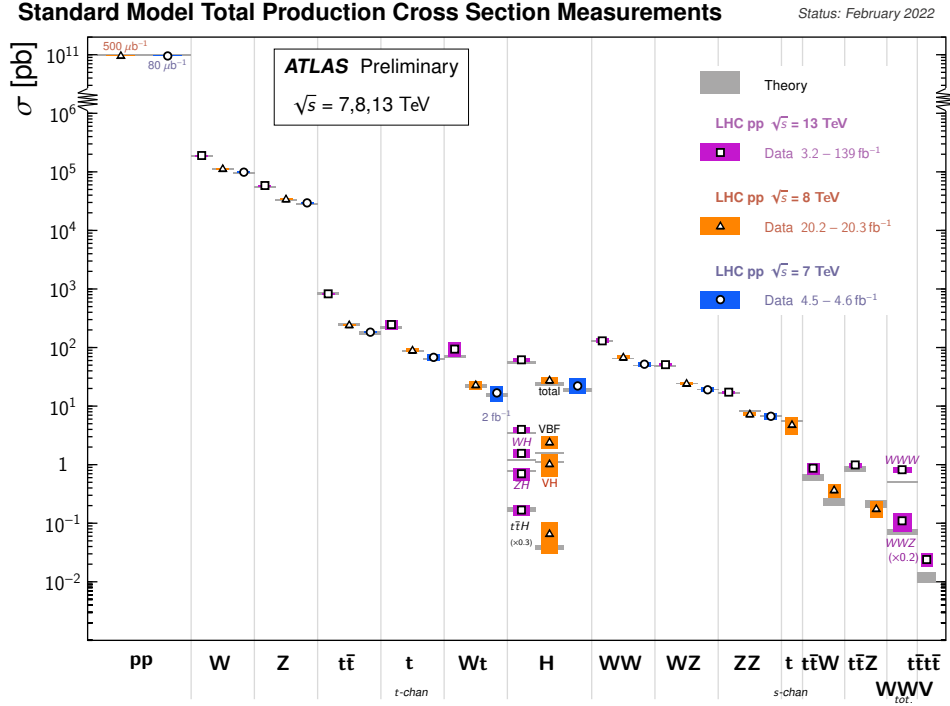


**Figure 2.2:** Summary of SM cross section measurements with the ATLAS detector [9].

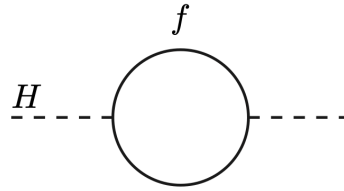


**Figure 2.3:** One-loop quantum corrections to the Higgs squared mass parameter  $m_H^2$ , due to a Dirac fermion  $f$  [1].

the stars and gas in the galaxy as a function of the distance from the centre of the galaxy to the orbiting object ( $R$ ). In general, the rotational velocity is expected to follow  $V(R) \propto \frac{1}{\sqrt{R}}$  in the outer regions of the galaxy, but the measurement results show that the rotational velocity becomes more constant as increasing  $R$  as shown in Figure 2.4. This means that there are massive objects that cannot be seen because it is not luminous. Such a massive object is called "Dark Matter" (DM) and it is predicted to occupy 26.8% of the universe [14].

There are several DM candidates, which can be broadly divided into candidates from particle physics and those from astrophysics. For candidates from particle physics, they must have the following properties to explain the observations:

- They interact only weakly with other particles.
- They are stable.
- They have finite mass.

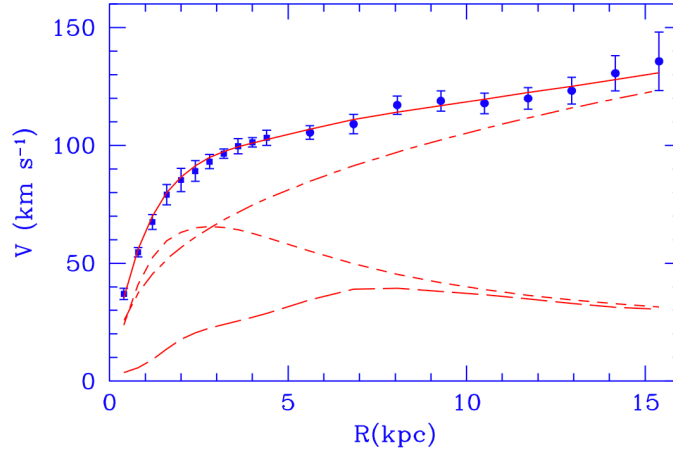


**Figure 2.4:** M33 rotation curve (points) compared with the best fit model (continuous line) [13]. The y-axis  $V$  is the rotational velocity of an object on a stable Kepler orbit with a radius  $R$  around the galaxy. Also shown the halo contribution (dashed- dotted line), the stellar disk (short dashed line) and the gas contribution (long dashed line).

Only neutrinos have these features in the SM particles, but if neutrinos are the main components of DM, no large-scale structure in the Universe is created due to too light mass [15]. Therefore, the beyond the standard model (BSM) particles are needed as dark matter candidates.

## 2.2 Supersymmetry

Supersymmetry (SUSY) [16, 17, 18, 19, 20, 21], which is a symmetry between fermions and bosons, is one of the promising solutions of the above problems. The Minimal Supersymmetric Standard Model (MSSM), which introduces minimal particles and degrees of freedom into SM [22, 23], is described here for simplicity.

The bosonic state is transformed to the fermionic state by the supersymmetry transformation  $Q$ , and the fermionic state is transformed to the bosonic state.

$$Q|\text{fermion}\rangle = |\text{boson}\rangle, \quad Q|\text{boson}\rangle = |\text{fermion}\rangle. \quad (2.3)$$

This introduces the partners of all the SM particles (super partners) as shown in Figure 2.5. The super partners of the SM fermions are called "sfermions" and have spin 0. The super partners of the quarks and leptons are called "squarks" and "sleptons", respectively. The super partners of the SM gauge bosons and Higgs bosons are called "gauginos" ("gluinos", "binos", and "winos") and "higgsinos" and have spin 1/2. The MSSM introduces two Higgs doublets and predicts five Higgs bosons. They are CP even neutral Higgs bosons ( $h$  and  $H$ ), a CP odd neutral Higgs boson ( $A$ ) and charged Higgs bosons ( $H^\pm$ ). The charged gauginos ( $\tilde{W}^\pm$ ,  $\tilde{H}^\pm$ ) are mixed and give two mass eigenstates, called "charginos" and denoted as  $\tilde{\chi}_1^\pm$  and  $\tilde{\chi}_2^\pm$  in the order from the lighter to the heavier. The neutral gauginos ( $\tilde{W}^0$ ,  $\tilde{B}^0$ ,  $\tilde{h}$ ,  $\tilde{H}$ ) are mixed and give four mass eigenstates, called "neutralinos", and denoted as  $\tilde{\chi}_1^0$ ,  $\tilde{\chi}_2^0$ ,  $\tilde{\chi}_3^0$ , and  $\tilde{\chi}_4^0$  in the order from the lightest to the heaviest. Charginos and neutralinos together are called

"electrowikinos".

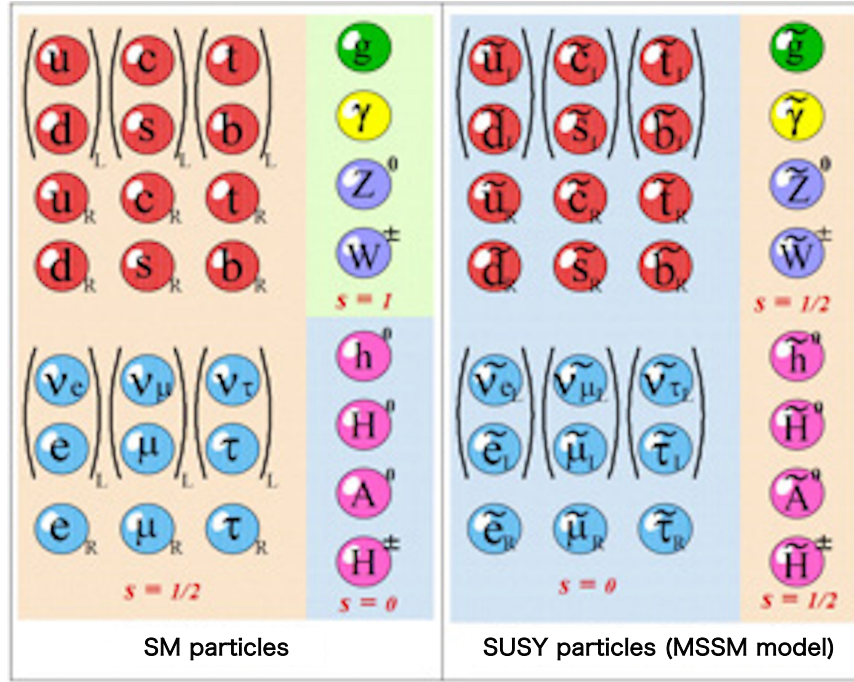


**Figure 2.5:** The SM particles (Left) and the SUSY particles (Right) [24]. It is expected that SUSY particles with 1/2 different spin from the SM particles will exist corresponding to each SM particle.

### 2.2.1 Benefit of supersymmetry

SUSY provides elegant solutions to the problems of Standard Model described in Section 2.1.

#### Fine tuning problem of Higgs boson mass

Since supersymmetry introduces two complex scalar fields for each Standard Model fermion, the correction in Eq. (2.2) cancel if the SM particles and the corresponding SUSY particles have the same masses [1]. However, the masses of the SUSY particles cannot be the same as those of the SM particles, since no SUSY particles have been observed on the same energy scales as the SM particles. Thus, it is clear that supersymmetry is broken in the vacuum state. Therefore, we are led to consider the soft breaking of supersymmetry where the effective Lagrangian of the MSSM can be written as follows

$$L = L_{\text{SUSY}} + L_{\text{soft}}, \quad (2.4)$$

where  $L_{\text{SUSY}}$  includes all gauge and Yukawa interactions and preserves supersymmetry invariance, and  $L_{\text{soft}}$  breaks supersymmetry but includes only mass terms and coupling parameters with positive mass dimensions. If the largest mass scale associated with the  $L_{\text{soft}}$  term is denoted  $m_{\text{soft}}$ , non-supersymmetric corrections to the square of the Higgs mass should generally be the form [1]

$$\Delta m_H^2 = m_{\text{soft}}^2 \left[ \frac{\lambda}{16\pi^2} \ln(\Lambda_{\text{UV}}/m_{\text{soft}}) + \dots \right]. \quad (2.5)$$



To solve the fine tuning problem, the  $m_{\text{soft}}$ , and therefore mass of at least the lightest SUSY particle should not greatly exceed the TeV scale.

## Dark matter

The lightest neutralino  $\tilde{\chi}_1^0$ , which can be stable under an assumption of "R-parity" conservation, is a good candidate for the DM. The mass of the  $\tilde{\chi}_1^0$  is implied to be in the range  $O(10) - O(1000)$  GeV, considering the relic density of the DM.

R-parity conservation is introduced from the constraint on the proton decay not observed. If the R-parity is conserved, SUSY particles are produced in pairs from SM particles and do not decay to the SM particles only. If the R-parity is violated, proton decay can be occurred easily by SUSY, for example, via  $p \rightarrow e^+ \pi^0$  as shown in Figure 2.6. However, it is not observed until now. The Super-Kamiokande experiment has set the upper limit of the proton lifetime to be  $\tau_p > 1.6 \times 10^{34}$  years [4]. From this results, R-parity conservation was introduced to prevent the process of SUSY particles being made from only SM particles and decaying to only SM particles. In that case, the lightest neutralino is stable.

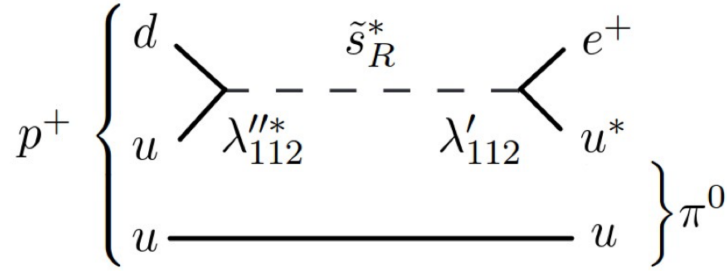


**Figure 2.6:** Diagram of the  $p \rightarrow e^+ \pi^0$  decay via SUSY particle  $\tilde{s}_R^*$  without any conservation related to lepton- and baryon-number.  $\lambda$  represents the coupling constant between SM and SUSY particles.

## Grand unification

SUSY also has an important benefit of unifying the electroweak and strong interactions at a high energy scale. The theory that unifies these interactions is called the Grand Unified Theory (GUT).

The SM is a  $SU(3) \times SU(2) \times U(1)$  gauge theory. The coupling constants  $\alpha_i(Q)$  ( $i = 1, 2, 3$ ) follow a renormalization group equation (RGE) that depends on the renormalization group energy scale  $Q$ . The RGE is described as follows [25]:

$$\frac{d\alpha_i(Q)}{d \ln Q} = -\frac{b_i}{2\pi} \alpha_i(Q)^2, \quad (2.6)$$

where  $b_i$  are the coefficients obtained from the loop calculations that contribute to each gauge boson. The coupling constants are described as follows by solving Eq. (2.6):

$$\frac{1}{\alpha_i(Q)} = \frac{1}{\alpha_i(m_W)} + \frac{b_i}{2\pi} \ln\left(\frac{Q}{m_W}\right) + \dots \quad (2.7)$$

In the case of the  $SU(5)$  model without SUSY, the three coupling constants are not unified as shown in the black lines of Figure 2.7. On the other hand, if the SUSY particles are considered in Eq. (2.7) and the mass is assumed to be  $O(1)$  TeV, these particles contribute to  $b_i$  to change the coupling constants, and the unification of the three coupling constants is allowed on the  $O(10^{15-16})$  GeV energy scale as shown in the red and blue lines of Figure 2.7. To achieve GUT, the gaugino masses are constrained to about  $O(1)$  TeV.

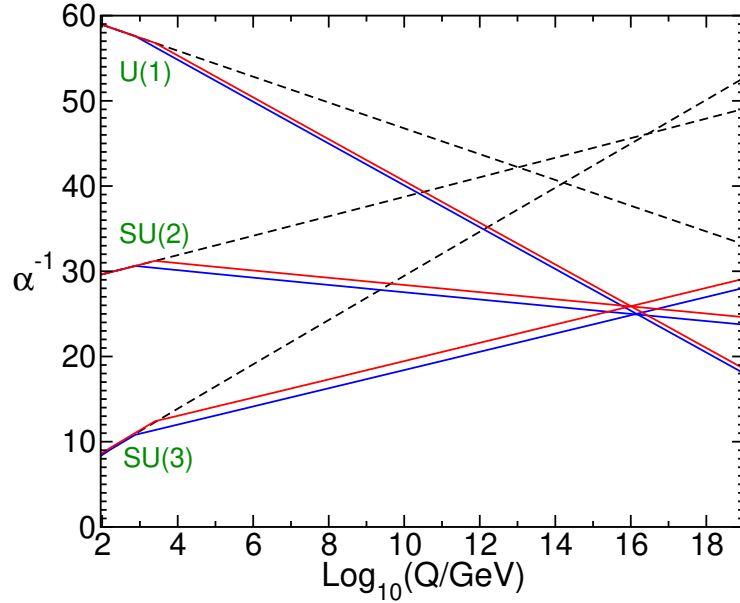


**Figure 2.7:** Inverse gauge couplings ( $\alpha^{-1}$ ) as a function of energy scale ( $Q$ ) [1]. Black dotted lines show ones with considering only the SM particles. Red and blue lines show ones with introducing SUSY particles which gaugino mass of 750 GeV and 2.5 TeV, respectively.

### 2.2.2 Search results in Run 2

The SUSY particles have been searched directly in several experiments at LEP, Tevatron, and LHC. Figure 2.8 shows the summary of the searches for SUSY particles at the ATLAS experiment by March 2022. The gluino with the largest cross section in the  $pp$  collision has been searched for up to 2.3 TeV. The squark with next largest cross section has also been searched for up to 1.85 TeV, and the electrowikino had been searched for up to 1.06 TeV. The searches for these require an increase in collision energy.

On the other hand, the search in phase space which has not been explored so far has become more important. Unexplored phase space refers to the region where the mass difference between  $\tilde{\chi}_1$  and  $\tilde{\chi}_2$  is small and they are compressed, or where the SUSY particles are long-lived. The search in regions where the mass is compressed is limited due to a huge number of low-momentum particles produced at the ATLAS experiment. On the other hand, the search in regions where the SUSY particle is long-lived has not been explored due to the need for dedicated reconstruction techniques. There are some cases where SUSY particles have a long lifetime:

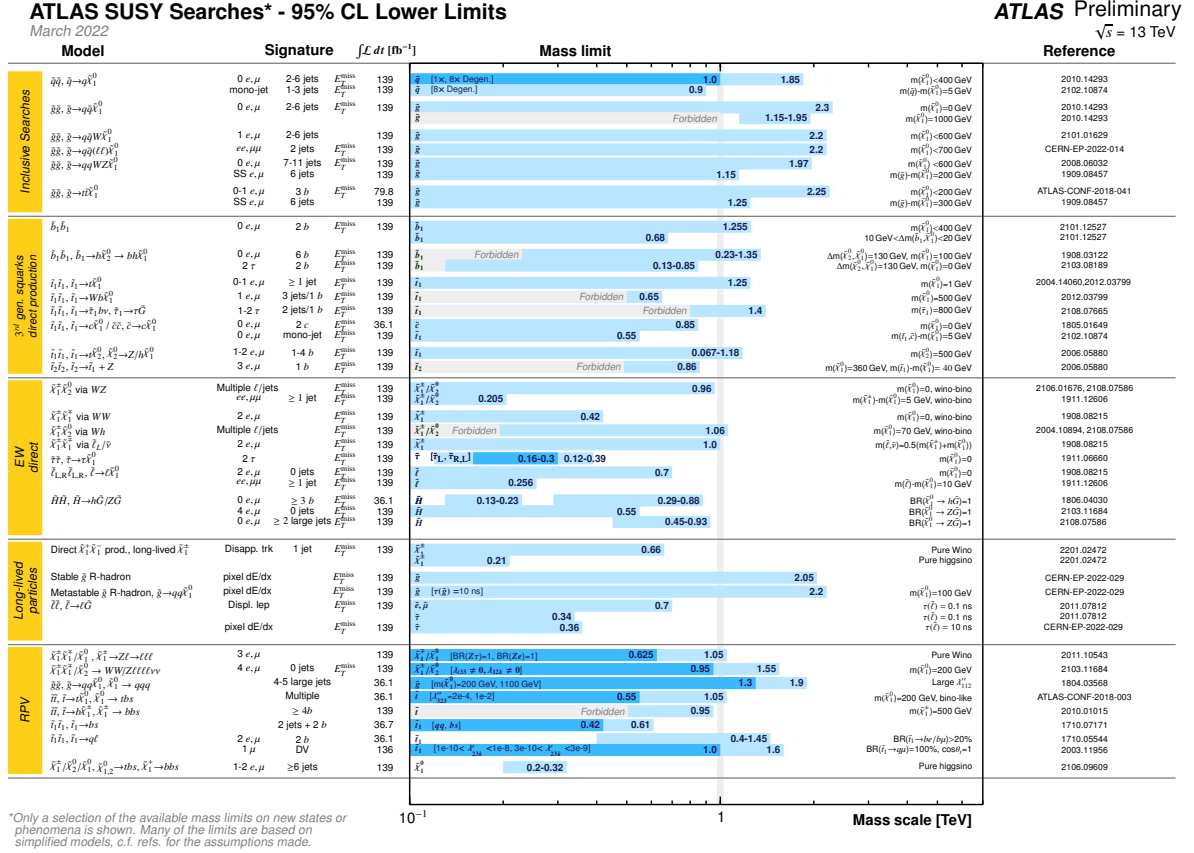


**Figure 2.8:** The summary of SUSY particle searches at the ATLAS experiment by March 2022 [3]. Exclusion mass limits for each SUSY particle are shown for each decay process, search signature and statistic.

- Mediator particles are heavy
- Small mass difference between particles before and after decay
- Small coupling constant

### 2.2.3 Target scenario

Based on the results of the searches to date, a large parameter space for the SUSY models which provide all the three benefits described in Section 2.2.1 was excluded. This thesis focuses on the SUSY model which breaks R-parity (R-parity violating: RPV) with small coupling constant between SM particles and SUSY particles [5]. In this model, the SUSY particles are not dark matter candidates, while the benefits for the fine tuning problem of Higgs boson mass and the grand unification can be kept.

### R-parity violating scenario

No observation of the proton decay is a good motivation for the R-parity conservation. However, if the mass of the involved SUSY particle is heavy or lepton- or baryon-number are violated individually, relatively large proton lifetime is obtained [5]. The terms related to RPV in the MSSM Lagrangian

are

$$L_{\Delta L, B=1} = \frac{1}{2} \lambda^{ijk} L_i L_j \bar{e}_k + \lambda'^{ijk} L_i Q_j \bar{d}_k + \mu'^i L_i H_u + \frac{1}{2} \lambda''^{ijk} \bar{u}_i \bar{d}_j \bar{d}_k, \quad (2.8)$$

where the  $i, j, k$  are generational indices,  $L$  is the leptonic  $SU(2)$  doublet,  $e$  is the leptonic  $SU(2)$  charged doublet,  $Q$  is the quark  $SU(2)$  doublet,  $u$  ( $d$ ) is the up (down) type quark singlet,  $H$  is the Higgs doublet, and  $\lambda$ ,  $\lambda'$ ,  $\mu'$  ( $\lambda''$ ) are lepton (baryon) violating couplings. Examples of each interaction are shown in Figure 2.9.

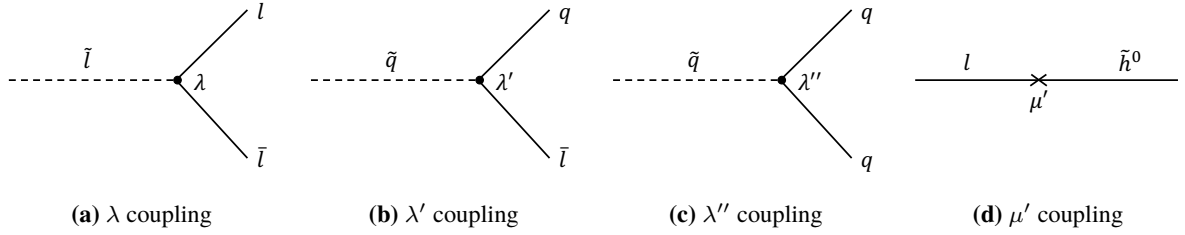


**Figure 2.9:** Examples of RPV interaction are illustrated. (a) shows an example of the  $\lambda$  coupling, where a slepton decays to the lepton pair. (b) shows an example of the  $\lambda'$  coupling, where a squark decays to the quark and lepton. (c) show an example of the  $\lambda''$  coupling, where a squark decays to the quark pair. (d) shows the mixes the lepton and Higgs superfield with  $\mu'$ .

The width of proton decay is written as

$$\Gamma_{p \rightarrow e^+ \pi^0} \sim m_{\text{proton}}^5 \sum_{i=2,3} |\lambda'^{11i} \lambda''^{11i}|^2 / m_{\tilde{d}_i}^4. \quad (2.9)$$

The problem with the proton decay can be avoided if the masses of the involved SUSY particles ( $m_{\tilde{d}}$ ) are heavy, or if one of the couplings of the  $\lambda'$  or  $\lambda''$  is small or 0.

## Search for RPV SUSY model at the ATLAS experiment

When the RPV coupling is small, the lifetime of the lightest SUSY particles is long. In the search at the ATLAS experiment, if the lifetime of the neutral SUSY particle is longer than 10 ns, the neutral SUSY particles decay outside the calorimeter and are detected as missing energy. Figure 2.10 shows the search results for the RPV SUSY particles using multiple jets and missing energy at the ATLAS experiment. In particular, the search for the SUSY particles with lifetimes below 1 ns is not possible with the analysis using missing energy.

In the ATLAS experiment, the analysis methods to search for long-lived SUSY particles in decay modes involving the  $\lambda$  and  $\lambda'$  couplings in Eq. (2.8) have already been established. Analyses using a decay vertex of the lightest SUSY particles and leptons have excluded the mass and lifetime of the lightest SUSY particles up to 1.3 TeV and 0.1 ns for the decay mode involving the  $\lambda$  coupling [27], and up to 1 TeV and 0.01 ns for the decay mode involving the  $\lambda'$  coupling [28]. This analysis searched for long-lived SUSY particles in decay modes involving the  $\lambda''$  coupling using the decay vertex of the long-lived SUSY particles and multiple jets. This analysis does not use objects suitable for selecting

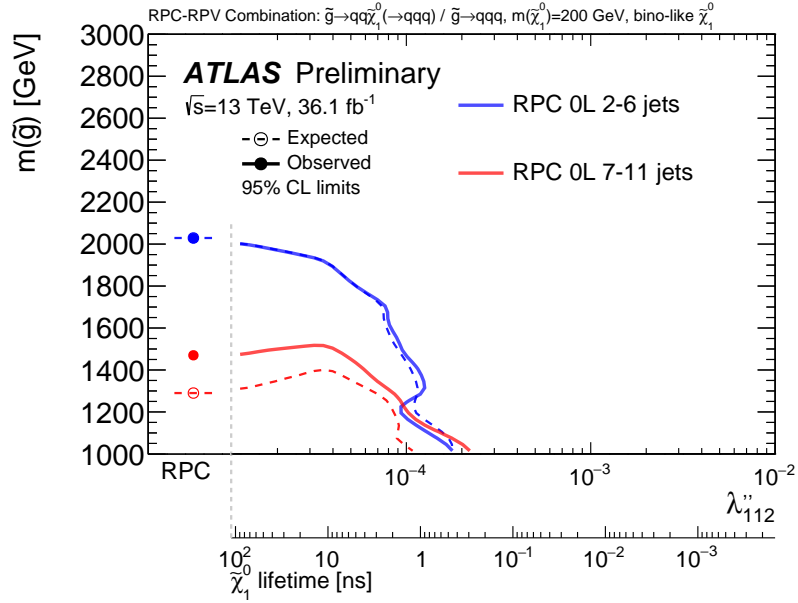


**Figure 2.10:** The results of search for RPV SUSY using multiple jets and missing energy [26]. The blue line shows the result using two to six jets final state, and the red curve shows the result using seven to eleven jets final state.

specific events such as the events including leptons; it is more difficult to estimate the number of background events from events containing the large number of jets produced from proton-proton collisions.

## Target signal

This thesis targets small values of the  $\lambda''$  coupling, assuming all other RPV couplings to be exactly zero. Several low- and intermediate-energy experimental observations constrain the value of the RPV couplings to be small [29, 30]. This naturally leads to suppression of the decay processes and can give rise to long-lived SUSY particles. A nonzero  $\lambda''$  coupling allows the electroweakinos to decay into three quarks via a decay of  $\tilde{\chi} \rightarrow q\bar{q}(\rightarrow qq)$ .

The diagrams of target signal models are shown in Figure 2.11. In the gluino pair production model, shown in Figure 2.11(a), pairs of gluinos  $\tilde{g}$  are produced. Each  $\tilde{g}$  promptly decays with a 100% branching ratio to a SM quark-antiquark pair and a neutralino  $\tilde{\chi}_1^0$ . The electroweakino pair production model, shown in Figure 2.11(b), considers the associated production of the lightest charged and neutral electroweakinos, i.e.  $\tilde{\chi}_1^\pm \tilde{\chi}_1^0$ ,  $\tilde{\chi}_1^+ \tilde{\chi}_1^-$ ,  $\tilde{\chi}_2^0 \tilde{\chi}_1^0$  and  $\tilde{\chi}_1^\pm \tilde{\chi}_2^0$ , assuming pure-higgsino states. The electroweakinos in both models decay to three quarks with a 100% branching ratio via the  $\lambda''$  couplings. The target lifetimes of neutralino and chargino are  $O(0.01) - O(1)$  ns and they correspond to the coupling constant  $\lambda''^{112}$  of the  $O(10^{-4}) - O(10^{-3})$ .

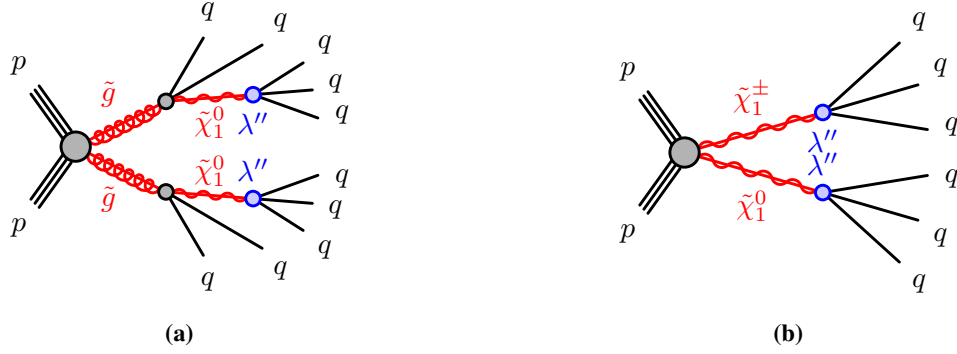


**Figure 2.11:** Diagrams of target benchmark models: (a) the gluino pair ( $\tilde{g}\tilde{g}$ ) production model, in which each gluino decays into a pair of quarks and a long-lived neutralino ( $\tilde{\chi}_1^0$ ), and (b) the electroweakino pair ( $\tilde{\chi}_1^\pm \tilde{\chi}_1^0$ ) production model, in which the  $\tilde{\chi}_1^\pm$  and  $\tilde{\chi}_1^0$  decay to three quarks via the RPV coupling  $\lambda''$ .

### Signal production and decay topology in $pp$ collisions

The LHC is a proton-proton collider. In  $pp$  collisions, particles are produced from the interaction between the quarks and gluons which constitute the proton. The production cross section for a particular process in the  $pp$  collision can be written as follows [31]:

$$\sigma_{pp \rightarrow X} = \sum_{i,j} \int dx_1 dx_2 f_i(x_1, \mu_F^2) f_j(x_2, \mu_F^2) \hat{\sigma}_{ij \rightarrow X}(x_1 p_1, x_2 p_2, \mu_F^2, \mu_R^2, \alpha(\mu_R^2)), \quad (2.10)$$

where  $f_{i(j)}(x_{1(2)}, \mu_F^2)$  is the parton distribution function (PDF) for the partons  $i, j = q, \bar{q}, g$  and  $\hat{\sigma}_{ij \rightarrow X}$  is the cross section between the partons of  $i$  and  $j$ . The PDF is defined as the probability density for finding a particle with a certain longitudinal momentum fraction  $x$  at an energy scale  $\mu_F$ . The  $\mu_F$  is called the QCD factorization factor and represents the energy scale at the boundary between perturbative QCD and non-perturbative QCD. Because of the inherent non-perturbative nature of partons which cannot be observed as free particles, parton densities cannot be calculated using perturbative QCD. Therefore, PDFs are determined by measurement of the deep inelastic scattering experiments. An example of the PDF is shown in Figure 2.12. On the other hand, the cross section  $\hat{\sigma}_{ij \rightarrow X}$  is calculable by the QCD and electroweak theories. It is calculated from a function of the momentum  $x_1 p_1 (x_2 p_2)$  of parton  $i(j)$ ,  $\mu_F$ , the QCD renormalization factor  $\mu_R$ , and the QCD coupling constant  $\alpha$ .  $\mu_R$  is the scale of the renormalization to avoid divergence of perturbation calculations.

Figure 2.13 shows the illustration of the signal production and decay process. Particles with color transit into colorless hadrons due to the "confinement" effect of strong interactions in the QCD theory (called hadronization). Hadronized quarks and gluons are detected as jets. The QCD process allows gluons (which are hadronized into jets) to be added to initial and final state particles. These additional processes are called initial state radiation (ISR) and final state radiation (FSR). Apart from the hard process of two-parton collisions, many other hadronic processes occur in a collision event. These processes are called underlying events (UEs) and include two types of processes of beam remnants and multi-parton soft QCD interactions (pile-up events). The pile-up events also include soft QCD

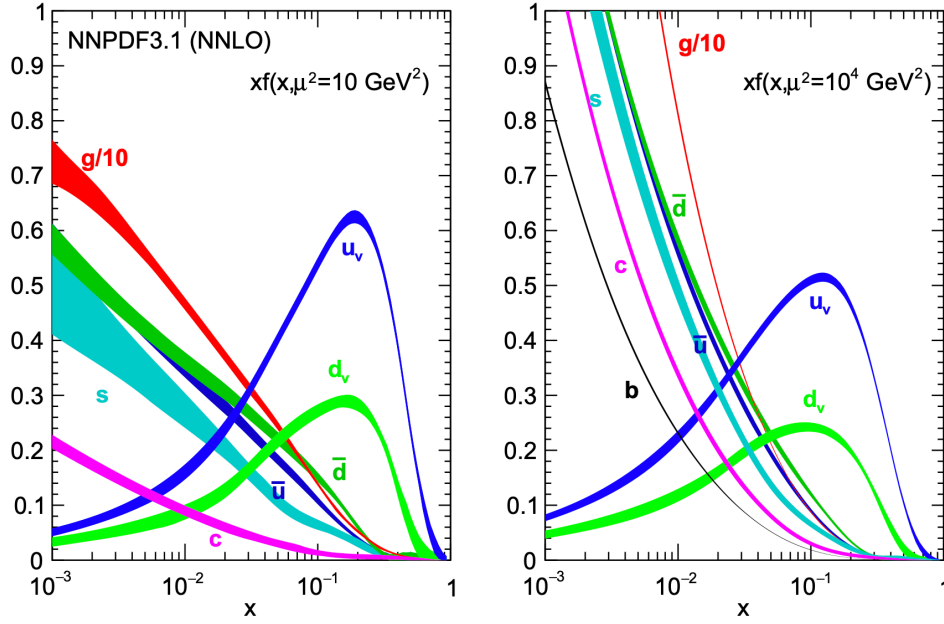


**Figure 2.12:** The NNPDF3.1 NNLO PDFs, evaluated at  $\mu_F^2 = 10 \text{ GeV}^2$  (left) and  $\mu_F^2 = 10^4 \text{ GeV}^2$  (right) [32].

interactions of partons contained in different protons.

The above process results in a large number of jets in the final state. Generally, a jet from heavy particle decay has a large momentum. In addition, in the region of  $O(0.01) - O(1)$  ns lifetime of neutralinos targeted in this analysis, neutralinos fly  $O(1) - O(100)$  mm and decay. This flight length is the distance, at which decays inside the inner detector and the decay point is observed as a displaced vertex (DV), a decay point that appears at a distance from the interaction point as shown in Figure 2.14. Therefore, this analysis focuses on events involving DVs and multiple high-momentum jets to search for long-lived SUSY particles.

In this search, the background events are the multiple jets events including DVs created accidentally. Background events are discussed in detail in Chapter 7.

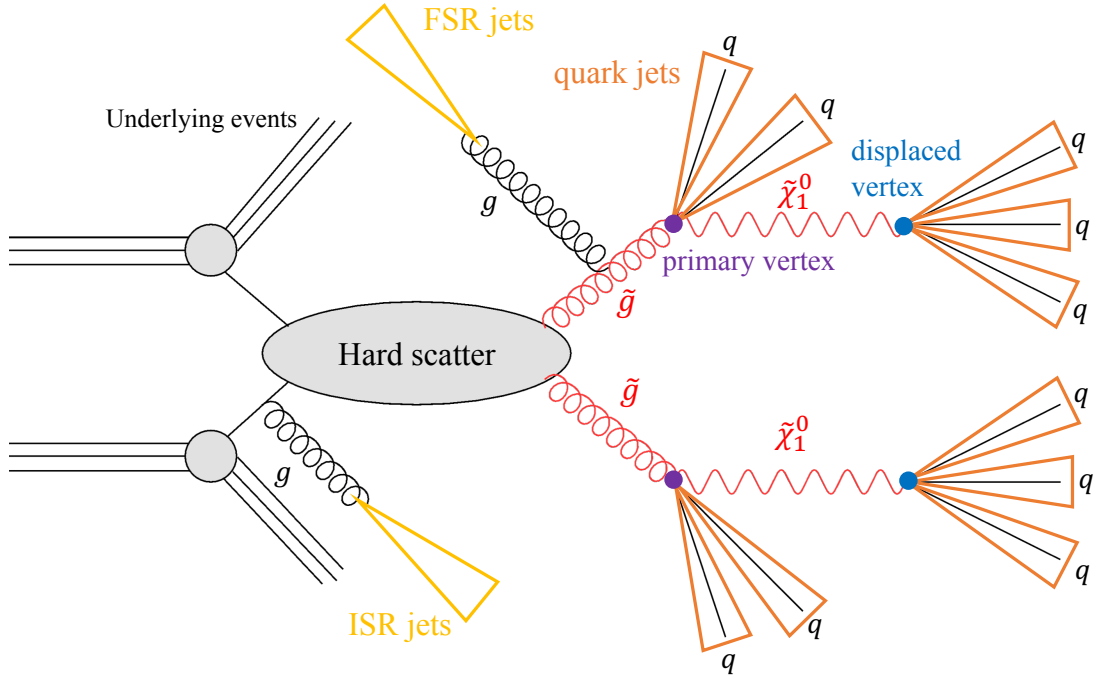


**Figure 2.13:** The illustration of the production and decay process for the gluino pair production model (Figure 2.11(a)). Gluino ( $\tilde{g}$ ) pairs are produced by hard scattering. The quarks ( $q$ ) and gluons ( $g$ ) are hadronized and are detected as jets. Neutralinos ( $\tilde{\chi}_1^0$ ) are not detected because they have no charge and only weak interactions.

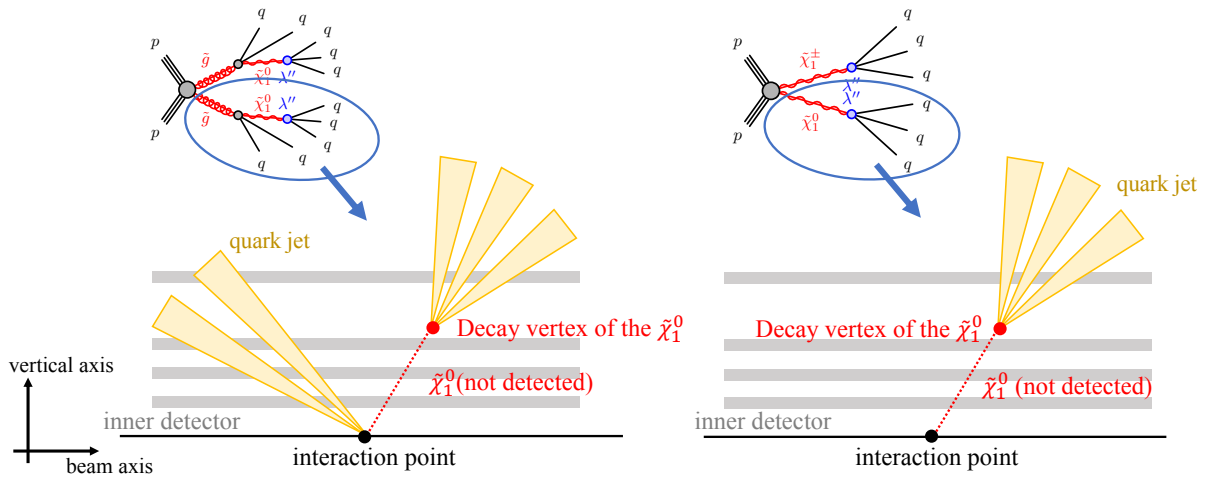


**Figure 2.14:** Event topology of the signal models. ISRs, FSRs, and UEs are not included in the figure, and only the topologies of the circled half of each diagram are shown.



## Chapter 3

# LHC-ATLAS experiment

### 3.1 The Large Hadron Collider

The LHC is a two-ring-superconducting-hadron accelerator and collider installed in the 26.7 km tunnel located 100 m underground in the European Organization for Nuclear Research (CERN) located across the border between Switzerland and France (Figure 3.1) [33]. Protons accelerated to a maximum of 7 TeV collide at a frequency of 40 MHz with a center-of-mass energy of 14 TeV to directly create heavy particles, enabling precise measurements of the Higgs boson and search for new particles. The LHC operation started in 2010 and has operated at a center-of-mass energy of 7 TeV in 2011, 8 TeV in 2012, and 13 TeV during 2015–2018.

Acceleration of protons is carried out step by step. First, LINAC2 extracts protons from hydrogen atoms and accelerates them to 50 MeV. After that, they are accelerated to 1.4 GeV by Proton Synchrotron Booster (Booster), 50 GeV by Proton Synchrotron (PS), 450 GeV by Super Proton Synchrotron (SPS), and finally maximum 7 TeV by LHC.

Figure 3.2 shows the production cross-section of each particle at the LHC. Of all the particles produced from proton-proton collisions, only about  $1/10^{10}$  are Higgs bosons. SUSY particles, which have not yet been discovered, are thought to have smaller production cross-sections. In the ATLAS experiment, it is impossible to store the data of all the events generated at 40 MHz, and thus a trigger system that selects only interesting events is important (Section 3.3).

### 3.2 The ATLAS detector

The ATLAS detector is a cylindrical general-purpose detector with a height of 25 m, a total length of 44 m, and a weight of 7,000 tons, which was installed at one of the interaction points of the LHC (Figure 3.3). From the inside, the inner tracking detector, the electromagnetic calorimeter, the hadron calorimeter, and the muon detector cover the interaction point in that order. A magnetic field of 2 T is applied by a solenoid magnet and 8 T·m by toroid magnets. The type of particle is identified according to which detector reacted, as shown in Figure 3.4. Since charged particles are bent by magnetic fields, the momentum of the particle is calculated from the radius of curvature based on detector information. The energy of the particle is measured by the calorimeters. In this section, the coordinate system and subdetectors in the ATLAS experiment are described.

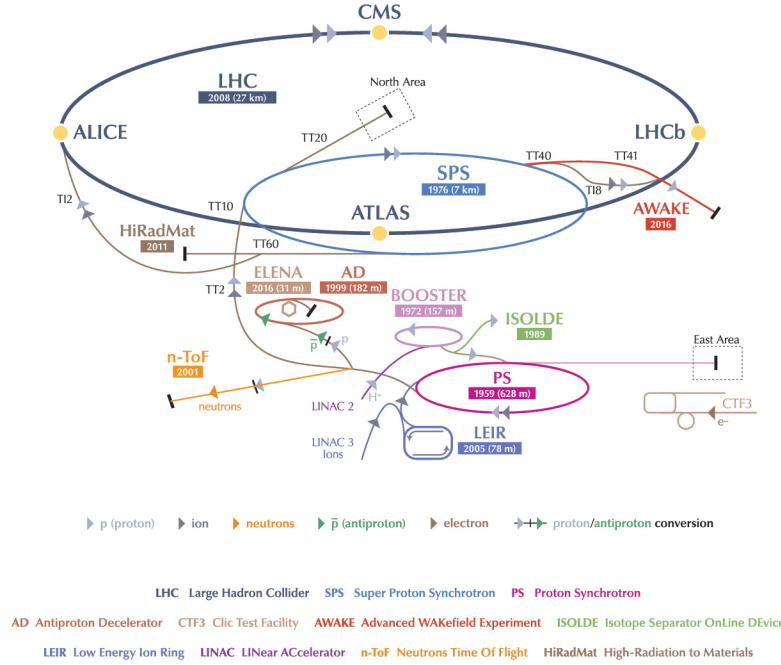


**Figure 3.1:** General view of the accelerator at CERN [34]. The largest, shown in dark blue, is the LHC, and other accelerators are used to step-by-step accelerate the protons entering the LHC.

### 3.2.1 Coordinate system at the ATLAS experiment

The coordinate system used in the ATLAS experiment is shown in Figure 3.5. Since the ATLAS detector is cylindrical, two coordinate systems, a Cartesian coordinate system and a cylindrical coordinate system, are used with the point of collision of the beam as the origin. In the Cartesian coordinate system, the  $z$ -axis is in the direction of the beam axis, the  $y$ -axis is in the direction perpendicular to the ground, and the  $x$ -axis is in the direction of the center of the LHC ring. Cylindrical coordinates use  $R = \sqrt{x^2 + y^2}$  for the cylindrical direction, and  $\phi$  ( $-\pi \leq \phi \leq \pi$ ) for the azimuths, and  $z$ . ATLAS experiments use the pseudorapidity  $\eta$  ( $= -\ln \tan \frac{\theta}{2}$ ) to represent the angle  $\theta$  ( $-\frac{\pi}{2} \leq \theta \leq \frac{\pi}{2}$ ) with the  $z$ -axis in the  $R$ - $z$  plane. In the ATLAS detector, the layout and types of detectors differ greatly between the side and bottom of the cylinder. The side region is called the barrel region, the bottom region is called the endcap region, and the endcap region with large  $|\eta|$  is called the forward region. Also, the region where  $z > 0$  is called A side, and the region where  $z < 0$  is called C side.

In the proton-proton collision, the component of the momentum of the colliding partons in the direction of the beam axis is not uniquely determined. On the other hand, the component of momentum perpendicular to the beam axis is nearly 0 at the time of collision. Therefore, in the ATLAS experiment, the components a transverse momentum  $p_T$  and transverse energy  $E_T$  ( $= E \frac{p_T}{|p|}$ ) perpendicular to the

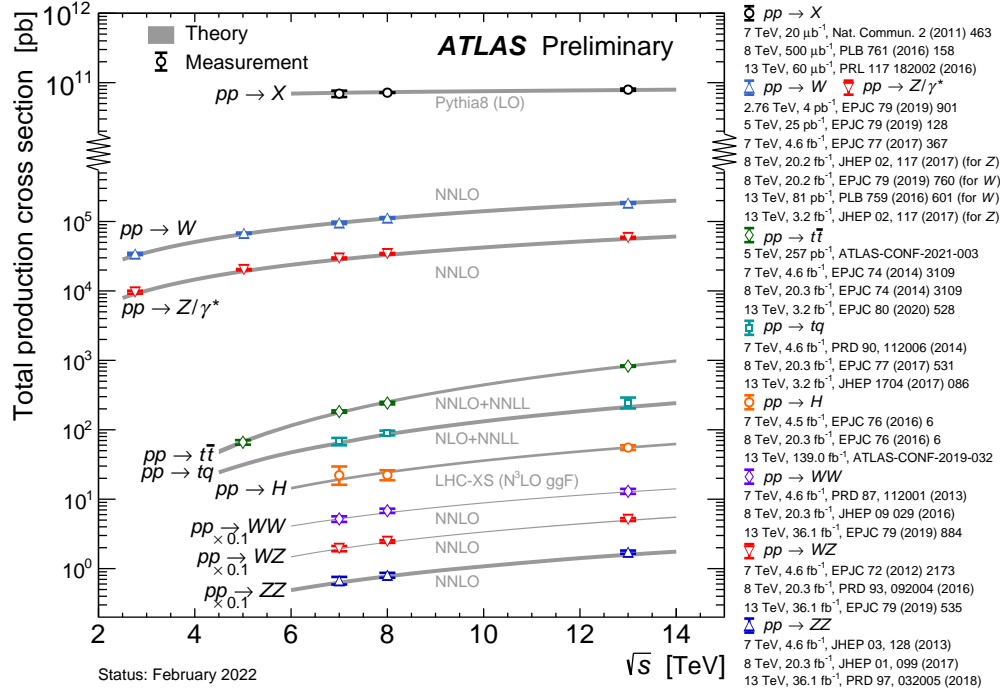


**Figure 3.2:** Total production cross section of SM particles in proton-proton collision [9]. Di-boson event production cross sections are scaled by a factor of 0.1 to avoid overlapping on the figure. The horizontal axis,  $\sqrt{s}$ , is the centre-of-mass energy.

beam axis are used. By using the component perpendicular to the beam axis, the momentum and energy of such as neutrinos, which cannot be detected by the detector, can be calculated as the transverse missing momentum ( $p_T^{\text{miss}}$ ), which is the inverse of the vector sum of  $p_T$  measured by the detector, and the transverse missing energy ( $E_T^{\text{miss}}$ ) by using the law of conservation.

### 3.2.2 Superconducting magnet

In the ATLAS experiment, a magnetic field is applied using a solenoid and toroid magnets as shown in Figure 3.6. By applying a magnetic field, the tracks of charged particles are bent, and the momentum and charge of the particles are measured from the radius of curvature.

A solenoid magnet is positioned between the inner tracking detector and the calorimeter. By applying a magnetic field of 2 T along the beam axis as shown in the left figure of Figure 3.7, the charged particles near the interaction point are bent in the  $\phi$  direction, enabling  $p_T$  measurement by the inner tracking detector.

Toroid magnets are placed inside the muon detector. They are arranged for the barrel and endcap, respectively, and apply a magnetic field of 0.2–3.5 T at the endcap and 0.15–2.5 T at the barrel along the  $\phi$  direction for  $p_T$  measurement at the muon detector. The right figure in Figure 3.7 shows the strength of the magnetic field that a muon with infinite momentum receives when it travels 1 m. Since the toroid magnets are placed in 8-fold symmetry as shown in Figure 3.6, the magnetic field also has

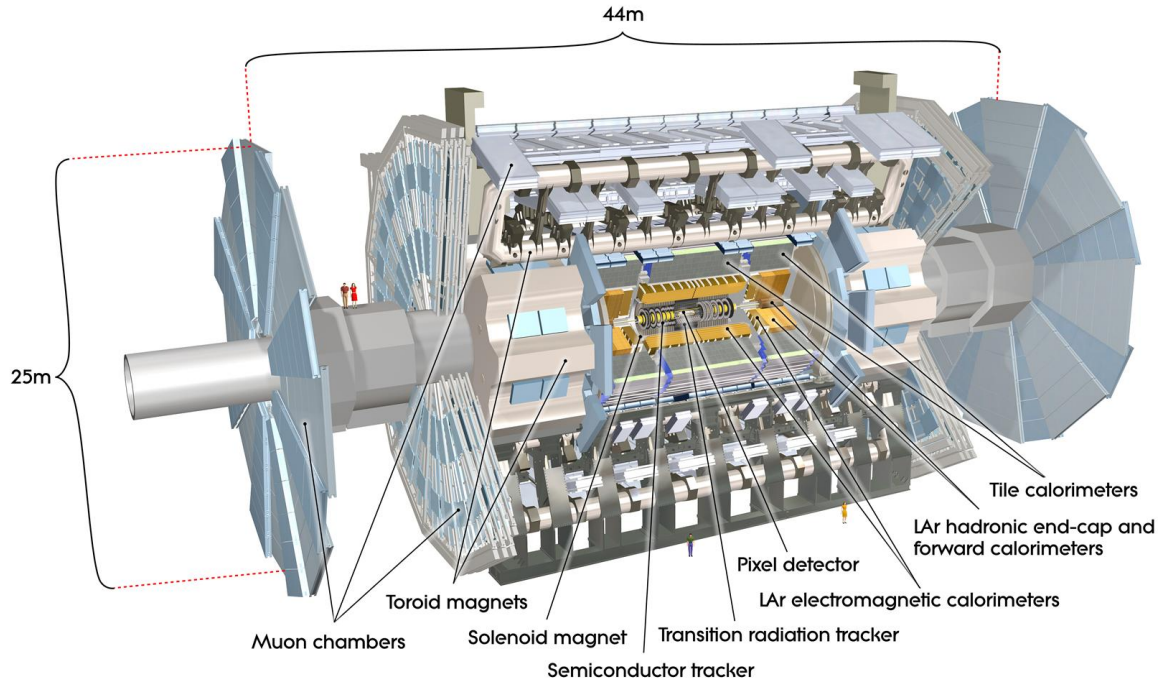


**Figure 3.3:** An overview of ATLAS detectors [35]. It consists of the superconducting magnet, the inner tracking detector, the electromagnetic calorimeter, the hadron calorimeter, and the muon detector.

8-fold symmetry.

### 3.2.3 Inner tracking detector

The inner tracking detector is the innermost detector in the ATLAS detector, and measures the momentum of charged particles around the interaction point and the decay vertex with high accuracy. It consists of Insertable B-Layer (IBL) [39] which is a silicon semiconductor detector, pixel detector, Semiconductor Tracker (SCT) which is a silicon strip detector, and Transition Radiation Tracker (TRT) from the inside as shown in Figure 3.8. Figure 3.9 shows the  $r$ - $z$  cross section view of the layout of a quadrant. The IBL covers the region of  $|\eta| < 3$ , and the other inner tracking detectors cover the region of  $|\eta| < 2.5$ . Passing through a sensor of the inner detector, a charged particle leaves an energy deposit in each sensor. By connecting the several energy deposits, called *hits*, a trajectory of the charged particle can be reconstructed. A reconstructed trajectory is called a track. Tracks have many information about the charged particles: a momentum, a direction and an impact parameter. Table 3.1 shows the number of channels, the size per element (for example, pixel size for pixel detectors), and spatial resolution of each detector.

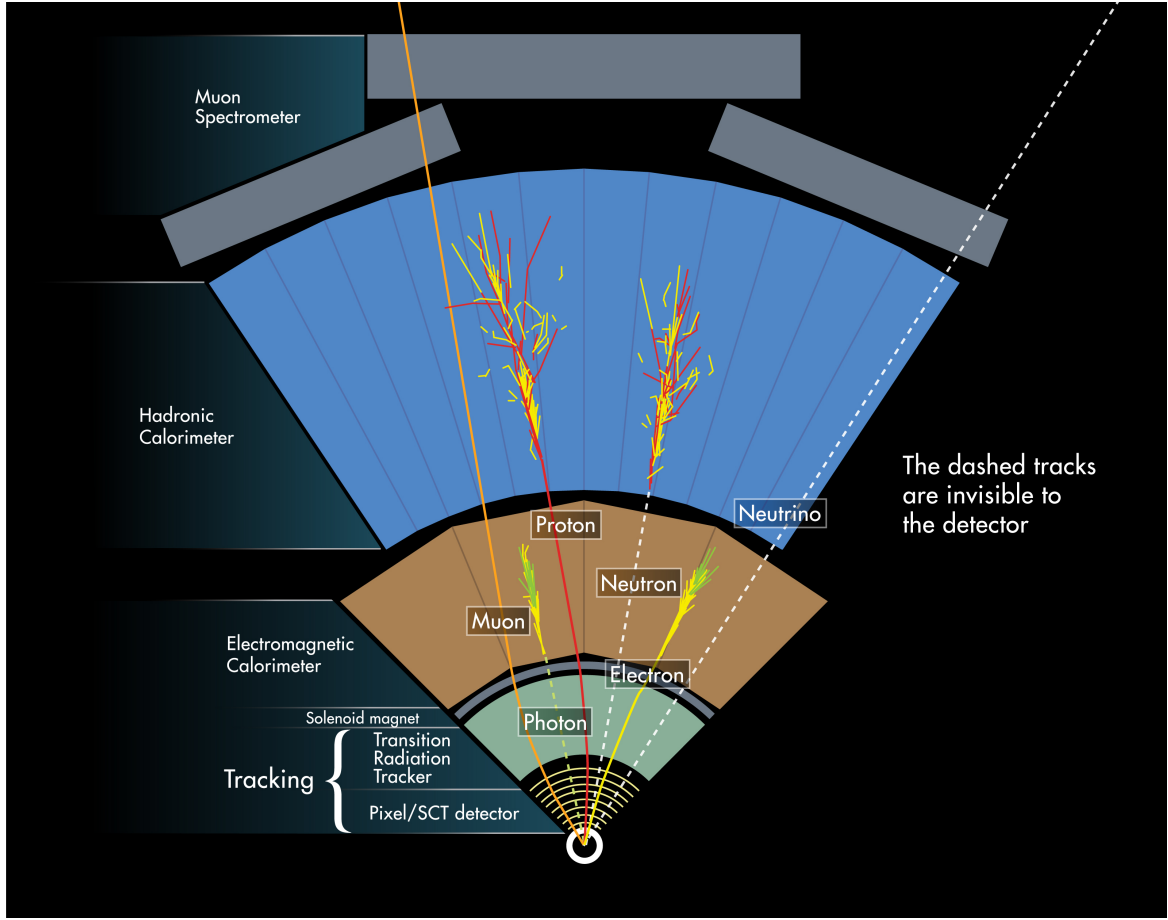


**Figure 3.4:** Diagram showing which detector is used to detect each particle [36].

**Table 3.1:** Parameters for each inner track detector [42, 39]. For IBL and Pixel, the resolution is shown in the  $R - \phi$  plane  $\times z$  direction, and for SCT and TRT, the resolution is shown for the  $R - \phi$  plane.

detector	number of channel	size per element	spatial resolution
IBL	6.0 million	$50 \times 250 \mu\text{m}^2$	$10 \times 60 \mu\text{m}^2$
Pixel	80.4 million	$50 \times 400 \mu\text{m}^2$	$10 \times 115 \mu\text{m}^2$
SCT	6.3 million	$80 \mu\text{m}$	$17 \mu\text{m}$
TRT	351 thousand	$4 \text{ mm}$	$130 \mu\text{m}$

### 3.2.4 Calorimeter

There are two types of calorimeters: electromagnetic calorimeters and hadron calorimeters as shown in Figure 3.10. The inner electromagnetic calorimeter uses electromagnetic showers to measure the energies of mainly electrons and photons, while the outer hadron calorimeters use hadron showers to measure the energies of quark jets and gluon jets.

The electromagnetic calorimeter is a sampling calorimeter with a lead absorption layer and a liquid argon detection layer. It covers the region of  $|\eta| < 1.475$  at the barrel region and  $2.5 < |\eta| < 3.2$  at the

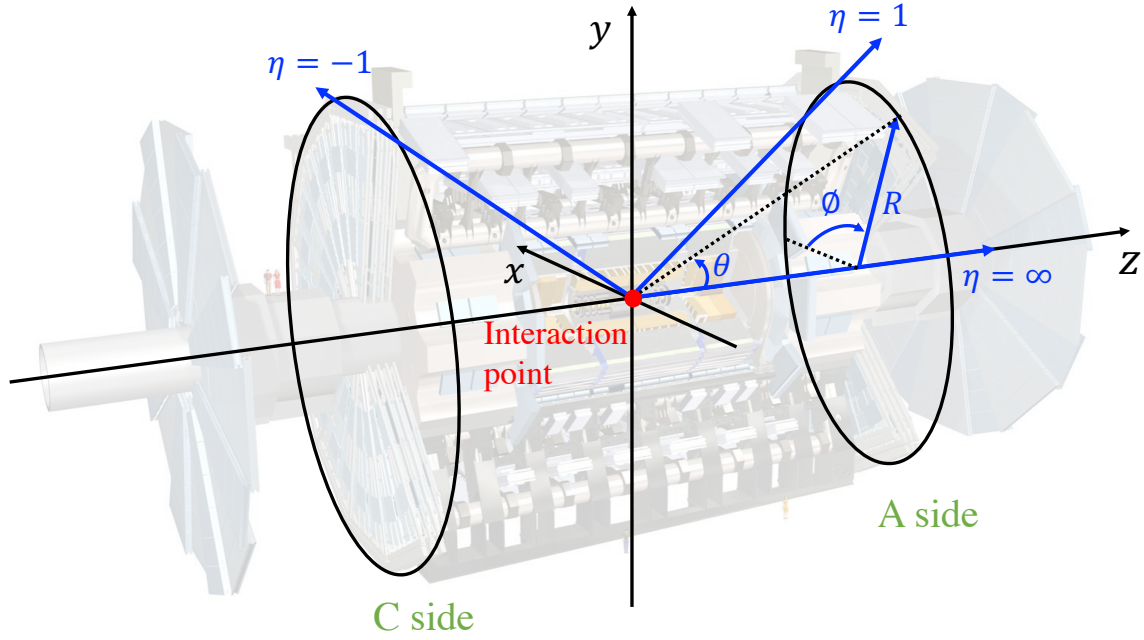


**Figure 3.5:** Coordinate system in the ATLAS experiment. An orthogonal coordinate system and a cylindrical coordinate system are used with the beam axis direction taken as the  $z$ -axis. Also, when representing  $\theta$ , we use the pseudorapidity  $\eta$ .

endcap region.

The hadron calorimeter is also a sampling calorimeter, but the absorption and detection layers are different depending on  $\eta$ . The barrel region ( $|\eta| < 1.7$ ) is covered by a Tile calorimeter with tiled iron and plastic scintillators. The endcap region ( $1.5 < |\eta| < 3.2$ ) is covered by a Hadronic End-cap Calorimeter using copper and liquid argon (HEC). The forward region ( $3.1 < |\eta| < 4.9$ ) employs a forward calorimeter (FCal) using copper or tungsten and liquid argon.

### 3.2.5 Muon detector

The muon detector is the outermost detector of the ATLAS detector (Figure 3.11). Because muons have a much heavier mass than electrons, they are less prone to bremsstrahlung, and they do not interact strongly. Therefore, particles detected by the outermost muon detector can be considered muons. By measuring the radius of curvature of the muon bent by the toroidal magnetic field from the hit information of the muon detectors and the inner detectors, the  $p_T$  of the muon is calculated. It consists of four gas detectors: Monitored Drift Tubes (MDT), Cathode Strip Chambers (CSC), Resistive Plate Chambers (RPC) and Thin Gap Chambers (TGC). The barrel region consists of RPC and MDT, and the endcap region consists of TGC, MDT, and CSC. Among them, TGC and RPC with fast signal response are used for event selection in Level-1 (L1) trigger, and MDT and CSC with good position resolution are used for high-level trigger (HLT) and physics analysis. Table 3.2 shows the position resolution and time resolution of each detector.



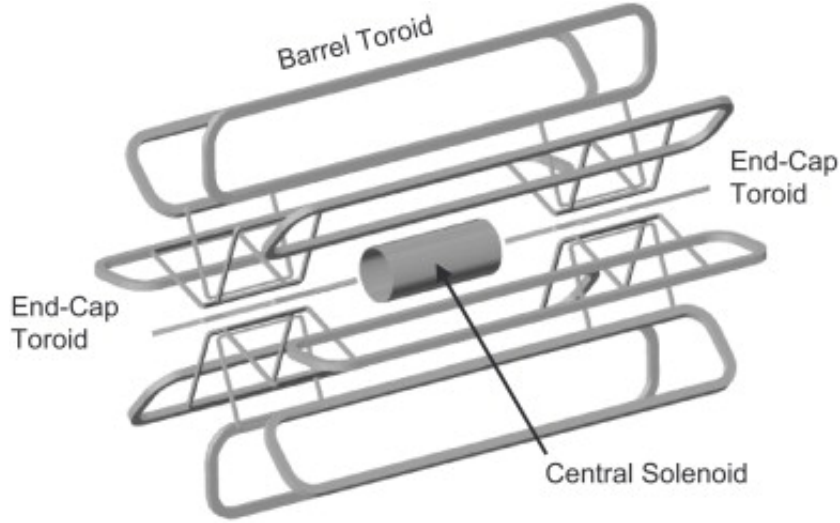


**Figure 3.6:** Arrangement of superconducting magnets in the ATLAS detector [37]. A solenoid magnet is placed between the inner tracking detector and the calorimeter, and toroid magnets are placed inside the muon detector.

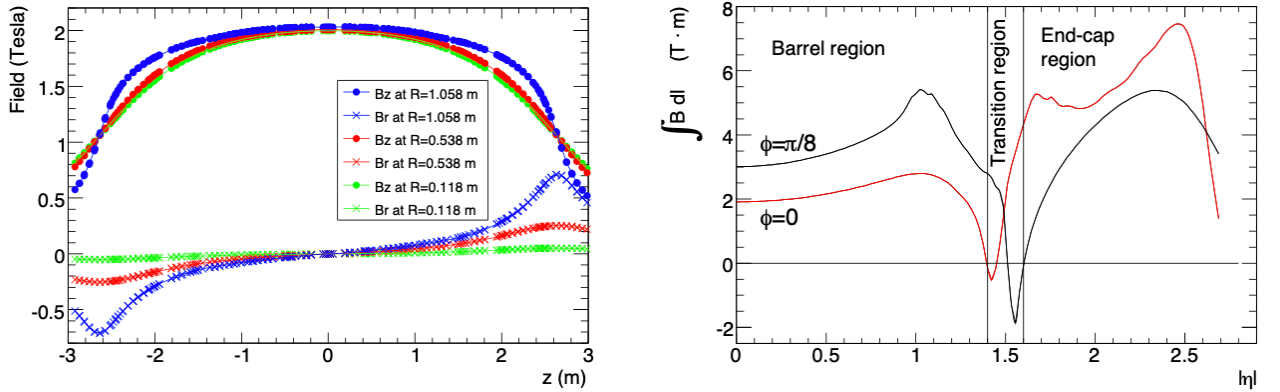


**Figure 3.7:** Magnetic field distribution of a solenoid magnet (left) and a toroid magnet (right) [38]. For the solenoid magnet, the  $z, R$  dependence of the magnetic field at a fixed azimuth angle as shown. In the figure, the distribution represented by circles is the magnitude of the magnetic field along the beam axis ( $z$  direction), and the distribution represented by crosses is the magnitude of the magnetic field perpendicular to the beam axis ( $R$  direction). For the toroid magnet, the  $|\eta|, \phi$  dependence of the magnetic field magnitude is shown. The red curve in the figure represents the magnitude of the magnetic field at  $\phi = 0$ , and the black curve represents the magnitude of the magnetic field at  $\phi = \frac{\pi}{8}$ .

### 3.3 Trigger and data acquisition

In the ATLAS experiment, it is impossible to store the data of all events generated at 40 MHz, as it would require a disk storage of  $O(1)$  ZB. Interesting events such as the events including Higgs boson and new BSM particles are generated with the very small fraction of all generated events as shown in Figure 3.2. Therefore, in the ATLAS experiment, a trigger system is introduced to select only

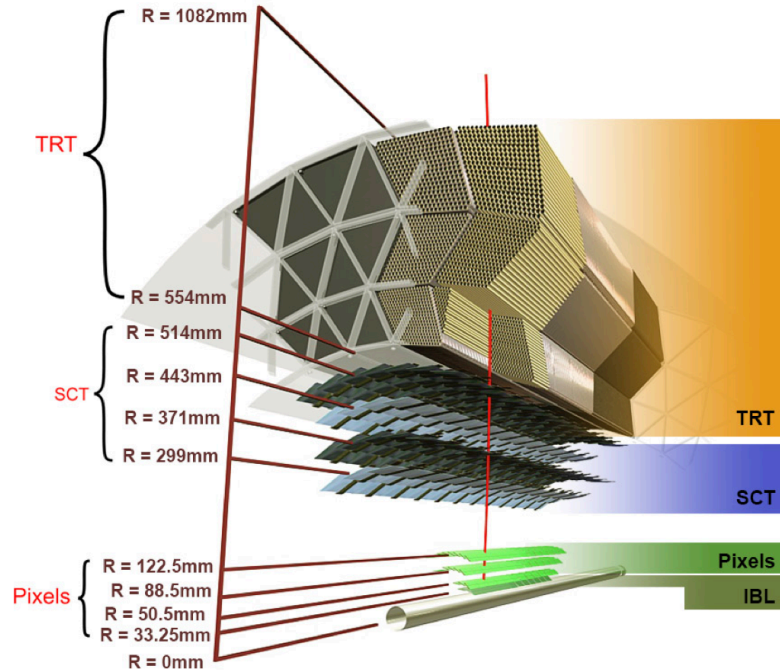


**Figure 3.8:** Cross-sectional view of the inner tracking detector [40]. The cylinder is the beam pipe, and the IBL is installed at 33.25 mm from the beam pipe, the pixel detector at 50.5–122.5 mm, the SCT at 299–514 mm, and the TRT at 554–1082 mm.

**Table 3.2:** Positional and time resolution of each muon detector. The value of the positional resolution does not take into account the error of detector alignment, and the value of the time resolution does not take into account the effects of signal propagation and electronic devices [38].

Detector	Function	Position resolution ( $z/R$ )	Position resolution ( $\phi$ )	Time resolution
MDT	HLT, analysis	$35 \mu\text{m} (z)$	—	—
CSC	HLT, analysis	$40 \mu\text{m} (R)$	5 mm	7 ns
RPC	L1 trigger	10 mm ( $z$ )	10 mm	1.5 ns
TGC	L1 trigger	2–6 mm ( $R$ )	3–7 mm	4 ns

interesting events (e.g. events containing high momentum particles or a large missing energy) from a huge number of events. Trigger selects events based on the number of particles and  $p_T$  derived from detector hit information.

Figure 3.12 shows an overview of the ATLAS trigger system. The events generated at 40 MHz are reduced to maximum 100 kHz in the L1 trigger with the hardware and 1 kHz in the HLT with the software before the storage. By reducing the rate step by step in this way, the HLT in the latter stage can use more time for processing, and can calculate momentum and perform event selection with higher accuracy.

The acquired data is checked to see if it was acquired without any malfunctions in the detector or



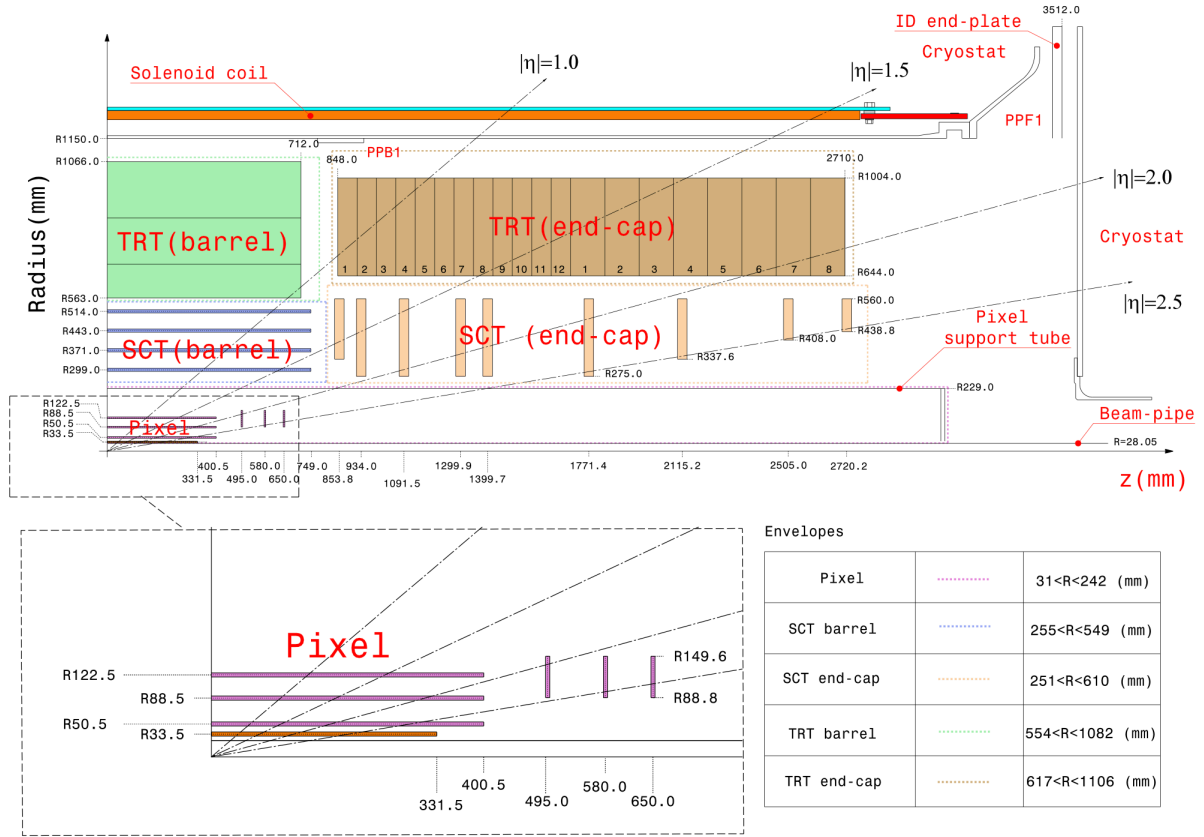


**Figure 3.9:** The  $r$ - $z$  cross-sectional view of the layout of a quadrant of the ATLAS inner detector [41]. The IBL covers the region of  $|\eta| < 3$ , and the other inner tracking detectors cover the region of  $|\eta| < 2.5$ .

trigger system and if there are no abnormalities before the data analysis.

In this analysis, the events stored by multi-jet trigger are used. The detail of the trigger in this analysis will be described in Section 6.2.

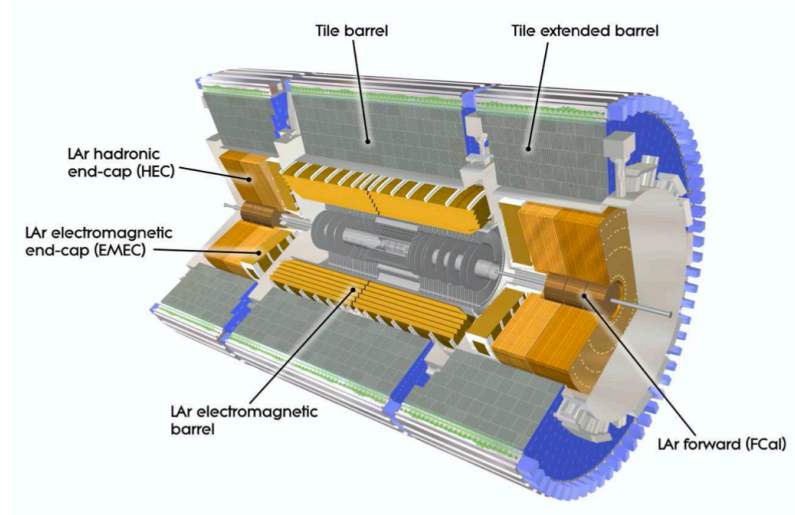


**Figure 3.10:** Cross-sectional view of the calorimeter [38]. Electromagnetic calorimeters, which measure the energies of electrons and photons are placed inside, and hadron calorimeters, which measure the energies of quark and gluon jets, are placed outside.

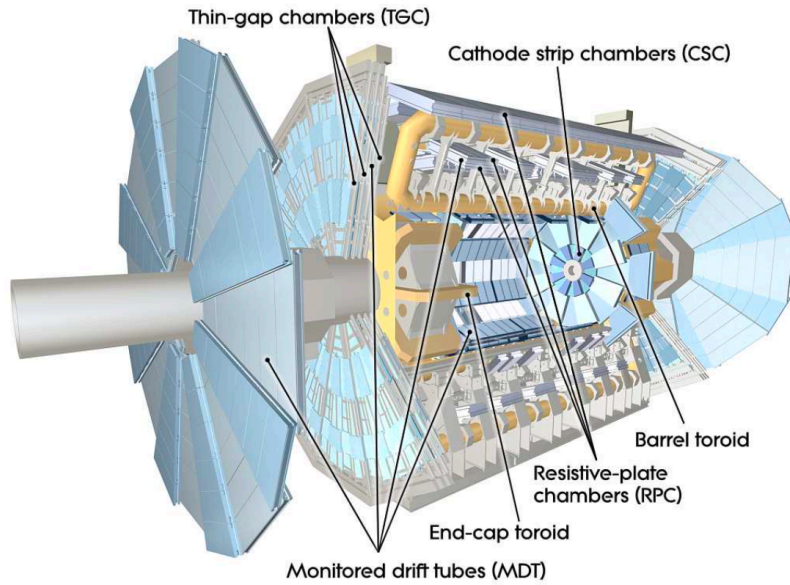


**Figure 3.11:** Cross-sectional view of the muon detector [38]. The barrel part is composed of RPC and MDT, and the endcap part is composed of TGC, MDT and CSC.

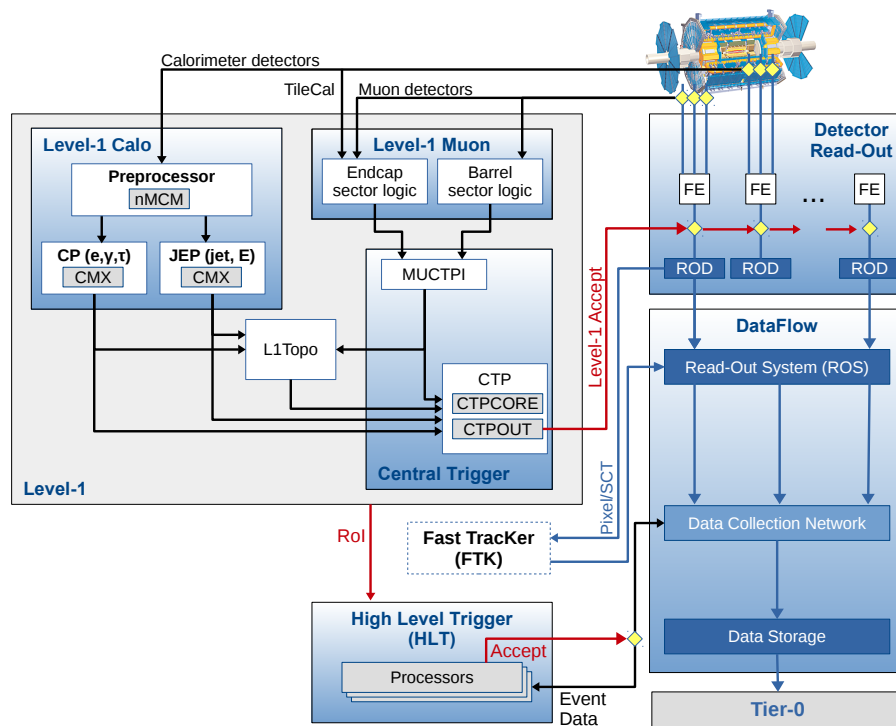


**Figure 3.12:** Overview of ATLAS trigger system and data acquisition system in Run 2 [43]. Only events accepted by L1 trigger and HLT are stored in data storage.

## Chapter 4

# Data and simulation samples

### 4.1 Data sample

This analysis uses  $139 \text{ fb}^{-1}$  of  $pp$  collision data collected at  $\sqrt{s} = 13 \text{ TeV}$  by the ATLAS detector during the data taking periods from 2015 to 2018. Data quality was monitored at all times, and the data where the detector did not work at its desired performance was filtered out from the data for physics analyses. The accumulation of the good data for physics analyses compared to the data delivered by the LHC and recorded by ATLAS is shown in Figure 4.1. The overall uncertainty on the luminosity of the dataset used in this search is 1.7%, obtained primarily using the luminosity measurement detector (LUCID-2 [44]).

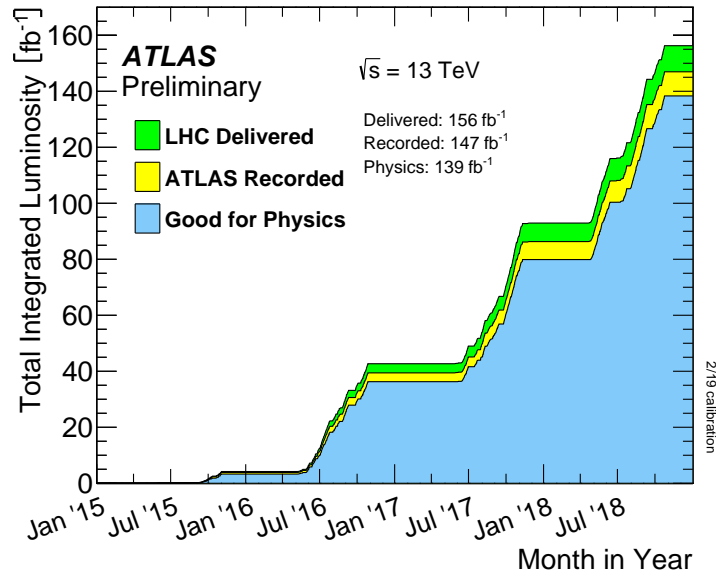


**Figure 4.1:** Integrated luminosity available in physics analyses ("Good for Physics") compared to the integrated luminosity provided by the LHC ("LHC Delivered") and recorded by the ATLAS detector ("ATLAS Recorded") [45].

When instantaneous luminosity increases, the number of  $pp$  interactions per bunch crossing also increases. The rate of the target process is generally rare, and most of the  $pp$  interactions are multi-parton soft QCD interactions. They are not interesting. Figure 4.2 shows a distribution of the number

of  $pp$  interactions per bunch crossing called pile-up in the data in 2015–2018. The average pile-up is 33.7.

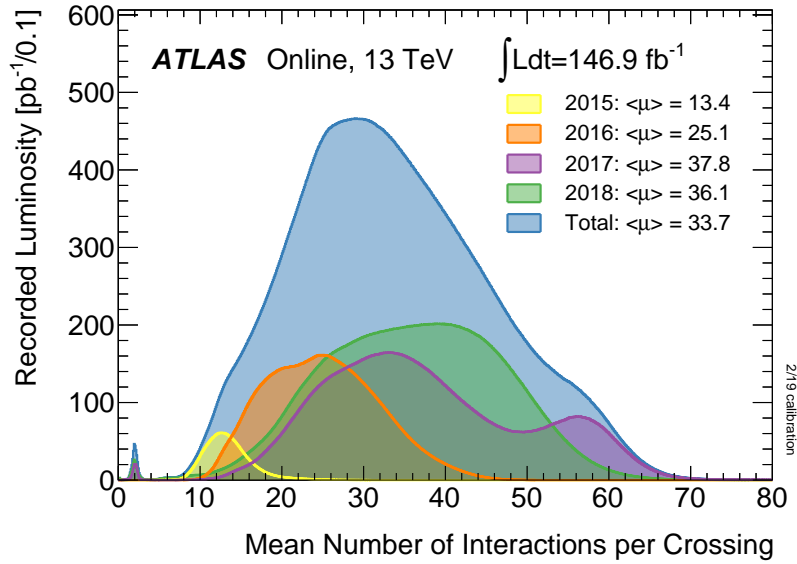


**Figure 4.2:** Number of interactions per crossing in each year [45]. Each year and the total for 2015–2018 are represented by difference colors.

## 4.2 Simulation samples

Monte Carlo (MC) simulated event samples are used to estimate the number of the signal and background events. The simulation is processed in three steps: the event generation, the pile-up simulation, and the detector simulation. Firstly, the events are generated based on theoretical calculations. Secondary, to simulate the effects of pile-up, additional interactions were generated using the soft QCD processes provided by PYTHIA 8.186 with the A3 tune [46] and the MSTW2008LO PDF set [47], and overlaid onto each simulated hard-scatter event. The MC samples were reweighted so that the pile-up distribution matches the one observed in the data. The information up to this point is called *truth-level* information. Finally, the MC samples were processed through an ATLAS detector simulation [48] based on GEANT4 [49]. All MC samples were reconstructed in the same manner as the data described in Chapter 5.

Event generation for each sample of signal and background is summarized below.

### Signal samples

Following two signal models are taken into account in this analysis:

- neutralinos are produced via gluinos and decay into three quarks via the RPV coupling  $\lambda''$  with lifetime of  $O(0.01) - O(10)$  ns as shown in Figure 2.11(a), referred to as the *gluino pair production model*.

- electroweakinos of pure higgsinos are produced directly and decay into three quarks via the RPV coupling  $\lambda''$  with lifetime of  $O(0.01) - O(10)$  ns as shown in Figure 2.11(b), referred to as the *electrowikino pair production model*.

The matrix element (ME) calculation for the SUSY production processes was performed to leading-order precision with MADGRAPH5\_AMC@NLO 2.6.2 [50] interfaced to PYTHIA 8.212 [51] for the parton showering (PS) and hadronization. All other SUSY-particle contributions are assumed to be decoupled. The matrix element calculation was performed at tree level and includes the emission of up to two additional partons for all signal samples. The PDF set used for the generation of the signal samples was NNPDF2.3LO [52] with the A14 [53] set of tuned underlying-event and shower parameters. The ME-PS matching was performed with the CKKW-L prescription [54, 55], with a matching scale set to one quarter of the produced SUSY particle mass. Signal cross-sections for the gluino pair production were calculated to approximate next-to-next-to-leading-order (NNLO) in the strong coupling constant, adding the resummation of soft gluon emission at next-to-next-to-leading-log (NNLL) accuracy (approximate NNLO+NNLL) [56, 57, 58, 59, 60, 61, 62, 63]. The nominal cross-section and its uncertainty were derived using the PDF4LHC15\_mc PDF set, following the recommendations of Ref. [64]. The electroweakino production cross sections are computed at NLO plus next-to-leading-log (NLL) precision [65, 66, 67, 68, 69] in a limit of mass-degenerate higgsinos  $\tilde{\chi}_2^0$ ,  $\tilde{\chi}_1^\pm$ , and  $\tilde{\chi}_1^0$ . The nominal cross-section and the uncertainty are taken from an envelope of cross-section predictions using different PDF sets and factorization and renormalization scales, as described in Ref. [2]. In the gluino case, the cross-sections range from  $8.9 \pm 1.4$  fb to  $46 \pm 14$  ab depending on the gluino mass from 1.6 TeV to 2.6 TeV, respectively. In the electroweakino case, they range from  $693 \pm 17$  fb to  $21.5 \pm 3.7$  ab depending on the neutralino mass from 100 GeV to 1700 GeV, respectively.

## Background samples

The background events are estimated using the dijet MC samples, as no specific SM process is assumed. Dijet events were generated using PYTHIA 8.230 with leading-order matrix elements for dijet production which were matched to the parton shower. The NNPDF2.3LO PDF set was used in the ME generation, the parton shower, and the simulation of the multi-parton interactions. The A14 set of tuned parameters was used. These samples are used for an independent closure test of the data-driven background estimates and calculation of tracking and vertexing systematic uncertainties.

## Chapter 5

# Reconstruction and object definition

This section describes the way of the reconstruction of physics objects used in this analysis, which are tracks and vertices including the dedicated techniques for the DV reconstruction, leptons, and jets.

### 5.1 Standard track reconstruction

Track reconstruction in the inner detector primarily uses an inside-out tracking, followed by an outside-in tracking.

#### 5.1.1 Inside-out tracking

The track reconstruction algorithm first looks for a track seed in the pixel and SCT detectors. Track seeds are built from three pixel space points, three SCT space points, or a combination of space points from both detectors. A space point is defined as hits in the pixel detector or the coincidence of axial and stereo layers in the SCT detector.

Second, the parameters of the track seed are obtained and track candidates are found. The track projected into the transverse plane follows a circular trajectory, which is uniquely described by the  $p_T$  and the transverse impact parameter  $d_0$ . Figure 5.1 shows a sketch of the technique used to estimate the parameters of the track seeds. The  $p_T$  is obtained from the radius  $\rho$  of the circle by assuming that the magnetic field  $B$  is parallel and homogeneous to the  $z$ -axis, using the following equation:

$$\rho[\text{mm}] = \frac{p_T[\text{GeV}]}{3 \cdot 10^{-4} \times q[\text{e}] \times B[\text{T}]} \quad (5.1)$$

The nominal value of the magnetic field in the ATLAS solenoid magnet is 2 T and the charge of the particle  $q[\text{e}]$  is determined from the direction of bending of the trajectory. The  $d_0$  of the track seed, which is the distance of the closest approach of the track to a reference point, is calculated at the point where the circle intersects the line connecting the reference point and the centre of the circle:

$$d_0 = \sqrt{c_X^2 + c_Y^2} - \rho, \quad (5.2)$$

where  $c_X$  and  $c_Y$  are the coordinates of the circle centre with respect to the reference point. The reference point is the origin in x-y-z space or the beam spot position. If the track seed passes certain

quality criteria, such as  $p_T$  and  $d_0$  selections [70], a window search is constructed from the track seed and track candidates are formed using the combinatorial Kalman filter [71].

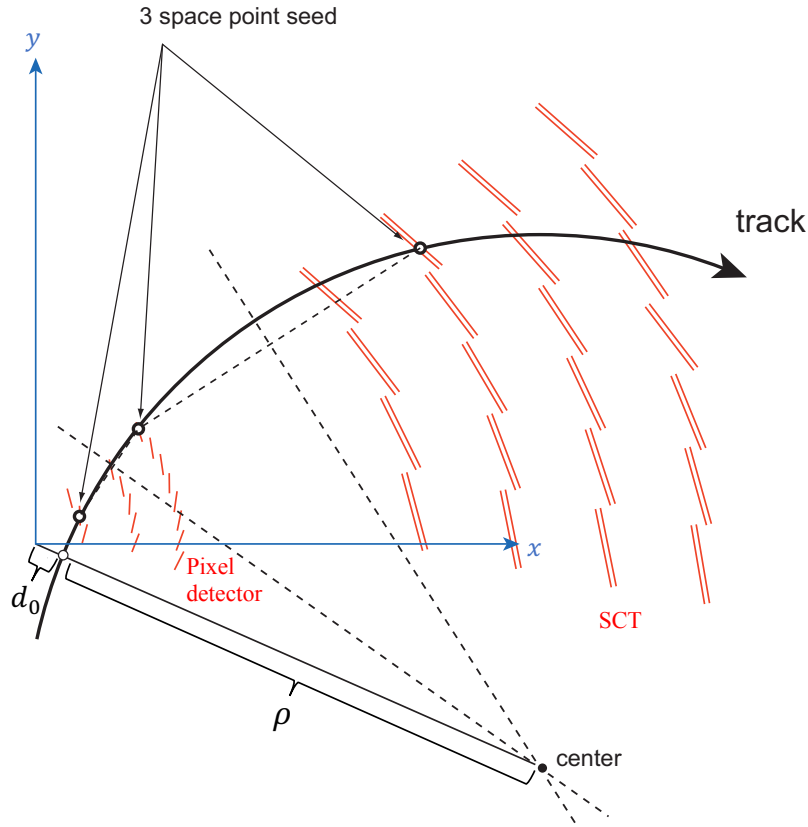


**Figure 5.1:** A sketch of the technique used to estimate the track parameters of the seeds [70].

The collection of the track candidates includes the fake tracks which have random hits combinations or duplicated tracks which have a shared space point with another track candidate. In the third step, the ambiguity of fake or duplicated tracks is resolved based on a *track score* that is calculated from fit quality in the Kalman filter and the number of shared hits and holes [71, 72]. The hole means a missing cluster, which is expected there, in the road of the track candidate.

Finally, track candidates passing the ambiguity solving step are extended into the TRT. By extrapolating the track to TRT detectors, the near TRT hits are added as TRT-hits candidates. Here in order to reduce the bad extrapolation with wrongly assigned TRT hits, a track without the extrapolation is kept if the *track score* becomes higher after the extrapolation.

### 5.1.2 Outside-in tracking

Inside-out tracking can reconstruct most of the charged particles from the interaction points. However, it assumes that charged particles leave the sufficient number of silicon (pixel or SCT detector) hits from inner most layer. Therefore, it doesn't work in the cases of the secondary particles from meta-stable particles and photon conversion that silicon-detector hits are intrinsically missing.



In order to reconstruct such tracks, TRT track candidates are used for seeding instead of hits in silicon detectors. Standalone TRT track candidates are reconstructed in the  $\eta$ - $\phi$  regions ( $0.4 \times 0.4$  in  $\Delta\eta \times \Delta\phi$ ) determined by deposits in the electromagnetic calorimeter. The resulting TRT track candidates may then be extended back into the silicon detectors by associating any hits which are not used by existing tracks reconstructed by the inside-out tracking. This tracking can reconstruct tracks which originate far from the interaction points but still have small impact parameters.

## 5.2 Primary vertex reconstruction

Primary vertex is reconstructed from tracks. Also, impact parameter requirements are applied to reduce contamination from tracks originating from secondary interactions. Reconstruction of vertices is only carried out using tracks that satisfy the following requirements [73]:

- $p_T > 400$  MeV
- $|d_0| < 4$  mm,  $\sigma(d_0) < 5$  mm,  $\sigma(z_0) < 10$  mm
- For  $|\eta| < 1.65$ : SCT detector hits  $\geq 4$ , silicon (SCT or pixel) hits  $\geq 9$ , Pixel holes = 0
- For  $|\eta| \geq 1.65$ : silicon hits  $\geq 11$ , SCT holes  $\leq 1$
- IBL hits + B-layer (most inner pixel layer) hits  $\geq 1$
- A maximum of 1 shared module (1 shared pixel hit or 2 shared SCT hits)

The parameters  $d_0$  and  $z_0$  denote the transverse and longitudinal impact parameters of tracks with respect to the centre of the luminous region, and  $\sigma(d_0)$  and  $\sigma(z_0)$  denote the corresponding uncertainties. The fit is repeated using these tracks until no additional vertex is found.

## 5.3 Displaced vertex reconstruction

This search targets the model including the massive particles with mean proper lifetimes  $\tau$  up to  $O(10)$  ns. Several charged decay products derived from long-lived particles (LLPs) flying  $O(1) - O(100)$  mm originate from locations in the detector with a substantial displacement from the primary  $pp$  interaction. Such a LLP decay point is called displaced vertex (DV), and dedicated techniques are required for an efficient reconstruction of the decay objects. In this section, tracking and vertexing techniques for reconstructing DVs are described.

### 5.3.1 Large Radius Tracking

The standard track reconstruction algorithm is optimized for charged particles originating from the interaction region, or from decays of short-lived particles  $c\tau < 10$  mm such as  $b$ -hadrons. Constraints are set on the transverse and longitudinal impact parameters of track candidates relative to the primary vertex ( $|d_0| < 10$  mm and  $|z_0| < 250$  mm, respectively), and their hit multiplicities in order to reduce the computational complexity. These selections result in inefficiencies in the reconstruction of tracks with large impact parameters, corresponding to charged particles produced in the LLP decays. To

reconstruct these tracks, a dedicated track reconstruction, called *large-radius tracking* (LRT) [74, 75], is performed. This reconstruction uses the hits left over from the standard tracking procedure and applies looser requirements, in particular on the transverse and longitudinal impact parameters ( $|d_0| < 300$  mm and  $|z_0| < 1500$  mm). The illustration and requirements of standard tracking and LRT are summarized in Figure 5.2 and Table 5.1.

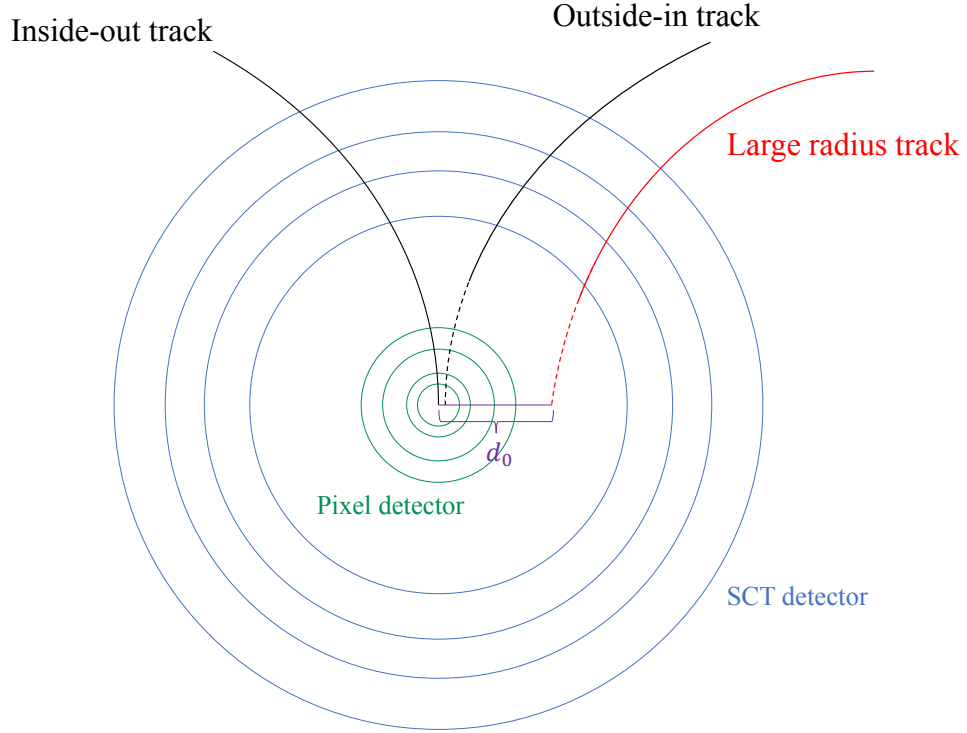


**Figure 5.2:** Illustration of standard track and large radius track on the  $x$ - $y$  plane. The solid curve shows the actual track and the dashed curve shows the extrapolated part for the calculation of  $d_0$ .

**Table 5.1:** Most important selections that differ between the standard and the large radius tracking setups [74].

	Standard	Large radius
Minimum $p_T$ [MeV]	500	900
Maximum $d_0$ [mm]	10	300
Maximum $z_0$ [mm]	250	1500
Maximum $ \eta $	2.7	5
Maximum shared silicon module	1	2
Minimum unshared silicon-detector hits	6	5
Minimum silicon-detector hits	7	7

### 5.3.2 Secondary vertex reconstruction

A dedicated secondary vertex reconstruction algorithm for LLP decays is employed to reconstruct DVs [76]. Tracks reconstructed by the standard tracking and LRT are used throughout the vertex reconstruction. All tracks are required to have transverse momentum  $p_T > 1$  GeV. Tracks are explicitly required not to be associated to any primary vertices.

The secondary vertices are reconstructed with the following order:

1. Form two-track seed vertices with high-quality tracks.
2. Merge the seed vertices to form N-track vertices.
3. Attach lower-quality tracks to the vertices.

#### Form two-track seed vertices

First, seed vertices are formed from two tracks called two-track seed vertices. Tracks used in this step satisfy the following criteria:

- If the track has no pixel hits, it must have at least six hits in the SCT.
- If the track has fewer than two pixel hits, it must have at least one hit in the TRT.
- If the track  $p_T$  is less than 20 GeV, it must have at least seven hits in the SCT. In addition, if the track  $|\eta|$  is less than 1.7, it must have at least 20 hits in the TRT.

Both tracks constructing the seed vertex are required to fulfil the hit-pattern shown in Figure 5.3. This requirement is from the concept that the tracks should have hits in tracker layers with radius beyond the seed vertex position, and should not have hits in tracker layers with radius smaller than the seed vertex position (Figure 5.3(a)). This requirement is not applied for tracker layers in close proximity to the seed vertex position, to accommodate the mismeasurement of the vertex position (Figure 5.3(b)). At least one track in each two-track seed vertex must have  $|d_0| > 2$  mm. Tracks used to seed vertex formation are called *selected tracks*.

#### Merge the seed vertices to form N-track vertices

In the two-track vertex forming stage, track can be used multiple times in different seed vertices. As the first step of N-track vertex forming stage, this usage of multiple times is resolved by comparing their  $\chi^2$  values in the vertex fits, or by merging the vertices if the distance between their estimated positions is not significant enough.

As the next step of the N-track forming stage, nearby vertices are merged into a single vertex. This is in order to mitigate splitting of the actual one LLP decay. Candidates for merged vertex are chosen in ascending order of the number of selected tracks constructing the vertex. The number of selected tracks is called track multiplicity. The algorithm attempts to merge each candidate with all other vertices with higher selected track multiplicity, in descending order of selected track multiplicity. If the positions of two vertices are within  $10\sigma$ , whether they are merged or not is considered. The parameter  $\sigma$  is the uncertainty on the difference between the two vertex positions, calculated as

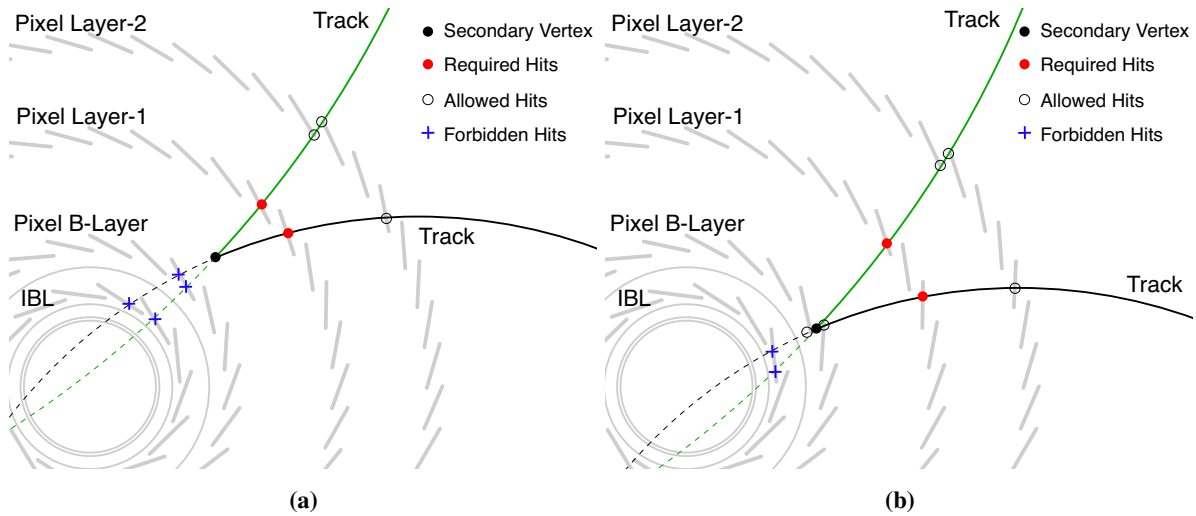


**Figure 5.3:** Example hit pattern of the tracks using secondary vertexing [76]. (a) The vertex is between the two layers of B-Layer and Layer-1 sensors. The tracks of the reconstructed secondary vertex must not have hits on the layers within the vertex radius (i.e. IBL and B-Layer), and must have hits on the closest layer outside the vertex (i.e. Layer-1). (b) The vertex is close to the pixel B-Layer sensors. In this example where the vertex is inside the B-Layer, the tracks are not allowed to have hits on the IBL but may have hits on the B-Layer, and must have hits on the Layer-1.

the quadratic sum from the covariance matrices of the two individual vertex fits. In the following, the lower selected track multiplicity vertex will be denoted “LMV,” while the higher selected track multiplicity vertex will be denoted “HMV.” Three tests are used to determine if two vertices should be merged into a single vertex:

- Vertices with a larger number of tracks have an improved position resolution compared to those with a smaller number of tracks. In order to address the situation that the LMV originates from the HMV but is distinguished from the HMV due to its poor position resolution, the LMV is refitted using the HMV position as the initial value. The vertices are merged and refitted as a single vertex if the updated vertex position is compatible with the HMV position.
- The selected tracks associated with the HMV are associated one by one with the LMV and the vertices are refitted again with the HMV position as the initial value. It is repeated for all tracks constructing the HMV and if any of the refitted vertices match the HMV position, they are merged and refitted as a single vertex.
- All of the selected tracks from both vertices are used in a single vertex fit using the position of the HMV as the initial value. If the refitted vertex is compatible with the HMV position, the vertices are merged to form a single vertex.

Finally, any remaining vertices within 1 mm are forced to merge, and all merged vertices are refitted with all tracks from the two input vertices.

### Attach lower-quality tracks

As the final stage, additional tracks satisfying looser selection criteria are attached to the reconstructed vertices in order to recover inefficiencies from the vertex seeding selection. These tracks are referred to as *attached tracks* and have looser hit selection requirements than selected tracks. Attached track requirements are summarized in Table 5.2. Hit pattern matching is follow:

- If a vertex is after the innermost pixel layer, a hit is required in the next outer layer of the vertex position, but no requirement is placed on hits in the inner layers.
- If a vertex is before the innermost pixel layer, hits are required in the first two layers of the pixel detector.

**Table 5.2:** Attached Track Requirements

$p_T > 1 \text{ GeV}$
Modified hit pattern matching
$ d_0 $ -significance $< 5$ with respect to the secondary vertex
$ z_0 $ -significance $< 5$ with respect to the secondary vertex

A track is associated to a single secondary vertex only, and tracks are preferentially associated with vertices with higher track multiplicity. Tracks already associated to any secondary vertex are not considered for further association to other vertices. Attachment is not accepted if  $\chi^2_{\text{vertex}}/n_{\text{dof}}$  becomes greater than 20.

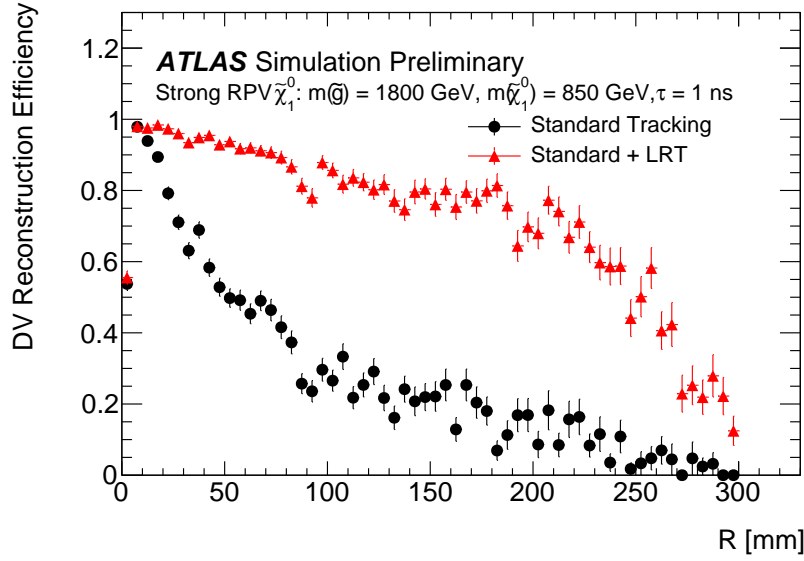
At this point, the final vertex fit is performed using all of the selected and attached tracks and the parameters with respect to the vertex position are re-calculated.

Figure 5.4 shows the improvement of the vertex reconstruction efficiency by using the LRT with respect to using only standard tracking at large radial position  $R$ . The efficiency decreases rapidly beyond 300 mm because the LRT algorithm requires at least seven silicon-detector hits. The drop of the vertex efficiency at small values of the radius  $R$  is due to the requirement of having at least one track with  $|d_0| > 2 \text{ mm}$  for forming the vertices.

## 5.4 Lepton reconstruction

While electrons and muons are not used in the event selection in this search, they are used in a procedure to remove overlapping objects described in Section 5.6.

Electron candidates are reconstructed from isolated electromagnetic calorimeter energy deposits matched to inner detector (ID) tracks, which are reconstructed in the inner detectors, and are required to have  $|\eta| < 2.47$ , a transverse momentum  $p_T > 10 \text{ GeV}$ , and to satisfy the *LooseAndBLayer* requirement defined in Ref.[77]. The *LooseAndBLayer* requires the electron-like quality based on a likelihood using measurements of shower shapes in the calorimeter and track properties in the inner detector as



**Figure 5.4:** LLP vertex reconstruction efficiency with and without the special LRT processing are shown for one benchmark signal as a function of the transverse distance ( $R$ ) from the nominal interaction point.

input variables, and also requires a hit in the innermost pixel layer.

Muon candidates are reconstructed in the region of  $|\eta| < 2.7$  by matching the muon spectrometer (MS) tracks reconstructed by only muon detectors with the ID track. Muons are required to have  $p_T > 10$  GeV and satisfy the *medium* identification requirements defined in Ref. [78], based on the number of hits in the different ID and MS subsystems, and on the ratio of the charge and momentum measured in the ID and MS divided by the sum in quadrature of their corresponding uncertainties.

## 5.5 Jet reconstruction

Two methods of the jet reconstruction are used in this analysis.

### 5.5.1 Calo jet

Calo jets are reconstructed from three-dimensional energy clusters in the calorimeters using the anti- $k_t$  jet clustering algorithm [79] with a radius parameter of  $R = 0.4$  [80]. When just "jet" is used, it refers to the calo jet. The energy resolution in the jet reconstruction in data and MC and the uncertainties from the difference in resolution between data and MC are shown in Figure 5.5.

Only jet candidates with  $p_T > 20$  GeV and  $|\eta| < 2.8$  are considered. Events are discarded if they contain a jet with  $p_T > 20$  GeV satisfying at least one of the following selection criteria, which are designed to reject detector noise and non-collision backgrounds [82]:

- $f_{\max} > 0.99$  and jet  $|\eta| < 2$
- $E_{\text{neg}} > 60$  GeV and  $f_{\max} > 0.85$
- $f_{\text{HEC}} > 0.5$ ,  $\langle Q \rangle > 0.5$ , and  $f_Q^{\text{LAr}}/65535 > 0.8$

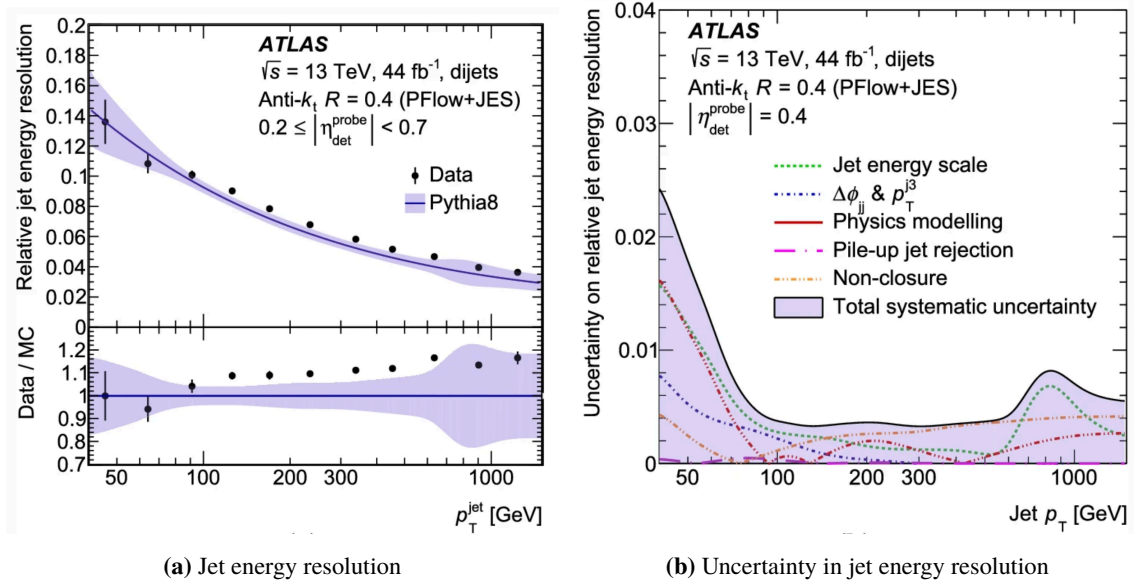


**Figure 5.5:** (a) The resolutions of the jet energy calculation in data and MC, and (b) the uncertainties from the difference in resolution between data and MC are shown [81].

- $f_{\text{EM}} > 0.95$ ,  $f_Q^{\text{LAr}} > 0.8$ , jet  $|\eta| < 2.8$ , and  $f_Q^{\text{LAr}}/65535 > 0.8$

where the variables used to identify bad jets are:

- $\langle Q \rangle$ : The average jet quality is defined as the energy-squared weighted average of the pulse quality of the calorimeter cells in the jet. The pulse quality is the quadratic difference between the actual and expected cell pulse shapes is used to discriminate noise from real energy deposits.
- $f_Q^{\text{LAr}}$ : Fraction of the energy in the liquid argon calorimeter cells of the jet with poor signal shape quality
- $E_{\text{neg}}$ : Sum of energy of all cells with negative energy in the jet
- $f_{\text{EM}}$ : Ratio of the energy in the electromagnetic calorimeter to the total energy of the jet
- $f_{\text{HEC}}$ : Ratio of the energy in the hadronic end-cap calorimeter to the total energy of the jet
- $f_{\text{max}}$ : Maximum energy fraction in any single calorimeter layer

This is called "jet cleaning".

After the jet cleaning, jets are calibrated with the following steps [83]:

- Jet energy scale (JES) calibration
- *In situ* calibration

### Jet energy scale calibration

The JES calibration transfers the jet momentum from reconstructed to the particle level. In this calibration, firstly, the Gaussian fit is performed to the  $R$ :

$$R = \frac{E_T^{\text{reco}}}{E_T^{\text{truth}}}, \quad (5.3)$$

where  $E_T^{\text{reco}}$  and  $E_T^{\text{truth}}$  are the reconstructed and particle level transverse energy of jets. This fit is performed in each  $E_T^{\text{truth}}$  and  $\eta_{\text{det}}$  range which is defined as  $\eta$  pointing to the geometric center of the detector in order to avoid the ambiguity on the detector regions used for the jet reconstruction. The  $\langle R \rangle$  defined as the mean of the Gaussian fit is used to calibrate the absolute jet energy scale. The  $\langle R \rangle$  in each  $\eta_{\text{det}}$  is shown in Figure 5.6.

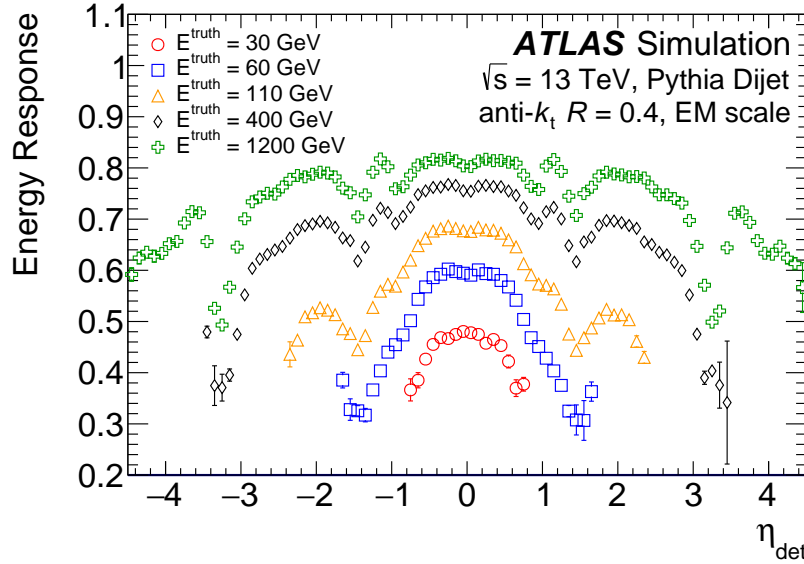


**Figure 5.6:** The energy response  $\langle R \rangle$  as a function of  $\eta_{\text{det}}$  for jets with various particle level energy ( $E^{\text{truth}}$ ) [83].

### In situ calibration

The *In situ* calibration aims to compensate the difference between the data and MC simulation. This calibration is performed for only the data. The  $R_{\text{in situ}}$  is defined as the average of  $p_T$  ratio of the jets and reference objects, and obtained using  $Z(\rightarrow ll)+\text{jet}$ ,  $\gamma+\text{jet}$ , and multi-jet events.  $Z$ ,  $\gamma$  and the vector sum of recoiling jets, which are the jets other than the leading jet, are the reference objects for the  $Z(\rightarrow ll)+\text{jet}$ ,  $\gamma+\text{jet}$ , and multi-jet events, respectively. The  $R_{\text{in situ}}$  is calculated both in the data and MC simulation and the correction factor is obtained as:

$$c = \frac{R_{\text{in situ}}^{\text{data}}}{R_{\text{in situ}}^{\text{MC}}}. \quad (5.4)$$

The correction factor calculated from all processes is shown in Figure 5.7.

Uncertainties on the JES after *In situ* calibration are shown in Figure 5.8.



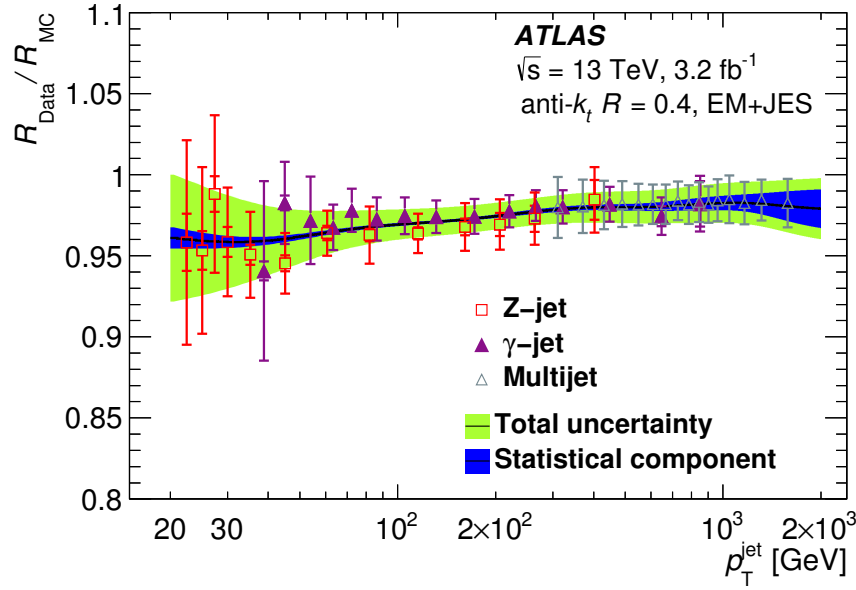


**Figure 5.7:** The correction factor in the *In situ* calibration using  $Z$ +jet,  $\gamma$ +jet, and multi-jet events as a function of the jet  $p_T$  [83]. The final derived correction is the black line. The statistical and total uncertainty bands are shown as the blue and green bands, respectively.

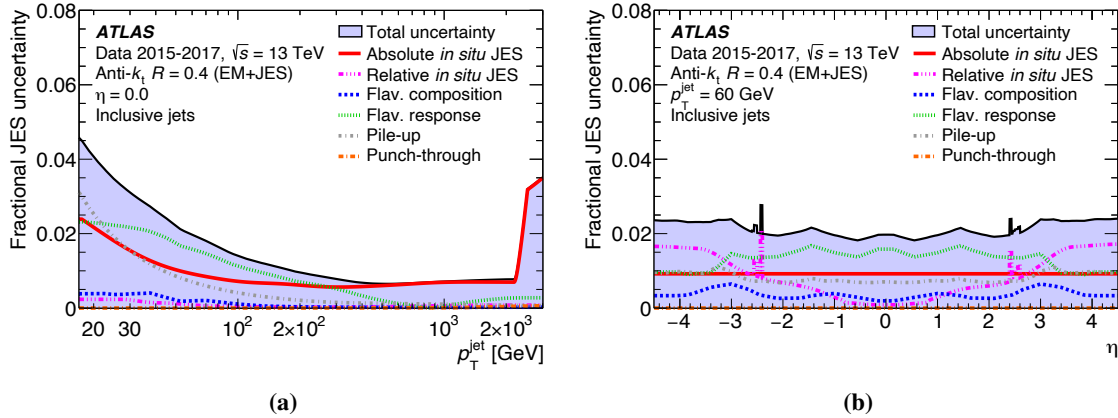


**Figure 5.8:** Uncertainty in the JES of fully calibrated jets as a function of (a) jet  $p_T$  at  $\eta = 0$  and (b)  $\eta$  at  $p_T = 80$  GeV [83]. The total uncertainty, which is all components summed in quadrature, is shown as a filled region with light blue. Each component is shown with different colors.

### 5.5.2 Track jet

The second type of jets is called the track jet. The track jets are constructed with an anti- $k_t$  algorithm with  $R = 0.4$  using all tracks with  $p_T > 1$  GeV and  $|d_0| < 2$  mm. Track jets have a stronger correlation with track density than calo jets and are used only in the inclusive background estimation described in Section 7.2.

Before finding the track jets, each track is associated to only one interaction point in order to minimize the probability of clustering tracks together in a single track jets originating from different interactions. The association proceeds as follows:

1. Tracks are assigned to a collision vertex if their longitudinal impact parameter significance  $|z_0/\sigma_{z_0}| < 3$  with respect to that vertex.
2. Any remaining unassociated tracks are assigned to a collision vertex if their longitudinal impact parameter satisfies  $|z_0| < 0.5$  mm with respect to that vertex.
3. If a track is found to be compatible with multiple collision vertices, the vertex with the highest  $S_{p_T}$  is chosen.

Then, the track jet finding is performed for each interaction point. Track jets are retained for further analysis if their  $p_T$  is larger than 20 GeV.

## 5.6 Overlap removal

Because muons, electrons, and jets are reconstructed independently using different algorithms, a single particle may be identified as two or more objects at the same time. The overlap removal is used to avoid the overlap of these objects. Track jets are excluded in the overlap removal procedure. The procedure can be separated in two steps, in order:

- Electron-muon: Electrons are removed if they share an inner detector track with a muon
- Electron-jet: Jets close to electrons are removed if they are within  $\Delta R (= \sqrt{(\Delta\eta)^2 + (\Delta\phi)^2}) < 0.2$  of an electron, in order to reject jets which originate from the calorimeter shower of the electron. In a subsequent step, electrons are removed if they are within  $\Delta R < 0.4$  of a remaining jet, in order to reject electrons which originate from hadronic decays.

# Chapter 6

## Event Selection

Events are selected using multiple high momentum jets and DVs.

### 6.1 Signal region definitions

This analysis defines two signal regions (SRs):

#### 1. High- $p_T$ SR:

- Events must pass the High- $p_T$  jet selection defined in Section 6.3
- Events must contain at least 1 DV passing all DV selections defined in Sections 6.4.1 and 6.4.3

#### 2. Trackless SR

- Events must pass the Low- $p_T$  and Trackless jet selections defined in Section 6.3
- Events must fail the High- $p_T$  jet selection defined in Section 6.3
- Events must contain at least 1 DV passing all DV selection defined in Section 6.4.1 and 6.4.3

The High- $p_T$  SR targets the gluino pair production model, in which high momentum jets are formed by the decay of heavy gluino. On the other hand, the electrowikino pair production model is expected to have jets with lower  $p_T$  on average. It is inefficient in the High- $p_T$  SR unless the neutralino mass is large. The Trackless SR is designed to recover sensitivity for this model. Both SRs are designed to include no background events derived from SM process while maintaining the selection efficiency of the targeted signal models as much as possible. In each SR, the signal is searched by estimating the expected number of background events and determining whether the number of events found in the actual data exceeds the estimate. From the next section, the definition of each selection and the signal efficiency in each SR is described.

### 6.2 Event trigger and jet filter

Events triggered by any of multi-jet triggers, each requiring from four to seven jets with various  $p_T$  thresholds, are used. Trigger thresholds were changed depending on the year since the jet trigger rate highly depends on the pile-up. The triggers with the lowest  $p_T$  threshold used for each year are listed in Table 6.1.

**Table 6.1:** Level-1 and HLT multi-jet triggers with the lowest  $p_T$  threshold in Run 2 [84, 85, 86].

Number of jets in HLT		Number of jets $\times p_T$ threshold [GeV]			
		2015	2016	2017	2018
4 jets	L1 threshold	$3 \times 40$	$3 \times 50$	$3 \times 50$	$3 \times 50$
	HLT threshold	$4 \times 100$	$4 \times 100$	$4 \times 100$	$4 \times 120$
5 jets	L1 threshold	$4 \times 20$	$4 \times 15$	$4 \times 15$	$4 \times 15$
	HLT threshold	$5 \times 60$	$5 \times 70$	$5 \times 70$	$5 \times 85$
6 jets	L1 threshold	$4 \times 15$	$4 \times 15$	$4 \times 15$	$4 \times 15$
	HLT threshold	$6 \times 45$	$6 \times 60$	$6 \times 60$	$6 \times 70$
7 jets	L1 threshold	-	$4 \times 15$	$4 \times 15$	$4 \times 15$
	HLT threshold	-	$7 \times 45$	$7 \times 45$	$7 \times 45$

As the LRT reconstruction algorithm which is dedicated technique to reconstruct tracks derived from LLPs decay is computationally expensive, and it cannot be run on all events recorded with the ATLAS detector. Instead, a selection referred to as a *filter* is applied to the events satisfying the trigger conditions described in Table 6.1. The events passing the filter requirements are processed with LRT. This analysis utilizes two filters: the high- $p_T$  and the trackless jet filters.

The high- $p_T$  jet filter targets the gluino pair production model. This filter requires that events have been triggered by any of the multi-jet triggers and that it has a certain number of reconstructed jets above some  $p_T$  thresholds listed as high- $p_T$  jet filter in Table 6.2. The uncalibrated jet  $p_T$  is used in this filter and the thresholds are chosen to reduce the rate of events to a manageable level.

The trackless jet filter targets the electroweakino pair production model. This filter also requires events to pass any of the multi-jet triggers and jets to pass requirements on multiplicity and  $p_T$  listed as low- $p_T$  jet filter in Table 6.2, that are looser  $p_T$  thresholds than ones for the high- $p_T$  jet filter. To compensate the reduced  $p_T$  thresholds, an additional requirement is applied. The events must have at least one "trackless jet" with  $p_T \geq 70$  GeV and  $|\eta| < 2.5$ , or at least two trackless jets with  $p_T \geq 50$  GeV and  $|\eta| < 2.5$ . If the sum of  $p_T$  of all standard (not reconstructed by LRT) tracks associated to the jet is less than 5 GeV, the jet is regarded as a "trackless jet". Tracks with  $p_T > 500$  MeV are used in the sum.

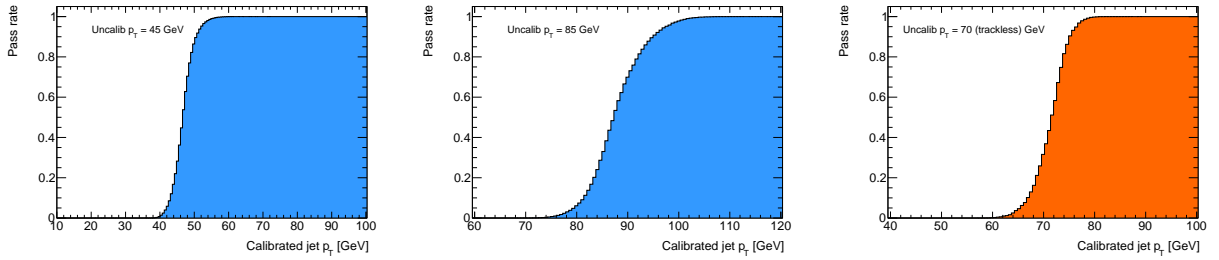
### 6.3 Jet selections

Events are required to have four to seven or more calibrated jets. Jet  $p_T$  after calibration may be higher than one before calibration. The  $p_T$  thresholds for calibrated jets are adjusted. The  $p_T$  thresholds are chosen not to remove events as much as possible that satisfy the jet filter requirement. To do this, the rate of jets that satisfies the  $p_T$  threshold of jet filter is derived as a function of the calibrated jet  $p_T$ , and the  $p_T$  threshold for the calibrated jet is set to the  $p_T$  where the rate is greater

**Table 6.2:** Uncalibrated jet multiplicity and  $p_T$  thresholds for the low- $p_T$  and high- $p_T$  jet filter.

Number of uncalibrated jets	Low- $p_T$ jet filter $p_T$ threshold [GeV]	High- $p_T$ jet filter $p_T$ threshold [GeV]
4	100	220
5	75	170
6	50	100
7	45	75

than 98%. The cases of three different thresholds for uncalibrated jets are shown in Figure 6.1. Only jets which pass the jet cleaning and overlap removal described in Section 5.5.1 are used to study the  $p_T$  thresholds. The  $p_T$  thresholds of the calibrated trackless jets are determined by the same method. Thresholds of calibrated jets for low- $p_T$  and high- $p_T$  jet selections are summarized in Table 6.3, and trackless jet selection is summarized in Table 6.4.

**Figure 6.1:** The rate at which jets with calibrated  $p_T$  shown in the horizontal axis pass the uncalibrated  $p_T$  threshold, for three thresholds used by the jet filter. The left and middle plots (blue) show the turn-on curve for normal jets. The rightmost plot (orange) shows the turn-on curve for trackless jets.**Table 6.3:** Calibrated jet multiplicity and  $p_T$  thresholds for the low- $p_T$  and high- $p_T$  jet selections.

Number of calibrated jets	Low- $p_T$ jet selection $p_T$ threshold [GeV]	High- $p_T$ jet selection $p_T$ threshold [GeV]
4	137	250
5	101	195
6	83	116
7	55	90

**Table 6.4:** Calibrated jet multiplicity and  $p_T$  thresholds of calibrated jets for the trackless jet selections.

Number of calibrated jets	Trackless jet selection $p_T$ threshold [GeV]
1	56
2	78

## 6.4 DV selections

In this analysis, the vertex created at a distance of  $O(1)$ – $O(100)$  mm from the interaction point is called the DV. This section describes the selections for DVs. The DV is selected mainly by the position, the number of tracks constituting the DV, and the invariant mass, which is calculated by assuming the charged pion mass from the four-momentum vector of the constituting tracks. Hereafter, the number of tracks constituting the DV is referred to as the "multiplicity" ( $N_{\text{Trk}}$ ) of the DV, and the invariant mass calculated from the tracks is referred to as the "mass" ( $m_{\text{DV}}$ ) of the DV.

### 6.4.1 Baseline DV selection

DVs must be reconstructed with a high position quality of  $\chi^2/n_{\text{DoF}} < 5$  to reject fake vertices. The reconstructed DV must be within a fiducial region, which is before SCT detector defined as  $R_{xy} = \sqrt{x_{\text{DV}}^2 + y_{\text{DV}}^2} < 300$  mm and  $|z_{\text{DV}}| < 300$  mm, where  $x_{\text{DV}}$ ,  $y_{\text{DV}}$ ,  $z_{\text{DV}}$  represent the position of the DV. In addition, the DV must be at least 4 mm from all primary vertices in the event to reduce the background events containing the heavy flavour SM particles which have a long lifetime.

Hadronic interactions with detector material can produce DVs with large track multiplicities. These DVs are difficult to distinguish from long-lived particle decays, and constitute a major background to the analysis. In order to reduce the contribution of hadronic interactions, it is essential to reject vertices found inside regions of detector material. The material map, shown in Figure 6.2, is constructed using the known positions of detector elements and from the positions of low-mass DVs reconstructed in data. The requirement of low-mass DV is shown in the following:

- $m_{\text{DV}} < 2.5$  GeV
- DVs reconstructed from two tracks and with  $0.45 < m_{\text{DV}} < 0.55$  GeV are vetoed for  $K_S^0$  suppression.
- DVs reconstructed from three tracks are rejected if the largest opening angle between constructing tracks is less than 0.15 rad or  $m_{\text{DV}} < 0.95$  GeV in order to reduce backgrounds from photon conversions.

The material map occupies 48% of the fiducial region. DVs existing in the material map are removed (called "material map veto").

A material map built from simulated MC events is also used in this analysis. The material map for MC is needed because the simulated detector does not match perfectly the physical detector.

The MC material map is built from the true positions of interactions rather than the reconstructed positions, which means that the material structures are thinner. Therefore, it does not remove material interactions as efficiently as the data material map does. The MC material map occupies 23% of the fiducial region. It is only used in the validation of the data-driven background estimates using MC described in Section 7.4.2.

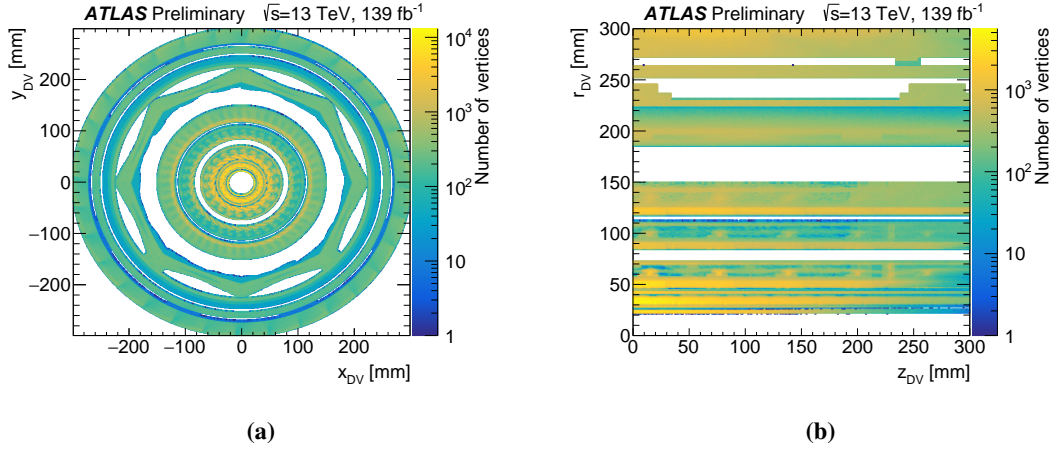


**Figure 6.2:** The positions of detector elements and reconstructed low-mass vertices in the (a)  $x - y$  plane and (b)  $r - z$  plane. DVs located in the colored areas are removed. The right figure is restricted to positive  $z$  values for presentation. The innermost area corresponds to the beampipe. This is surrounded by four pixel detector layers. The octagonal shape and outermost structures are due to support structures separating the pixel and SCT detectors.

A summary of the baseline DV selections is shown in Table 6.5.

**Table 6.5:** Summary of the baseline DV selections.

Within a fiducial region	$R_{xy} < 300 \text{ mm},  z  < 300 \text{ mm}$
Distance from any primary vertices	$> 4 \text{ mm}$
Vertex fit quality	$\chi^2/N_{\text{DoF}} < 5$
Material veto	Outside material map

### 6.4.2 DV-track selection

To reject fake DVs, while maintaining a high efficiency for DVs in the signal process, track selections are applied to DVs after baseline DV selections. Only tracks satisfying specific quality selections, summarized in Table 6.6, are used in the calculation of the DV track multiplicity and mass. As the background composition changes in different parts of the detector, these selections depend on the  $R_{xy}$  position of the DV ( $R_{DV}$ ), with different criteria before and after the beampipe ( $R = 25 \text{ mm}$ ) and the last pixel layer ( $R = 145 \text{ mm}$ ). Further requirements, aimed at rejecting wrong track-to-vertex associations, are applied on the azimuthal difference  $\Delta\phi_{PV-DV}$  between the track direction and the

vector connecting the primary vertex to the displaced vertex.

**Table 6.6:** Summary of the track selections used for signal DV candidates. The track  $d_0$ -significance is given by  $|d_0|/\sigma(d_0)$ . The selected tracks are the tracks that were used to reconstruct the first seed vertex. The attached tracks are low-quality tracks that were added to the DV later.

†: if the azimuthal difference between the track direction and the vector connecting the primary vertex to the displaced vertex is small ( $\Delta\phi_{\text{PV-DV}} < 0.2$ ), the requirement for  $p_T$  is tightened to  $p_T > 4$  GeV.

Region		$0 < R_{\text{DV}} < 25$ mm	$25 < R_{\text{DV}} < 145$ mm	$R_{\text{DV}} > 145$ mm
Attached tracks	Track $p_T$ [GeV]	$> 2$	$> 3^\dagger$	$> 4$
	Track $d_0$ -significance	$> 10$	$> 15$	-
	Backward going tracks	$\Delta\phi_{\text{PV-DV}} < \pi/2$		
	Upstream hit veto	No hits allowed with $R < R_{\text{DV}}$		
Selected tracks	Track $p_T$ [GeV]	$> 2$	$> 2^\dagger$	$> 2$
	Track $d_0$ -significance	$> 10$	-	$> 10$
	Upstream hit veto	No hits allowed with $R < R_{\text{DV}}$		

Figure 6.3 shows the DV selection efficiency, where the recalculated DV mass and track multiplicity satisfy the requirements of  $m_{\text{DV}} > 5$  GeV and  $N_{\text{Trk}} \geq 5$ , or  $m_{\text{DV}} > 10$  and  $N_{\text{Trk}} \geq 4$ , when each DV-track selection is applied in sequence. The selection efficiency satisfying baseline DV selection and the requirements of DV mass and multiplicity is set as 1. The bin labeled *baseline* refers to the baseline DV selections described in Section 6.4.1. The following bins mean the DV-track selections. The last bin requires that at least 2 selected tracks remain in the DV after the all DV-track selections have been applied. The signal samples in the plot are combined gluino masses of 1600 GeV and 1800 GeV as well as neutralino lifetimes of 0.01, 0.1, 1, and 10 ns to gain statistics. This combination doesn't affect the DV properties significantly except for  $R_{\text{xy}}$ . In this study, DVs in the individual radial regions are treated separately, and the differences in  $R_{\text{xy}}$  due to combination doesn't affect the selection efficiency.

### 6.4.3 Final DV selection

To exclude the background events containing the DVs not derived from signal process, the DVs are required to have at least two selected tracks<sup>\*1</sup>, at least five tracks combined selected and attached tracks, and DV mass  $> 10$  GeV. Since there are no long-lived SM particles with masses heavier than 10 GeV, this selection is effective in reducing DV derived from the SM process.

\*1 the tracks that were used to reconstruct the first seed vertex



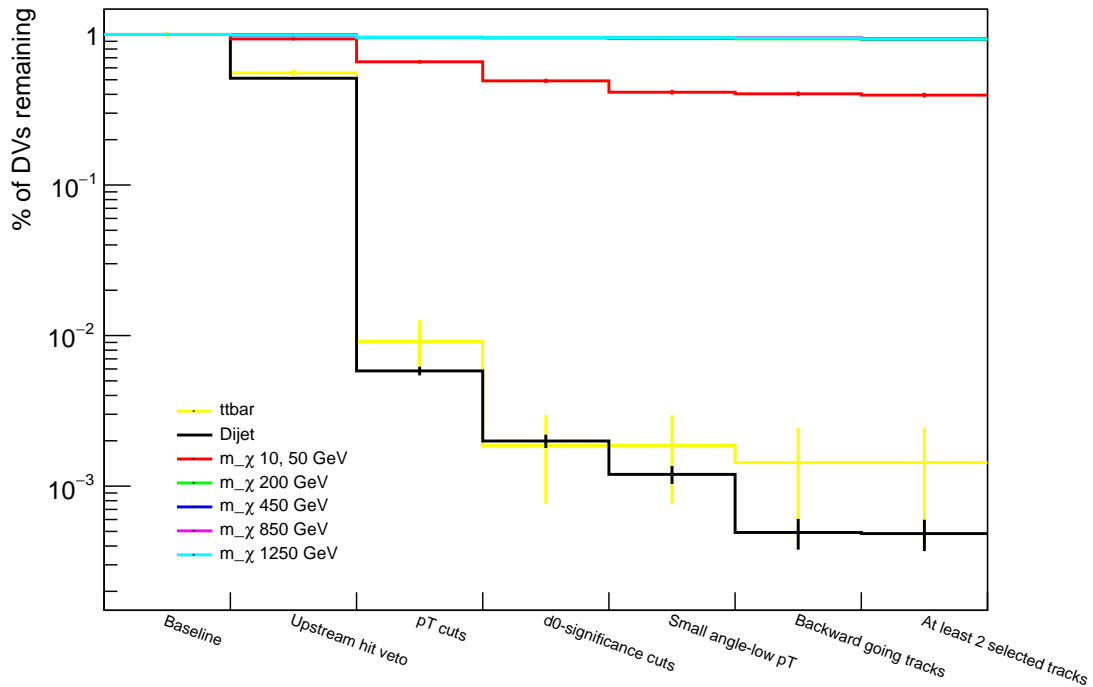


**Figure 6.3:** Cutflow of different MC samples with DV-track selection applied sequentially for SM process samples and signal samples. The strong pair production model are used as the signal samples, and combined gluino masses of 1600 GeV and 1800 GeV as well as neutralino lifetimes of 0.01, 0.1, 1, and 10 ns to gain statistics. The higher mass neutralino samples are all overlapping at the top, closely following the line of sample with  $\tilde{\chi}_1^0$  mass of 1250 GeV.

## 6.5 Signal efficiencies

Figure 6.4 shows the DV selection efficiency satisfying the baseline and final DV selections with and without attached tracks described in Section 5.3.2. The efficiency is significantly increased by using attached tracks.

Figure 6.5 shows the selection efficiencies after sequentially applying each criteria in the High- $p_T$  SR, as a function of neutralino mass and lifetime in the gluino pair production model. The gluino mass is fixed at 2600 GeV.

Table 6.7 shows the cutflow table for the both of the Trackless and High- $p_T$  SR for a few representative point of the electrowikino pair production model. For neutralino masses of a few hundred GeV, the Trackless SR is the most powerful signal region, albeit still not fully efficient due to the rather soft  $p_T$  spectrum of jets expected in this model. Above about 1 TeV the High- $p_T$  SR is more efficient at selecting events also for this signal model, showing the complementarity of the two signal regions for this model. Figure 6.6 shows in detail the selection efficiency for the electrowikino pair production model after a few of the most important requirements, as a function of the neutralino mass and lifetime, further corroborating the observations above.

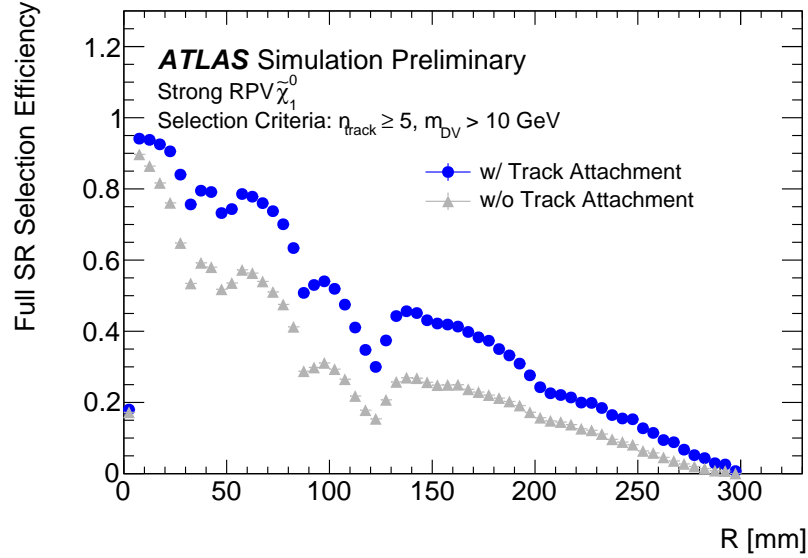


**Figure 6.4:** DV selection efficiency for the baseline and final DV selection for neutralinos produced via gluinos with and without attached tracks. With track attachment, the number of tracks from the DVs and the visible DV mass is calculated from the selected and attached tracks. On the other hand, in the histogram showing the performance without track attachment, the number of tracks and DV mass is calculated only from the selected tracks.

**Table 6.7:** The efficiencies for passing the various selection criteria in the Trackless SR (High- $p_T$  SR); a few representative points of the electrowikino pair production model are shown. Note that the "trackless jets" selection includes the requirement not to pass the "high- $p_T$ " jet selection to make the two regions orthogonal.

	$m(\tilde{\chi}_1^0) = 500$ GeV, $\tau(\tilde{\chi}_1^0) = 1$ ns	$m(\tilde{\chi}_1^0) = 700$ GeV, $\tau(\tilde{\chi}_1^0) = 0.1$ ns	$m(\tilde{\chi}_1^0) = 1300$ GeV, $\tau(\tilde{\chi}_1^0) = 1$ ns	$m(\tilde{\chi}_1^0) = 1700$ GeV, $\tau(\tilde{\chi}_1^0) = 0.1$ ns
Initial	1.000	1.000	1.000	1.000
Pass Trigger	0.869	0.982	0.999	0.999
Pass trackless (high- $p_T$ ) jet filter	0.867 (0.140)	0.936 (0.434)	0.997 (0.958)	0.930 (0.993)
Pass trackless (high- $p_T$ ) jets selection	0.399 (0.058)	0.536 (0.234)	0.172 (0.803)	0.062 (0.923)
$R_{\text{DV}} < 300$ mm && $ z_{\text{DV}}  < 300$ mm	0.348 (0.051)	0.530 (0.231)	0.162 (0.755)	0.061 (0.909)
DV > 4 mm from PV	0.345 (0.050)	0.517 (0.228)	0.161 (0.751)	0.060 (0.887)
$\chi^2/N_{\text{DoF}} < 5$	0.334 (0.049)	0.515 (0.228)	0.157 (0.734)	0.060 (0.884)
Pass material veto	0.234 (0.033)	0.459 (0.199)	0.117 (0.546)	0.054 (0.785)
$n_{\text{Trk}} \geq 5$	0.145 (0.020)	0.416 (0.180)	0.083 (0.379)	0.049 (0.698)
$m_{\text{DV}} > 10$ GeV	0.143 (0.019)	0.414 (0.179)	0.083 (0.375)	0.048 (0.696)

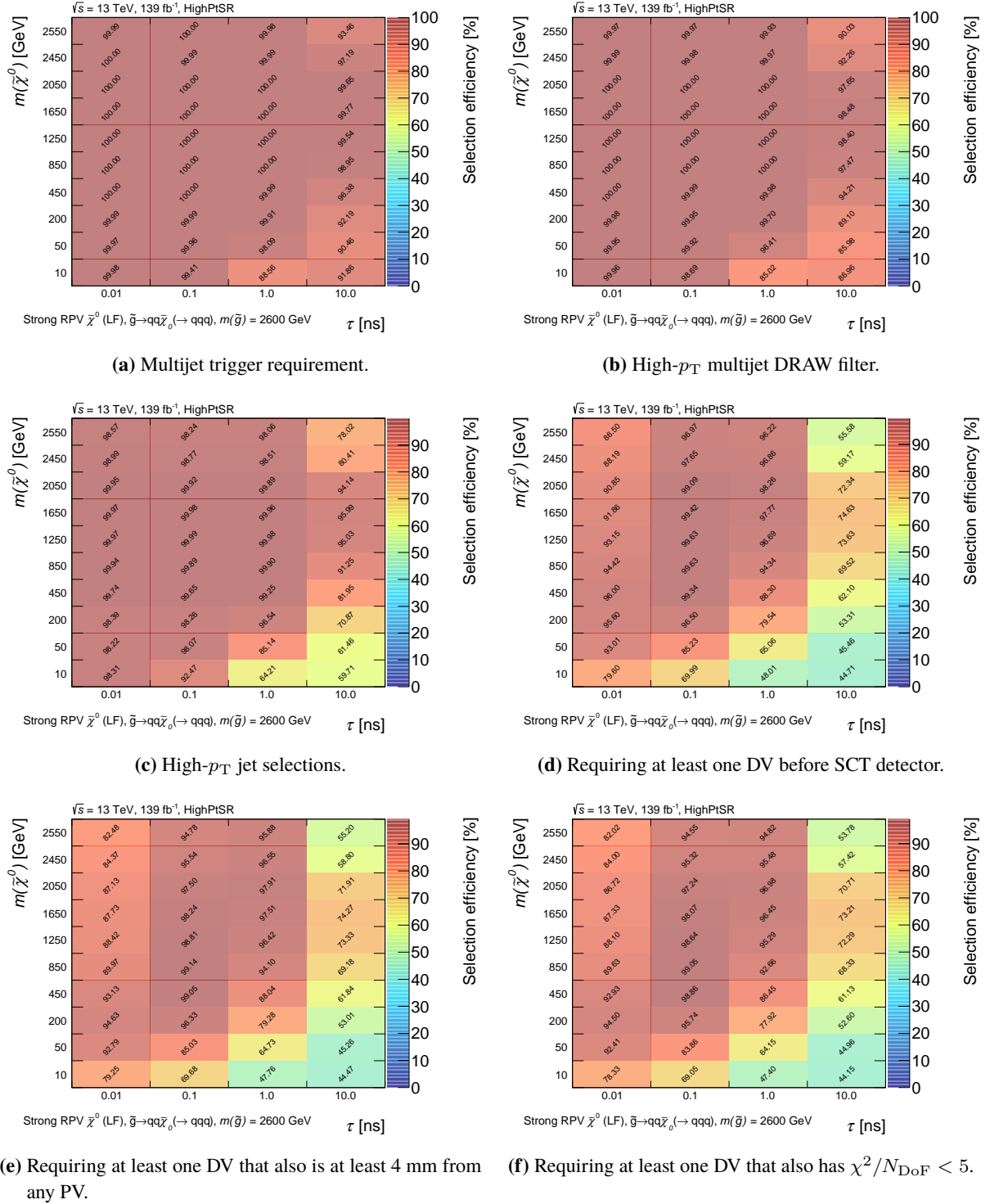
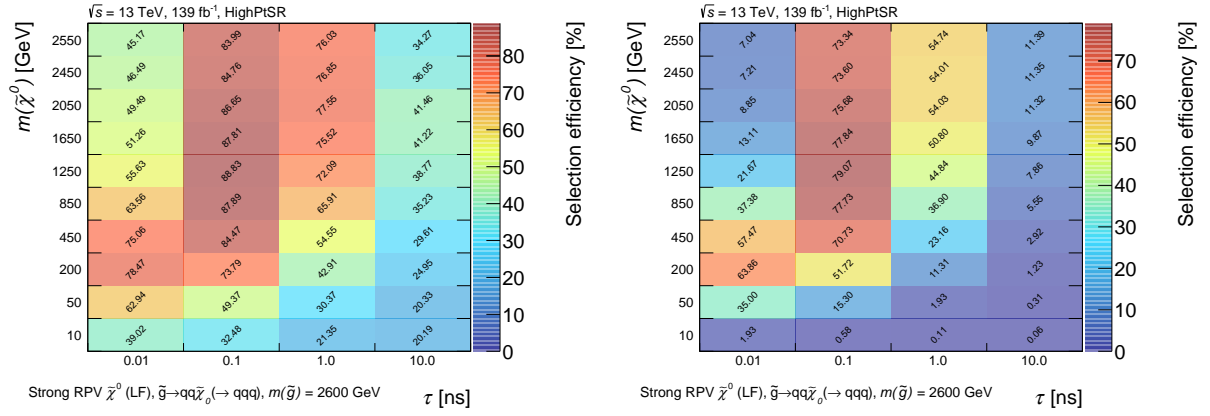
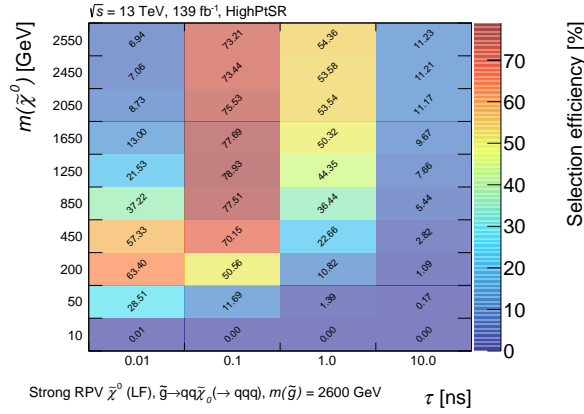


**Figure 6.5:** Selection efficiency for the gluino pair production model after applying each of the selection criteria in the High- $p_T$  SR as a function of neutralino mass and lifetime. The gluino mass is fixed at 2600 GeV. Note that each plot shows the cumulative efficiency of all selections up to the one displayed.

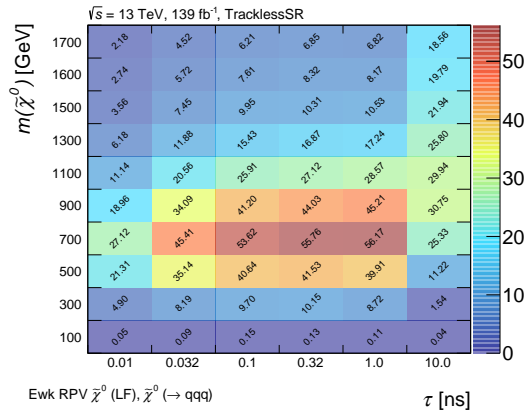


(g) Requiring at least one DV that also passes the material veto. (h) Requiring at least one DV that also has 5 or more tracks.

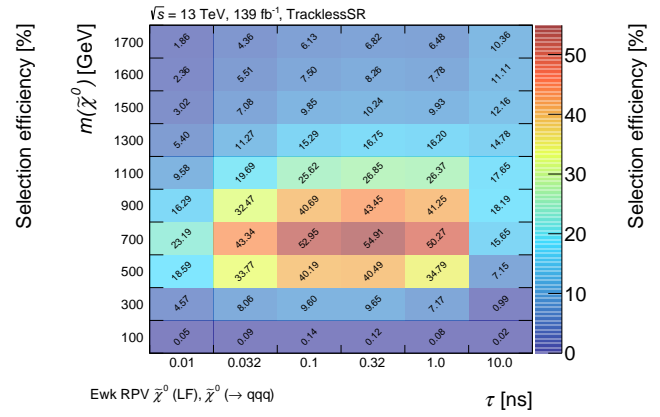


(i) Requiring at least one DV that also has  $m_{DV} > 10$  GeV.

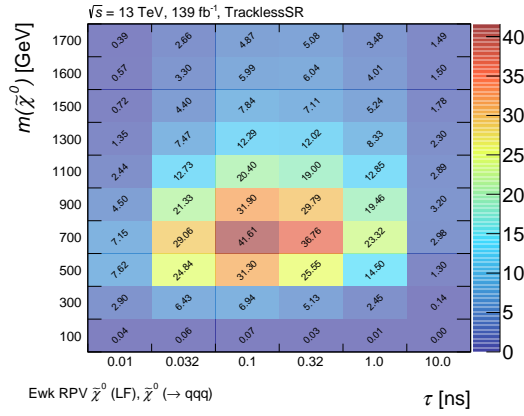
**Figure 6.5:** (Cont'd) Selection efficiency for the gluino production signal scenarios after applying each of the selection criteria of the High- $p_T$  SR as a function of neutralino mass and lifetime. The gluino mass is fixed at 2600 GeV. Note that each plot shows the cumulative efficiency of all selections up to the one displayed.



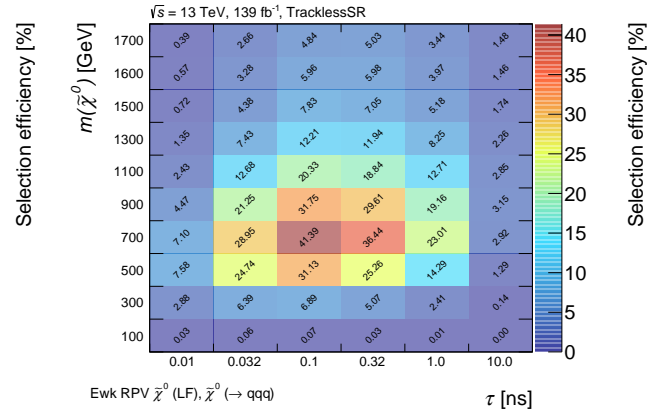
(a) Trackless jet selections.



(b) Requiring at least one DV before SCT detector.



(c) Requiring at least one DV that also has 5 or more tracks.

(d) Requiring at least one DV that also has  $m_{\text{DV}} > 10 \text{ GeV}$ .

**Figure 6.6:** Signal efficiencies for the electrowikino pair production model as a function of neutralino mass and lifetime after a few of the most important selections defined in the Trackless SR. Note that each plot shows the cumulative efficiency of all selections up to the one displayed.

## Chapter 7

# Background estimation

### 7.1 Background classification

There are no heavy SM particles which decay with long lifetime. Dominant backgrounds in this analysis are multi-jets events including DVs reconstructed by instrumental and algorithmic effects from three main sources shown in Figure 7.1.

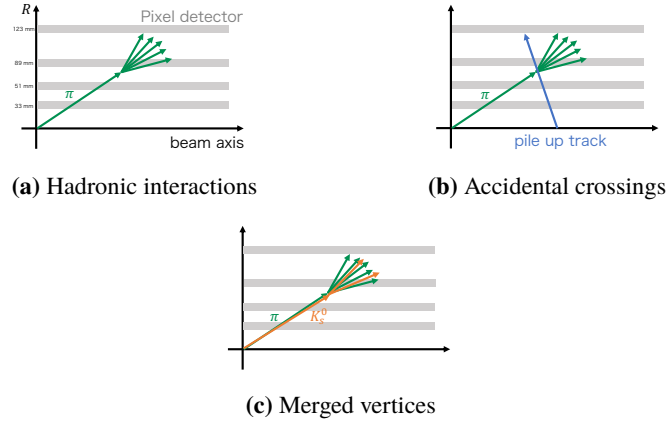


**Figure 7.1:** Background classification of (a) Hadronic interactions (b) Accidental crossings (c) Merged vertices.

#### (a) Hadronic interactions

Hadronic interactions arise from particles interacting with the nuclei of detector material or air. If charged particles are produced in this interaction, they may be used for the reconstruction of a displaced vertex. The charged particles produced from this interaction are typically collimated, and the DV mass, which is the invariant mass calculated from the associated tracks, becomes relatively small. Rarely, the decay products are not collimated and high-mass DVs are reconstructed. The bulk of these DVs is located in the high material-density regions of the detector and tracks derived from these DVs are removed by the material map veto described in Section 6.4.1. The remaining DVs are either due to hadronic interactions in the low material-density regions, or avoidance of material map veto due to the resolution of the vertex position. The number of these DVs that pass the DV selections needs to be estimated.

### (b) Accidental crossings

The mass of DVs created from the actual DV originating from long-lived SM particle decays or hadronic interactions is low ( $\lesssim 5$  GeV). However, when an unrelated track crosses accidentally with these DVs at large angle, the mass of DVs becomes higher. DVs created in this way are called DVs derived from accidental crossings, and these DVs are more likely to pass the DV selections.

### (c) Merged vertices

Two actual vertices that are close together may be reconstructed as a single vertex by the vertexing algorithm. These DVs are called merged vertices. The vertices from decays of long-lived SM particles or hadronic interactions may be merged by the vertexing algorithm, and a single high-mass DV that satisfies the SR selection is created.

The probability that an event includes at least one DV is correlated to the presence of track jets. Figure 7.2 shows the fraction of events which contain a SR-like DV in the events triggered by single photon trigger ( $E_T > 140$  GeV) as a function of track jet multiplicity. "SR-like DVs" are those which pass the baseline DV selection and have high mass and high multiplicity. This plot shows that events with more track jets are more likely to contain a SR-like DV. The next section describes the method to estimate the number of background events including DVs inclusively using this trend.

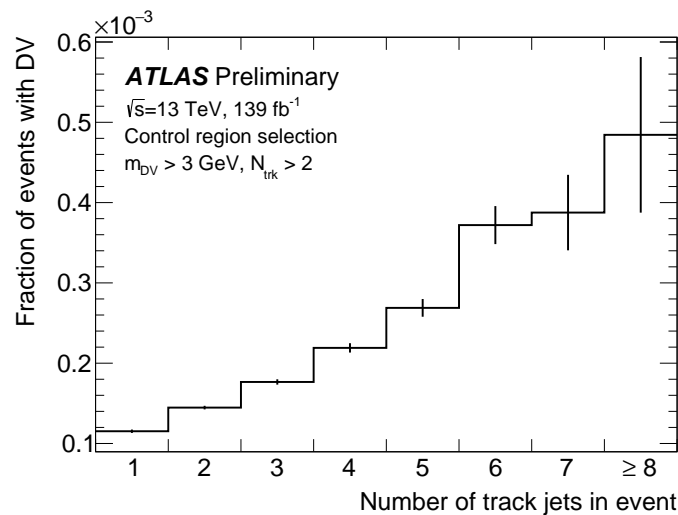


**Figure 7.2:** The fraction of events triggered by single photon trigger which contain a DV satisfying the baseline DV selection,  $m_{DV} > 3$  GeV, and  $N_{Trk} > 2$ .

## 7.2 Inclusive background estimation method

This estimation technique works in two steps:

1. The "track jet-DV probability", which is the probability of a SR-like DV being generated near

the track jet, is calculated using the number of track jets and DVs in the Control Region (CR) of the data.

2. The total number of expected background events including DVs is estimated by applying the track jet-DV probability to the number of track jets in events passing the jet selections of the SRs. The track jet-DV probability is a very small value. The probability of reconstructing more than one DV for a single multi-jet event is so small that the estimated number of DVs can be treated as the estimated number of events.

### 7.2.1 Calculation of track jet-DV probability

The track jet-DV probability is calculated using events containing three or more track jets in the Photon-triggered CR. The photon-triggered CR is populated with events which satisfy the following selection. **Photon-triggered CR:**

- Passes single photon trigger with  $E_T > 140$  GeV
- Fails both SR selections
- At least 3 track jets with  $p_T > 20$  GeV

Single photon trigger is selected because it is not expected to significantly alter the composition of jets in the control region with respect to the signal region. This CR is designed to contain track jets and limit the contamination from signal models of interest.

Differences in track jet properties in CR and SRs were identified. Figure 7.3 shows the track jet multiplicity, track jet  $p_T$ , and a number of tracks per track jet in the CR and in events passing the jet selections of the SRs defined in Section 6.3. Although the events in the CR have on average fewer track jets than events passing the jet selections of the SRs, this method allows the track jet-DV probability to be calculated as a value that also includes differences in track jet multiplicity within events. Therefore, differences in track jet multiplicity between the CR and the SRs can be prevented from affecting the estimates. The impact of the difference in track jet multiplicity will be tested and taken as a systematic uncertainty in Section 7.3. The events passing the jet selections of the High- $p_T$  SR have track jets with higher  $p_T$  and consisting of more tracks than those in the CR. Conversely, the events passing the jet selections of the Trackless SR have track jets with slightly lower  $p_T$  and consisting of fewer tracks than those in the CR. The track jet-DV probability is parameterized as a function of both of the track jet  $p_T$  and a number of tracks per track jet in order to take into account these differences.

The track jet-DV probability that a DV is produced given the presence of a track jet is calculated in the CR from the following formula:

$$\text{Prob ( DV | track jet )} = \frac{\text{Number of DVs matched to a track jet}}{\text{Total number of track jets}} . \quad (7.1)$$

The SR-like DVs in the CR are matched to the closest track jet in the event using the  $\Delta R_{\text{DV,jet}} (= \sqrt{\Delta\eta^2 + \Delta\phi^2})$ , where  $\Delta\eta$  and  $\Delta\phi$  are measured between the direction of the DV from a PV and



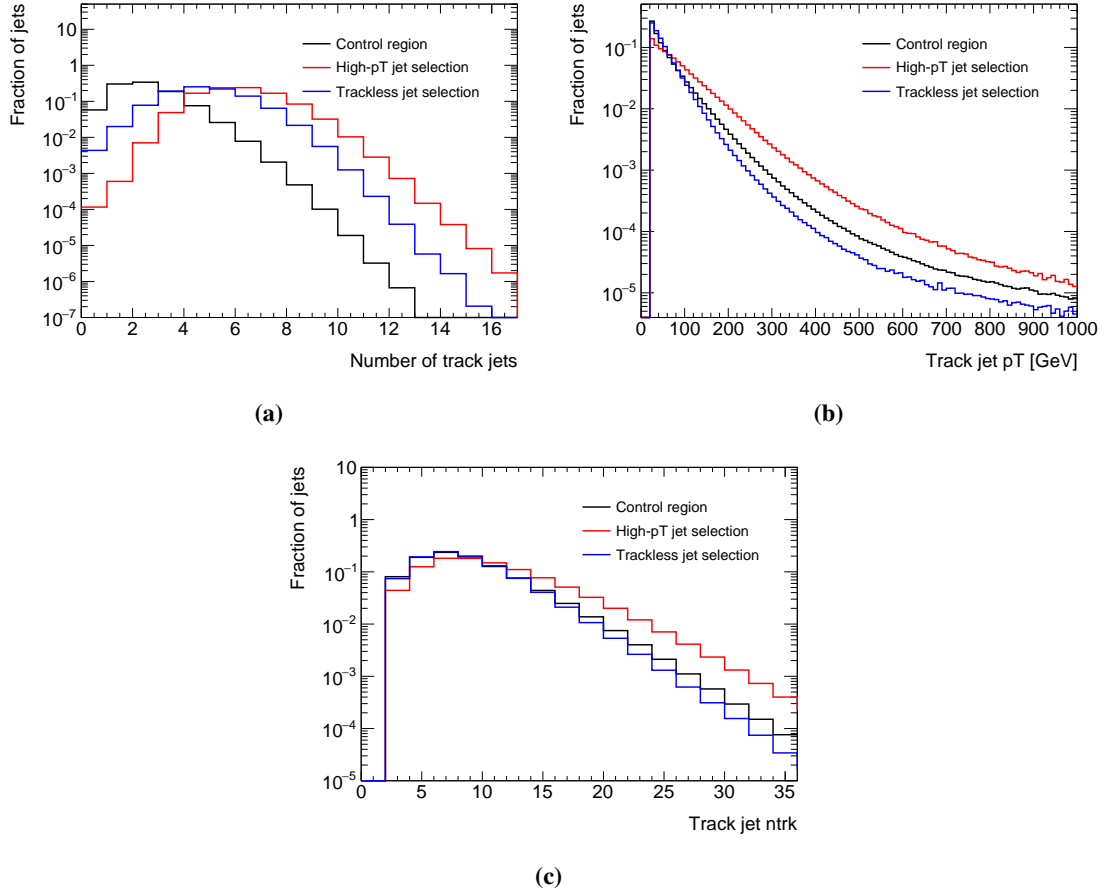


**Figure 7.3:** A comparison of the track jet (a) multiplicity, (b)  $p_T$ , and (c) a number of tracks per track jet in the control region and in events passing the jet selections of the High- $p_T$  and Trackless SRs. All distributions are used the full Run-2 dataset and are normalized by the integration of the distributions.

the axis of the track jet. Each DV is matched to only one track jet in each event. The track jet-DV probability parameterized as a function of the number of tracks in the jet and track jet  $p_T$  are shown in Figures 7.4 and 7.5, respectively. The track jet-DV probability in Figure 7.4 is calculated using the number of tracks in the track jet for all track jets as the denominator and the number of tracks in the track jet closest to the DV that satisfies the mass and multiplicity requirements written in the plots as the numerator. DVs with high mass and high track multiplicity are more likely to be produced near track jets consisting of more tracks (from Figure 7.4) and having moderate  $p_T$  (from Figure 7.5). It is also observed that the shape of the track jet-DV probability changes for different DV masses and track multiplicities. This indicates that separate track jet-DV probability distributions need to be derived for each of DV with different mass and track multiplicity. For example, in order to estimate the number of the events with DVs reconstructed from four tracks in the events passing the jet selections of the SRs, the track jet-DV probability is calculated using only DVs reconstructed from four tracks in the CR.

The track jet-DV probability to estimate the number of the background events in the SRs is calculated

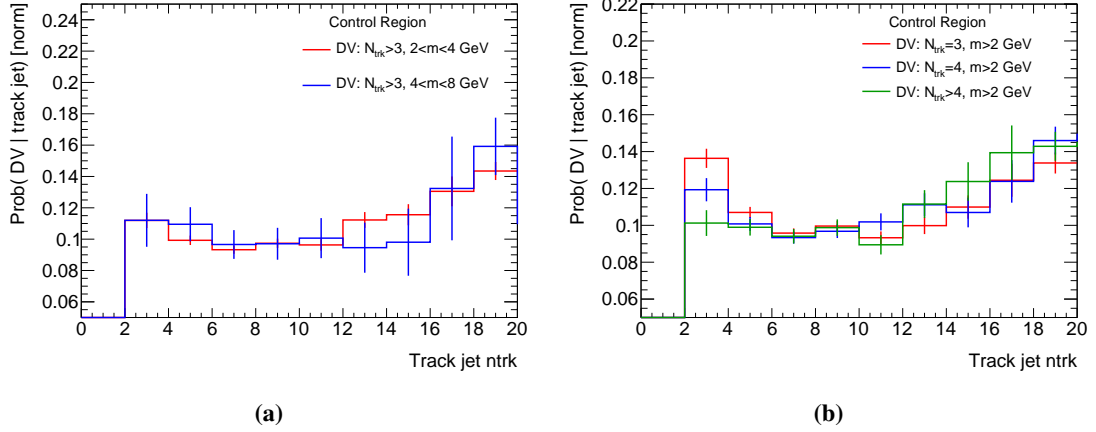


**Figure 7.4:** The track jet-DV probability as a function of the number of tracks in the track jet, for DVs of various (a) masses ( $m$ ) and (b) track multiplicities ( $N_{\text{Trk}}$ ), calculated using events in the CR with the full Run-2 dataset. Each distribution is normalized by the integration of the distributions. The last bin includes the overflow.

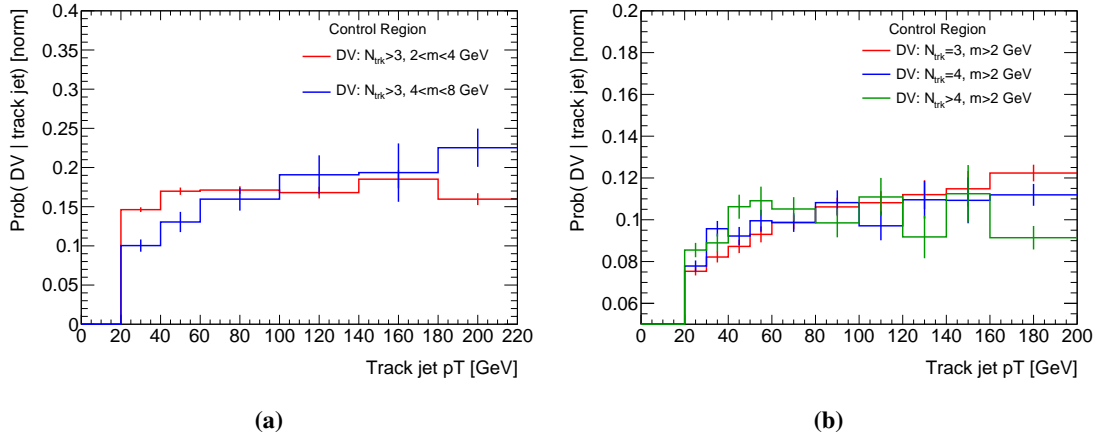


**Figure 7.5:** The track jet-DV probability as a function of the track jet  $p_T$ , for DVs of various (a) masses ( $m$ ) and (b) track multiplicities ( $N_{\text{Trk}}$ ), calculated using events in the CR with the full Run-2 dataset. Each distribution is normalized by the integration of the distributions. The last bin includes the overflow.

using all DVs satisfying  $N_{\text{Trk}} > 3$  and  $m_{\text{DV}} > 5$  GeV in the CR. The requirements of the DV mass and track multiplicity in the CR are looser than the requirements in the SRs ( $N_{\text{Trk}} > 4$  and  $m_{\text{DV}} > 10$  GeV) to ensure sufficient statistics to calculate the track jet-DV probability. Although earlier it is mentioned that the shape of the track jet-DV probability changes depending on the mass and multiplicity of the DVs, the change is sufficiently smaller than the change due to the statistical uncertainty in the number of DVs in the above mass and multiplicity region. The number of DVs matched to a track jet in the CR is shown in Figure 7.6(a). The total number of track jets is shown in Figure 7.6(b). The track jet-DV probability shown in Figure 7.6(c) is calculated by dividing Figure 7.6(a) by Figure 7.6(b). The track jet-DV probability is very small ( $\mathcal{O}(10^{-6})$ ) because the SR-like DVs are rare and the number of jets

produced in the ATLAS detector is very high.

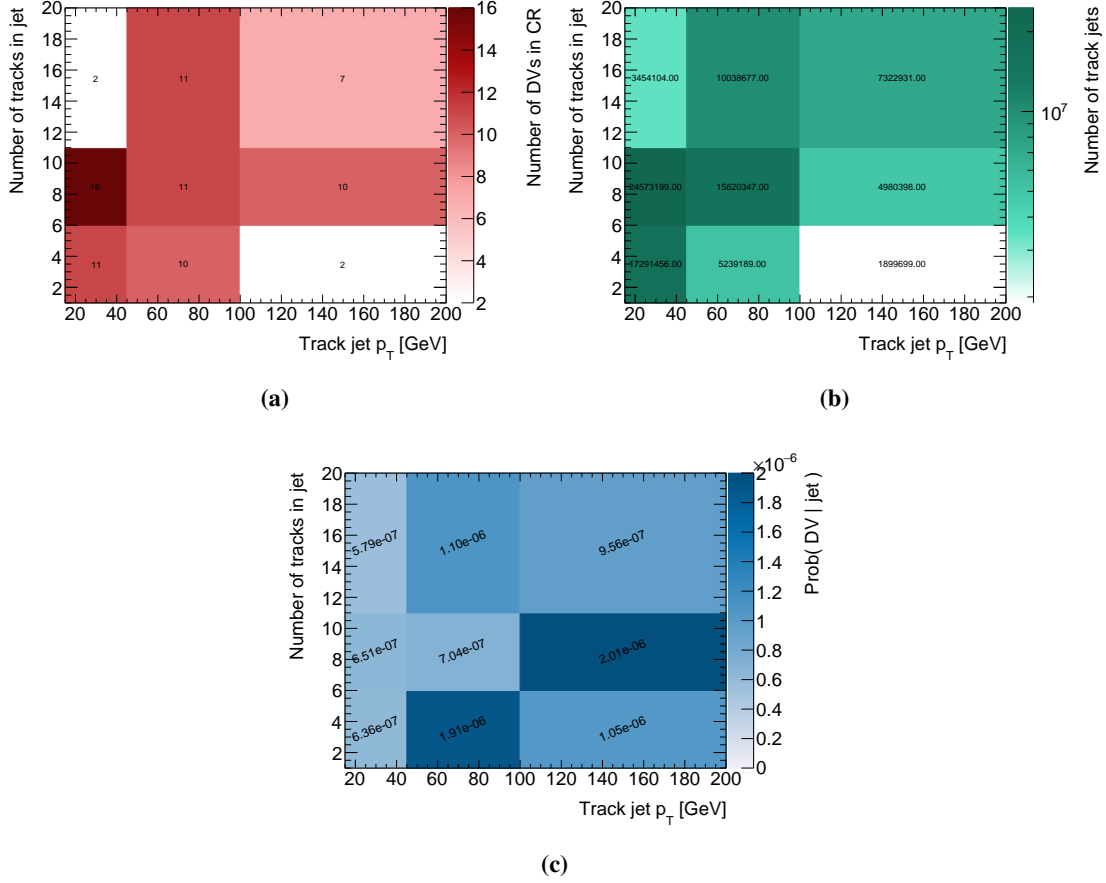


**Figure 7.6:** (a) The number of DVs satisfying  $N_{\text{Trk}} > 3$  and  $m_{\text{DV}} > 5$  GeV matched to a track jet, (b) the total number of track jets, (c) the track jet-DV probability of DVs satisfying  $N_{\text{Trk}} > 3$  and  $m_{\text{DV}} > 5$  GeV in the CR.

## 7.2.2 Estimation of the number of the background events in the SRs

The estimated number of events with a SR-like DV is the total number of track jets in events passing the jet selections of the SRs times the track jet-DV probability. This means it is calculated using the following formula:

$$N_{\text{Bkg}} = f \cdot \sum_{i=0}^{N_{\text{track jet}}} P(\text{DV} | \text{jet}_i), \quad (7.2)$$

where  $f$  is an additional weight which takes into account the difference in the DV mass and track multiplicity requirements used in the calculation of the track jet-DV probability and in the SR selection. It is calculated by taking the ratio of the number of events satisfying the requirements of  $m_{\text{DV}} > 10$  GeV and  $N_{\text{Trk}} > 4$  to ones satisfying the requirements of  $m_{\text{DV}} > 5$  GeV and  $N_{\text{Trk}} > 3$  in

the CR:

$$f = \frac{N_{\text{Event}}(m_{\text{DV}} > 10 \text{ GeV}, N_{\text{track}} > 4)}{N_{\text{Event}}(m_{\text{DV}} > 5 \text{ GeV}, N_{\text{track}} > 3)} \text{ in CR} = 3/80 = 0.0375. \quad (7.3)$$

The probability that more than one SR-like DV is produced in the same event is negligible.

The number of track jets as a function of track jet  $p_T$  and the number of tracks in a track jet in events passing the jet selections of the High- $p_T$  and Trackless SRs are shown in Figures 7.7(a) and 7.8(a), respectively. Figures 7.7(b) and 7.8(b) are after applying the track jet-DV probability and  $f$  factor, and the sum of bin contents is the estimated number of the background events in each SR. The total number of background events are 0.49 in the High- $p_T$  SR, and 0.69 in the Trackless SR.

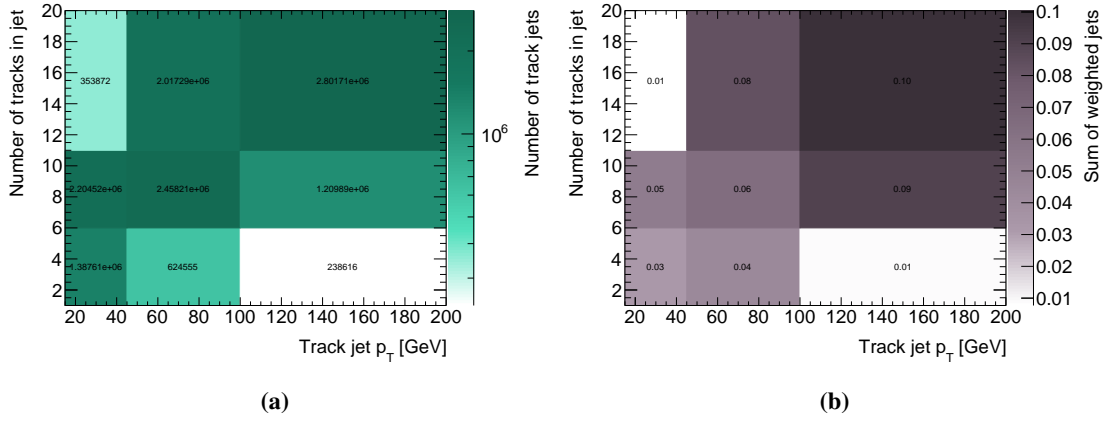


**Figure 7.7:** The number of the track jets passing the jet selections of the **High- $p_T$**  SR (a) before and (b) after applying the track jet-DV probability and  $f$  factor.

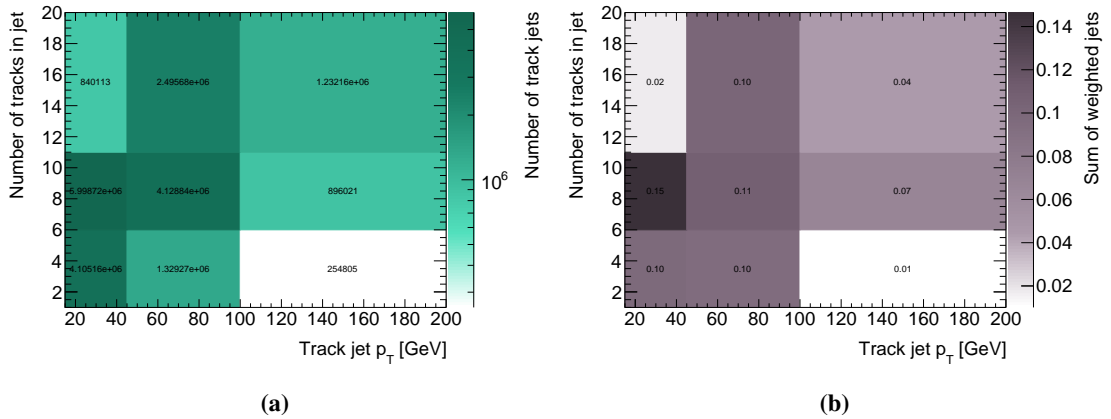


**Figure 7.8:** The number of the track jets passing the jet selections of the **Trackless** SR (a) before and (b) after applying the track jet-DV probability and  $f$  factor.

### 7.3 Uncertainties on background estimation

Three sources of uncertainty are considered for this background estimation. First, the statistical uncertainty on the number of events with a SR-like DV in the CR is propagated to the final estimate. This uncertainty takes into account both of the statistical uncertainty on the track jet-DV probability and on the  $f$  factor. A toy MC method with  $N = 10000$  pseudo-experiments is used to estimate this uncertainty. The number of events with a SR-like DV in the CR shown in Figure 7.6(a) is varied in each bin within its statistical uncertainty, and the calculation of the new track jet-DV probability distribution and  $f$  factor using it and estimation of the number of the background events are repeated  $N$  times. The standard deviation of the estimated number of background events from all statistically varied toy experiments is taken as the uncertainty in the final background estimate. An uncertainty of 58% is added from this statistical uncertainty to the estimated number of background events in both of High- $p_T$  and Trackless SRs.

The second systematic uncertainty takes into account differences in track jet multiplicity between CR and SRs. This estimation method allows the track jet-DV probability to be calculated as a value that also includes differences in track jet multiplicity within events. This allows the track jet-DV probability to be calculated in the CR having events with fewer number of track jets and applied to the events passing the jet selections of the SRs with more number of track jets. The impact of this difference in track jet multiplicity on the track jet-DV probability is tested and added as an uncertainty. The tests are carried out according to the following steps

1. The track jet-DV probability is derived for a SR-like DV as a function of the number of track jets.
2. The distribution of the track jet-DV probability is fitted by a linear function. Figure 7.9(a) shows the distribution with a fit of a liner function.
3. The fitting function is multiplied with the distribution of the number of events in the CR and passing the jet selections of the SRs as a function of the number of track jets shown in Figure 7.9(b), bin by bin. The value at the centre of each bin is used as the value of the fit function.
4. The resulting histograms are integrated over all bins ( $N$ ), and the difference between  $N_{\text{CR}}$  and  $N_{\text{pass jet selections of High-}p_T \text{ SR}}$  ( $N_{\text{pass jet selections of Trackless SR}}$ ) is calculated. The uncertainty is the value of the difference and assigned to the estimated number of background events in the High- $p_T$  SR (Trackless SR).

The procedure is repeated with variations of the fitting function with the anti-correlation parameter varied within  $1\sigma$ , and the largest uncertainty is assigned to the estimated number of background events. An uncertainties of  $^{+10\%}_{-27\%}$  on the estimate of background in the High- $p_T$  SR and  $^{+6.3\%}_{-17\%}$  in the Trackless SR are added from this procedure.

Finally, the third systematic uncertainty to consider the differences in the pileup distributions between the CR and the SRs is assigned. The pileup distribution in these regions is shown in

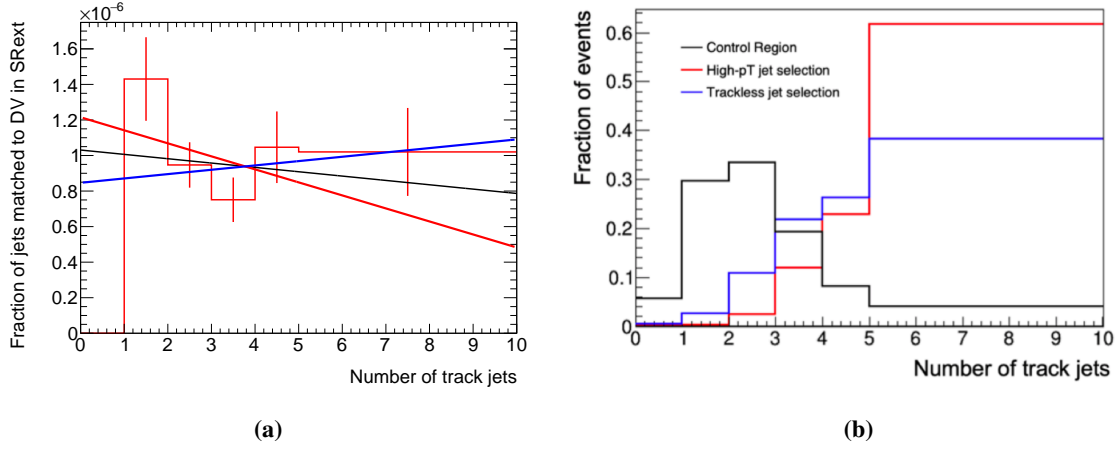


**Figure 7.9:** (a) The track jet-DV probability for a SR-like DV ( $N_{\text{Trk}} > 3$  and  $m_{\text{DV}} > 5$  GeV) as a function of the number of track jets per event. The distribution is fit to a linear function (black line) and the anti-correlated fit parameters are varied within  $1\sigma$  (red and blue lines). (b) The distribution of the number of track jets in the CR and in events passing the jet selections of the SRs using the same binning of the track jet-DV probability. Both of plots are normalized by the integration of the distribution.

Figure 7.10. Events which pass the jet selections of the High- $p_T$  SR have on average lower pileup than the events in the CR, while events passing the jet selections of the Trackless SR have slightly higher pileup. This is because the events are selected so that there is no duplication in each region, in the order of priority: High- $p_T$  SR, Trackless SR, and CR. This trend is found to be consistent in all data-taking years, individually. In order to consider these differences, events in the CR are reweighted so that the pileup distribution matches events passing the jet selection of Trackless or High- $p_T$  SRs. Then, the track jet-DV probability is recalculated with the reweighted events and the estimated number of background events is re-evaluated. In this procedure, the number of expected background events is 0.46 (0.83) in the High- $p_T$  (Trackless) SR, which corresponds to a 5.9% decrease (20% increase) of the number of events in the High- $p_T$  (Trackless) SR. Changes in these values are added as an uncertainty.

All of above uncertainties are assumed to be uncorrelated.

## 7.4 Validation

In this section, several methods to validate the inclusive estimate are presented. These are:

1. Validation in the low multiplicity or low DV mass sideband regions of the SR in data
2. Validation in the high multiplicity, high DV mass, and inside of material regions
3. Cross check with the alternative background estimation method

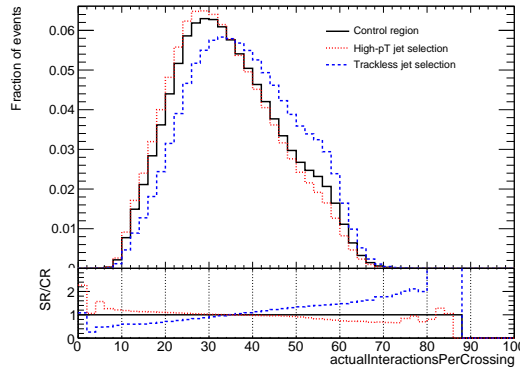


**Figure 7.10:** The pileup distribution in the CR and in events passing the jet selections of the High- $p_T$  and Trackless SRs.

#### 7.4.1 Validation in sideband regions of the SR

First, the inclusive background estimation technique is tested in low multiplicity or low DV mass sideband regions of the High- $p_T$  SR and Trackless SR in data. Events in these sideband regions pass the jet selections and include at least one DV satisfying the baseline DV selections. The track jet-DV probability for each validation region is calculated separately as described in Section 7.2.1.

The validation results in the sideband regions of the High- $p_T$  SR and Trackless SR are shown in Figure 7.11 and Figure 7.12, respectively. There is good agreement between the number of estimated and observed events in most validation regions. The largest deviation occurs in the validation region containing events passing the jet selections of the High- $p_T$  and Trackless SR with a DV satisfying the number of the tracks ( $N_{\text{Trk}} = 4$  and  $2 < m_{\text{DV}} < 5$  GeV).

#### 7.4.2 Validation in the inside material regions

To check whether this estimation method works for high multiplicity and high mass DVs, validation was carried out using DVs in the inside material region. DVs are required to pass the full DV selection except for the material map veto and to fail the material map veto. The track jet-DV probability is calculated for each DV satisfying the requirement of track multiplicity and mass using DVs in the CR which are reconstructed inside of material regions. The validation results inside material regions are shown in Figure 7.13.

In the events passing the jet selection of the High- $p_T$  SR, the number of observed and expected events in the region for high DV mass of  $m_{\text{DV}} > 15$  GeV is almost consistent within error. While, there is a significant underestimation of the number of events for the lower DV mass of  $m_{\text{DV}} < 15$  GeV. This is confirmed for both DVs reconstructed from four tracks (4-trk DVs) five or more tracks ( $>4$ -trk DVs). In the events passing the jet selection of the Trackless SR, the number of observed and expected events is almost consistent within error for all validation regions. There is a mild overestimation of the number of events in the  $m_{\text{DV}} = 5\text{--}10$  GeV mass region for both of 4-trk DVs and  $>4$ -trk DVs.

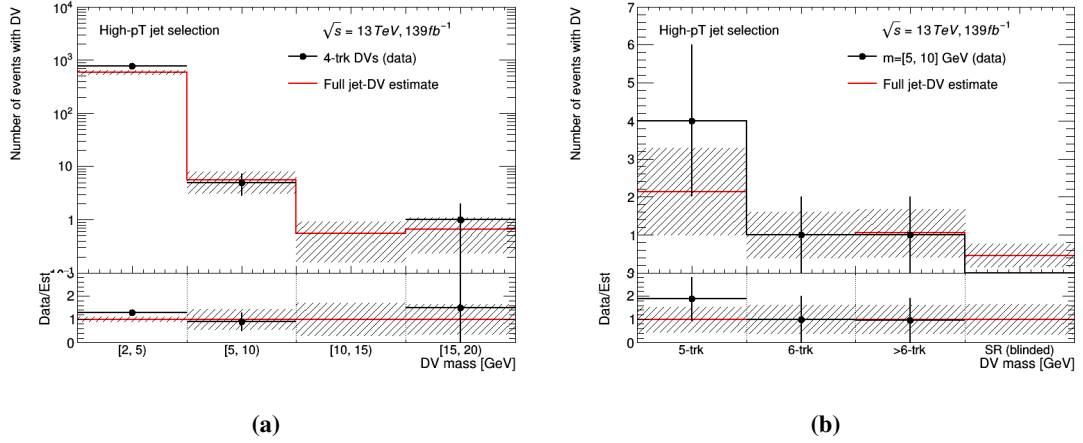


**Figure 7.11:** Validation results in various sideband regions of the **High- $p_T$  SR**. Black dots are observed number of events and red lines are expected number of events. In (a), the regions contain events containing DVs satisfying  $N_{\text{Trk}} = 4$  and various mass requirements. In (b), the regions contain events containing DVs satisfying the various track multiplicity requirements of  $N_{\text{Trk}} > 4$  and  $m_{\text{DV}} = 5\text{--}10 \text{ GeV}$ . The rightmost bin in (b) shows background estimate in the SR ( $N_{\text{Trk}} \geq 5$  and  $m_{\text{DV}} > 10 \text{ GeV}$ ).

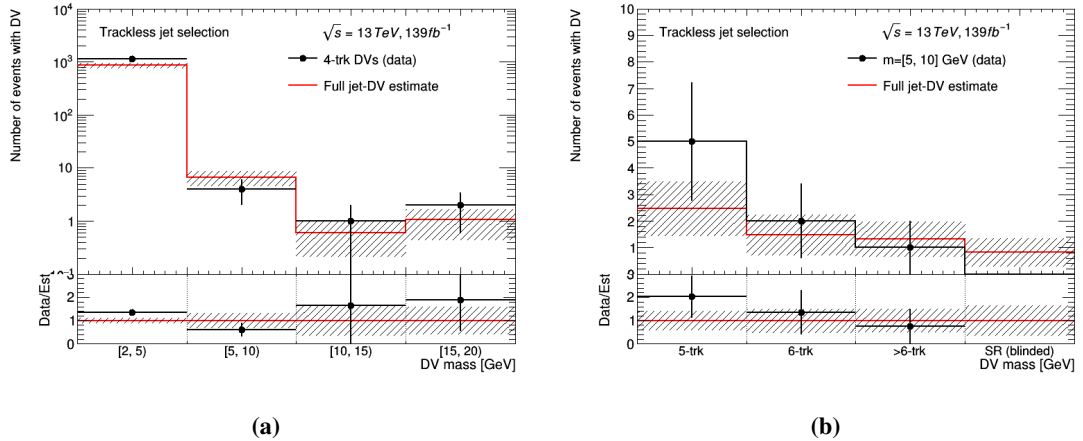


**Figure 7.12:** Validation results in various sideband regions of the **Trackless SR**. Black dots are observed number of events and red lines are expected number of events. In (a), the regions contain events containing DVs satisfying  $N_{\text{Trk}} = 4$  and various mass requirements. In (b), the regions contain events containing DVs satisfying the various track multiplicity requirements of  $N_{\text{Trk}} > 4$  and  $m_{\text{DV}} = 5\text{--}10 \text{ GeV}$ . The rightmost bin in (b) shows background estimate in the SR ( $N_{\text{Trk}} \geq 5$  and  $m_{\text{DV}} > 10 \text{ GeV}$ ).

To understand a significant underestimation in events passing the jet selection of the High- $p_T$  SR, a test was conducted using MC. The validation results in the inside material region using the dijet MC are shown in Figure 7.14. An underestimation of the number of the background events is also observed in the MC for events with a  $>4$ -trk DV with  $m_{\text{DV}} = 5\text{--}10 \text{ GeV}$  in the events passing the jet selections of the High- $p_T$  SR.



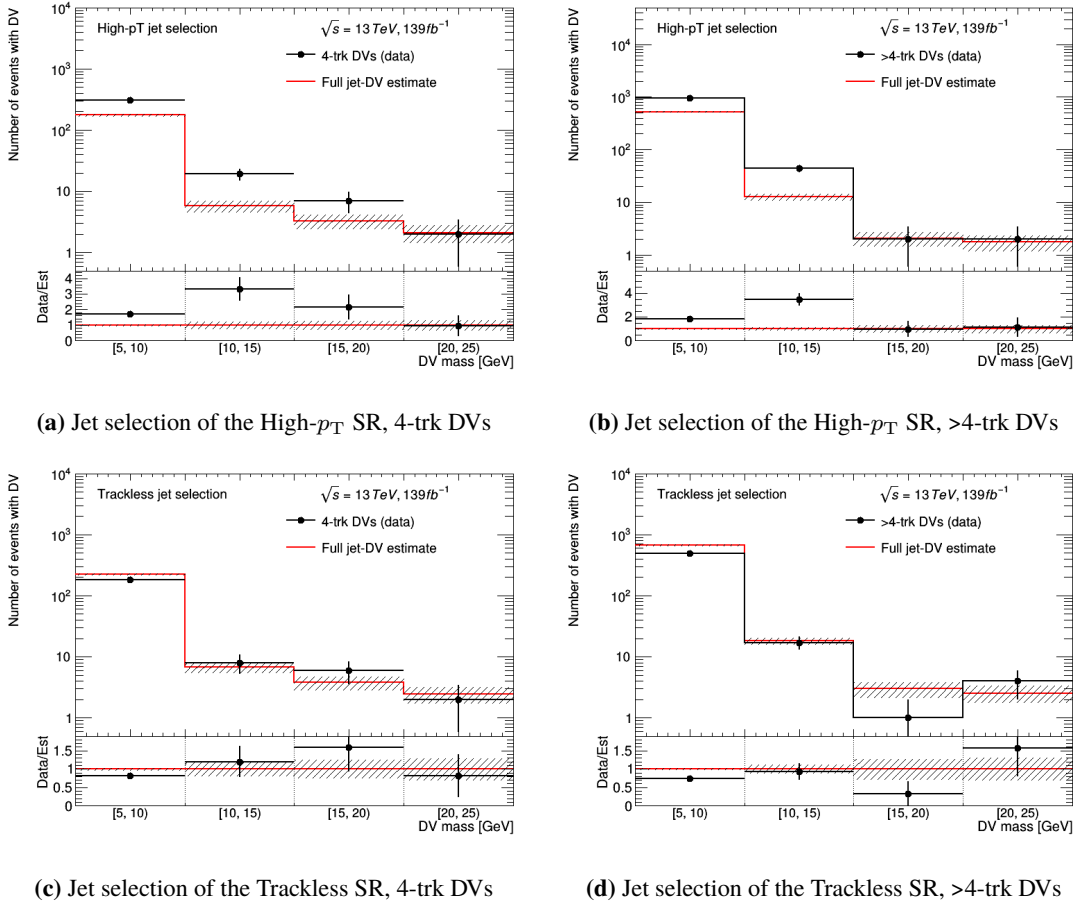


**Figure 7.13:** Validation results in the inside of material regions using **data**. DVs are required to pass the full DV selection except for the material map veto and to fail the material map veto. Black dots are observed number of events and red lines are expected number of events. Only the statistical uncertainties propagated from the CR are drawn in the number of estimated events.

By categorizing the DVs by the type of tracks constructing the DV, which of the three DV sources shown in Figure 7.1 affected the underestimate is considered. The DVs are categorized as follows and use only the DVs for each category to calculate the track jet-DV probabilities and estimate the number of DVs:

- **Hadronic interactions:** All tracks constructing the DV are from hard scattering process and generated in the GEANT4 simulation step and originate from the same SM long-lived parent particle.
- **Accidental crossings:** Includes following two kinds of DVs.
  - All tracks in the DV are from hard scattering process but do not share the same SM long-lived parent particle. There should be two parent particles, one with two or more tracks and one with only one track.
  - The DV is reconstructed from two or more hard scattering tracks and one track derived

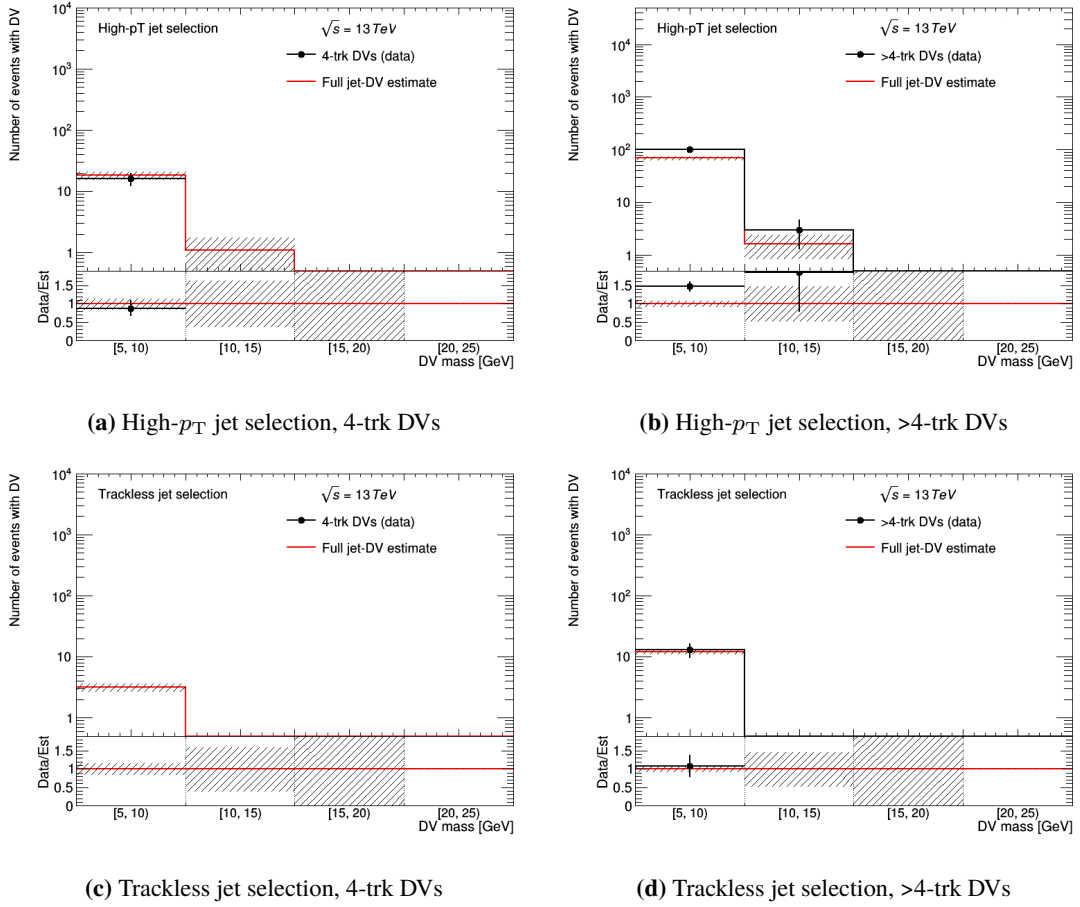


**Figure 7.14:** Validation results in the inside of material regions using **dijet MC**. DVs are required to pass the full DV selection except for the material map veto and to fail the material map veto. Black dots are observed number of events and red lines are expected number of events. Only the statistical uncertainties propagated from the CR are drawn in the number of estimated events..

from a pile up. The hard scattering tracks should be from the same SM long-lived parent particle.

- **Merged vertices:** All tracks in the DV are from hard scattering process but do not share the same SM long-lived parent particle. There should be two parent particles, both with two or more tracks.

The validation results for the low mass DV are shown in Figure 7.15 for events passing the jet selections of the High- $p_T$  SR. It is clear that the DVs from the hadronic interaction is cause of the underestimate of the expected number of events. Therefore, whether this underestimation has a significant impact on the estimate of the number of events in the High- $p_T$  SR is considered by the ratio of hadronic interactions in the High- $p_T$  SR. In the next section, the cross check with the alternative background estimation method, which estimating each DV source independently, and estimate of the ratio of hadronic interactions are described.

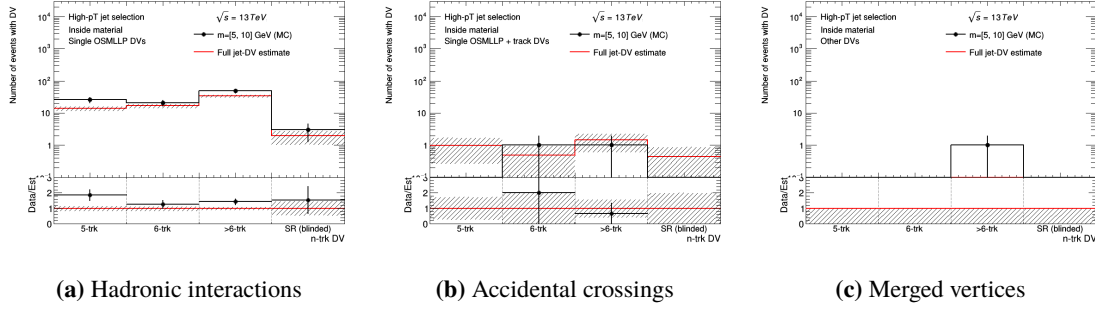


**Figure 7.15:** Validation results in the low-mass and inside of material validation regions for different categories of DVs, for the events passing the jet selections of the High- $p_T$  SR using **dijet MC**. Black dots are observed number of events and red lines are expected number of events. Only the statistical uncertainties propagated from the CR are drawn.

### 7.4.3 Cross check with the independent background estimation method

The cross check of the inclusive background estimation method with an alternative approach that aims to estimate each source of background independently is described. Each DV source is independently estimated by the data-driven techniques and combined into a complete background estimate.

#### Hadronic interactions

The number of DVs derived from hadronic interaction is estimated by extrapolating the mass distribution obtained by fitting the mass distribution of the data in the  $m_{DV} < 10$  GeV region to the signal region for  $m_{DV} > 10$  GeV. This background component includes vertices created by decays of the long-lived SM particles.

The green distribution in Figure 7.16 shows the mass distributions of the DV derived from hadronic interactions in the outside material region. The other color distributions in Figure 7.16 show the mass distributions of the DV derived from other DV source in Figure 7.1. For  $m_{DV} < 10$  GeV, the contamination from other categories of DVs is smaller than the DVs derived from the hadronic interactions. This indicates that fits in the  $m_{DV} < 10$  GeV region can be done with less contamination of other DV components.

The following function was employed to empirically describe the shape of the distribution, which is linearly increasing at low mass and exponentially decaying at high mass, in Figure 7.16:

$$n_{DV}(m) = \frac{1}{\frac{1}{C(m-b)} + \frac{1}{e^{-\frac{m-B}{l}}}}, \quad (7.4)$$

where  $m$  is the DV mass,  $C$  and  $b$  are the slope and intercept of the DV mass in the initial straight line describing the low-mass part, and  $B$  and  $l$  describe the magnitude and slope of the exponential component. This function is floored at 0 to avoid negative values at any values of DV mass. The uncertainties from fitting the distributions are propagated to the mass distribution.

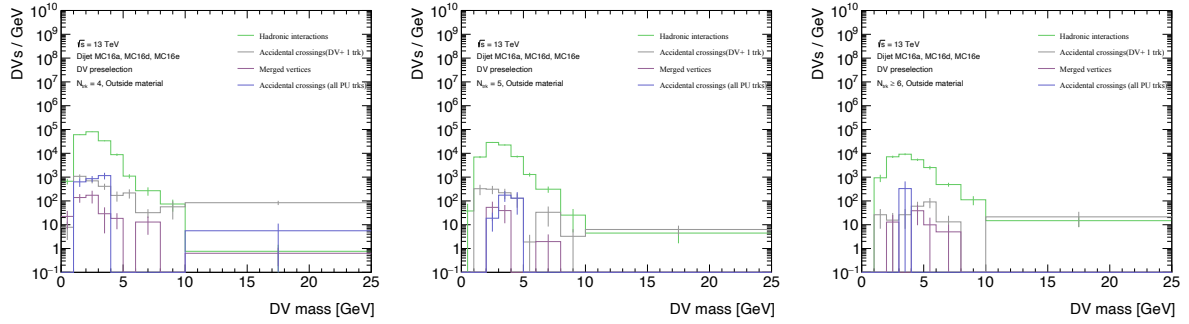


**Figure 7.16:** The mass distributions of DVs derived from various DV categories as a function of DV mass for DVs with 4 tracks (left), 5 tracks (middle) and 6 or more tracks (right) in the outside material region using **dijet MC**. Green distribution is DVs derived from hadronic interactions, the gray and blue distributions are accidental crossings, and the purple distribution is merged vertices.

## Accidental crossings

The number of DVs derived from accidental crossings is estimated by following three steps:

1. producing a database of accidentally crossing tracks.
2. producing mass templates of DVs which contain an accidentally crossing track.
3. measuring the probability that an accidentally crossing track is associated to a DV.

The behavior of the DVs derived from accidental crossings is expected to differ depending on the position of the DV due to the vertex reconstruction efficiency and the crossing angle of the tracks depending on DV position. Therefore, the following procedure is performed separately in different radial regions of the detector:

- Inside beam pipe (BP):  $R_{xy} < 25$  [mm]
- Inside IBL:  $25 \leq R_{xy} < 38$  [mm]
- Inside the most outer layer of the pixel detector (L2):  $38 \leq R_{xy} < 120$  [mm]
- Inside SCT:  $120 \leq R_{xy} < 300$  [mm]

The *track database* is a collection of the track informations which have accidentally crossed to a DV. Accidental crossing tracks are identified using displaced decays of the  $K_S^0$  meson. The invariant mass of  $K_S^0$  is 498 MeV and the average lifetime is 90 ps. To identify the accidental crossing tracks, DVs constructed from three tracks where two tracks can be combined to form a vertex consistent with the  $K_S^0$  mass are identified. Then, the third track of vertices not included in the calculation of  $K_S^0$  mass is considered to be the track which is accidentally crossing the decay vertex of  $K_S^0$ . If this accidental crossing track passes the DV-track selection described in Section 6.4.2, it is added to the track database. The  $p_T$  and  $\eta$  of the accidental crossing tracks,  $R_{xy}$  and  $z$  position of the DV where the accidental crossing track was taken from, the direction between DV and PV, and the crossing angle  $\Delta\phi$  defined as the angle between the accidental crossing track and the direction of the DV from the primary vertex are stored to the track database.

Mass templates are produced separately for each DV track multiplicity. For DVs reconstructed from  $n$  tracks, one track recorded in the *track database* is added at random. At this time, add a track stored in the same  $R_{xy}$ ,  $z$  region as the DV. The boundaries of the  $z$  regions used are -300, -150, -100, -50, 0, 50, 100, 150, 300 mm. All DVs satisfy the baseline DV selections in the event that satisfy the requirements of jet selections of each SR are used to build the template. Calculate the DV mass, including a track added from the *track database*, and define the distribution as the DV mass distribution reconstructed from the  $n+1$  tracks.

The mass distribution up to this point is created assuming that all DVs reconstructed from  $n$  tracks in the data are accidentally crossed by a track. In the final step of the estimate, the mass distributions are scaled down by the *crossing factor*, which is the probability that tracks cross to the DVs accidentally. The *crossing factor* is calculated from the ratio between the number of  $K_S^0$  decay vertices reconstructed from only two pure tracks and the number of  $K_S^0$  in the DV reconstructed from three tracks. Figure 7.17(a) shows the mass distribution of the DVs reconstructed from two tracks for the outermost radial region ( $120 \leq R_{xy} < 300$  [mm]). Figure 7.17(b) shows the mass distribution calculated by selected two of three tracks which constructing DVs, using DVs reconstructed from three tracks. The part fitted by a liner function is subtracted as the background from each histogram and the mass distribution is integrated in the mass range of 0.46–0.54 GeV. Each of these integrals refers to the number of reconstructed  $K_S^0$  decays without and with an accidental crossing track. Therefore the crossing factor is calculated as follow:

$$\begin{aligned}
 a = K_S^0 \text{ with accidental crossings} &= \int_{K_S^0 - 40 \text{ MeV}}^{K_S^0 + 40 \text{ MeV}} N[_3P_2(3\text{-track DV})](m) dm \\
 b = K_S^0 \text{ without accidental crossings} &= \int_{K_S^0 - 40 \text{ MeV}}^{K_S^0 + 40 \text{ MeV}} N[2\text{-track DV}](m) dm \\
 \therefore \text{Crossing factor} &= \frac{a}{a+b}
 \end{aligned} \tag{7.5}$$

where the  $m$  is the invariant mass of the vertex and  $_3P_2$  is the permutation of two tracks in the DV reconstructed from three tracks.

The *crossing factors* in each radial region are shown in Figure 7.18 and listed in Table 7.1. Because there were too few  $K_S^0$  reconstructed in the inside BP and inside IBL regions with accidental crossing tracks, these regions were combined to calculate the crossing factor. The "All AX" *crossing factors* are calculated using all reconstructed  $K_S^0$  with an accidental crossing track, and are used to weight DVs reconstructed from  $n+1$  tracks in the mass distribution when the DVs reconstructed from  $n$  tracks have at least 2 selected tracks. The "Selected AX" *crossing factors* are calculated using only reconstructed  $K_S^0$  which the accidental crossing tracks are used to construct the first vertex seed, and are used to weight DVs reconstructed from  $n+1$  tracks in the mass distribution when the DVs reconstructed from  $n$  tracks have only 1 selected track. As the radial position of the DV increases, the *crossing factor*

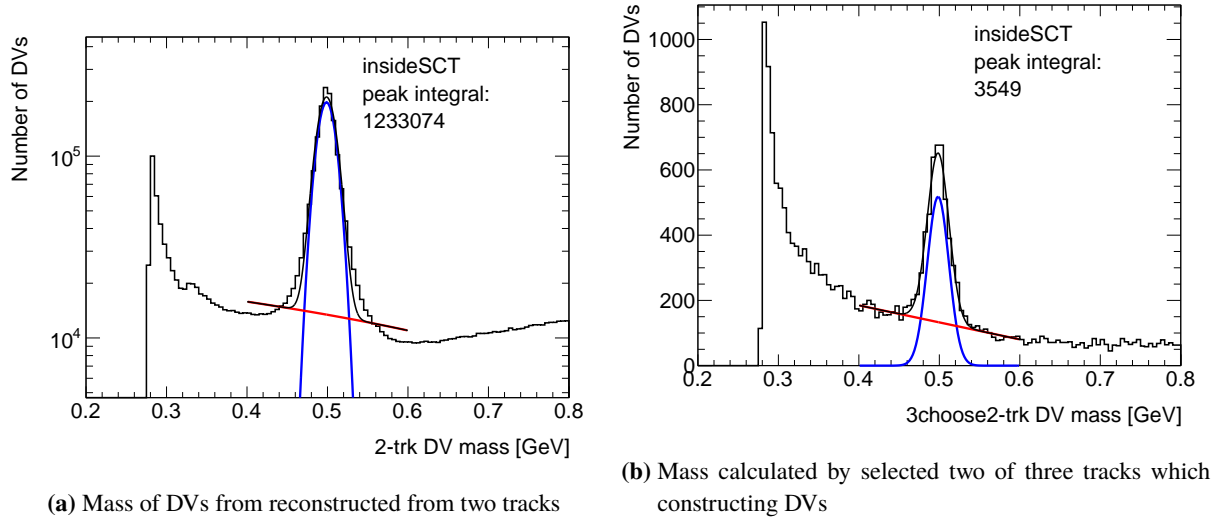


**Figure 7.17:** The mass distributions of (a) DVs reconstructed from 2 tracks and (b) mass calculated by selected two of three tracks which constructing DVs, using data in the inside SCT region. Note that y-axis in (a) is logarithmic, while the y-axis in (b) is linear. The mass distributions are fit by a Gaussian (blue) and a linear (red) functions. The total number of entries in the peak after subtracting the fitted by a linear function is printed on each histogram.

increases. This is due to the lower resolution of the vertex positions after the last pixel layer.

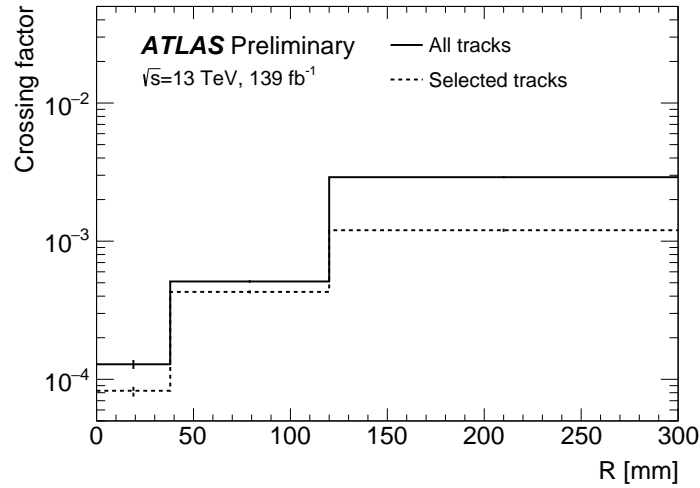


**Figure 7.18:** Crossing factors calculated in each radial region. The error bars show the statistical uncertainties.

The mass distribution of DVs reconstructed from (3+1) tracks, (4+1) tracks, and ( $\geq 5+1$ ) tracks, scaled by these *crossing factors* and combined each radius regions are shown in Figure 7.19. The number of the DVs derived from accidental crossings in the SR is calculated by integrating these templates in the  $m > 10$  GeV region.

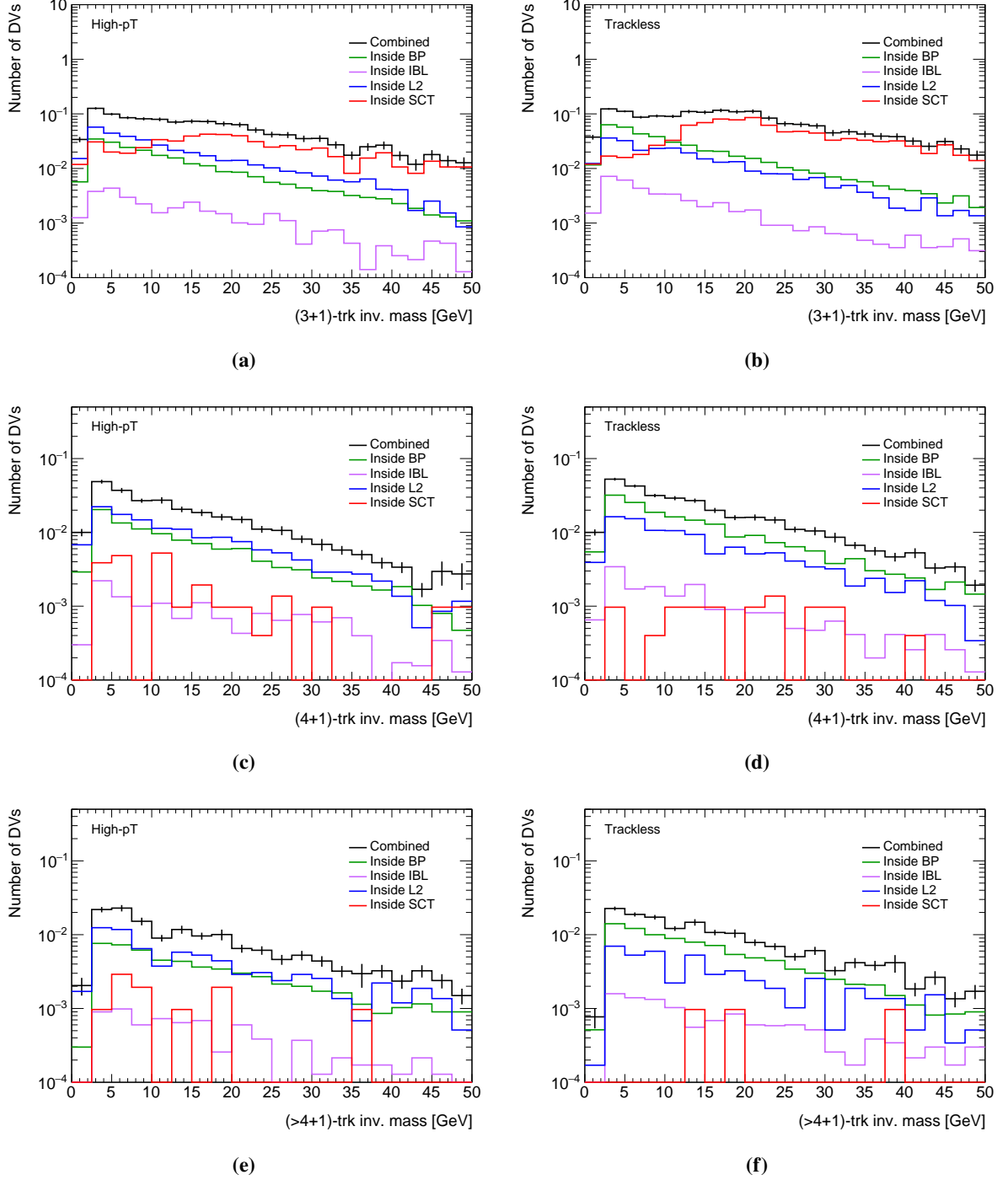


**Figure 7.19:** Final mass distributions of accidental crossings for the various DV track multiplicities in both SRs, as indicated in the legend of each plot. Each distribution is scaled by the appropriate crossing factor. Only statistical uncertainties are drawn on the combined distribution.

**Table 7.1:** Crossing factors including the statistical uncertainties calculated in each radial region. The same crossing factor is used for the inside BP and inside IBL regions.

Radial region	Crossing Factors	
	All AX	Selected AX
Inside BP	$(1.284 \pm 0.095) \times 10^{-4}$	$(8.26 \pm 0.76) \times 10^{-5}$
Inside IBL	$(1.284 \pm 0.095) \times 10^{-4}$	$(8.26 \pm 0.76) \times 10^{-5}$
Inside L2	$(5.11 \pm 0.12) \times 10^{-4}$	$(4.29 \pm 0.11) \times 10^{-4}$
Inside SCT	$(2.910 \pm 0.049) \times 10^{-3}$	$(1.201 \pm 0.031) \times 10^{-3}$

## Merged vertices

Mass templates of merged vertices with varying track multiplicities are built by randomly merging pairs of DVs taken from different events in data. Only DVs with a distance significance of  $S < 10$  are merged.  $S$  is the distance between vertices divided by its uncertainty defined as

$$S = \sqrt{(\vec{v}_1 - \vec{v}_2)(C_1 + C_2)^{-1}(\vec{v}_1 - \vec{v}_2)^T}, \quad (7.6)$$

where  $\vec{v}_1$  and  $\vec{v}_2$  are three-dimensional positions of DVs and the quantities  $C_1$  and  $C_2$  are the covariance matrices of the DVs.

The number of background events including DVs derived from the merged vertices is estimated by comparing the distributions of the distance significance  $S(V_1, V_2)$  for DV pairs taken from the same events and different events. Specifically, the number of events is estimated by the following procedure:

1. The ratio of vertices merged is called "merging rate" and calculated from the ratio of the distribution of distance significance between DV pairs taken from the same and different events.
2. The mass distribution of DVs derived from merged vertices is created by merging the DV pairs taken from different events which satisfy  $S < 10$ . The mass of the merged DV pair is calculated using the all tracks constructing both of DVs.
3. The mass distribution is normalized by the merging rate. The same weight is assigned to each merged DV mass in the distribution so that the integral of the distribution matches the integral of the difference between the distribution of distance significance created using the same events and the different events.
4. DV-track selection described in Section 6.4.2 is performed on the merged DVs in the mass distribution, and the mass is recalculated using only for tracks that satisfy the requirements.
5. The number of vertices in the SR is calculated by integrating the mass distributions in the  $m_{\text{DV}} > 10$  GeV region.



The above steps are performed separately for DV with each track multiplicity.

The distribution of the distance significance of the DV pairs reconstructed from two and three tracks is shown in Figure 7.20 for events which pass the jet selections of the Trackless SR. The distribution of the distance significance in the different event is normalized to match the distribution in the same events in the  $S > 10$  region, where merging is forbidden. In the  $S < 10$  region, the number of DV pairs in the same events is less than that in the different events. It indicates that merging has taken place in the same events. The difference in this distribution is the merging rate.

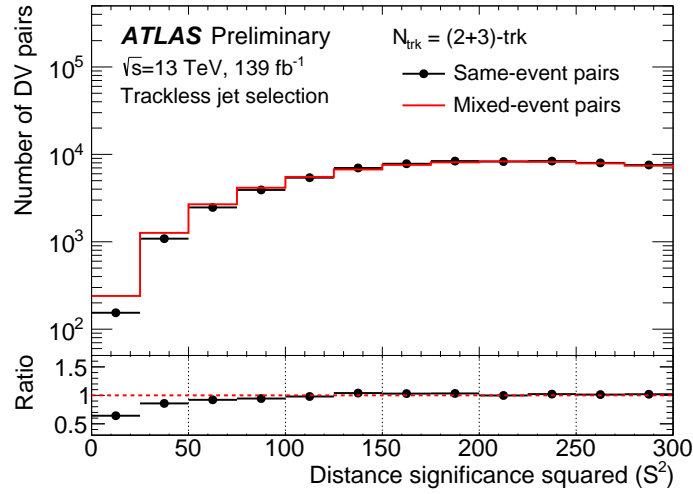


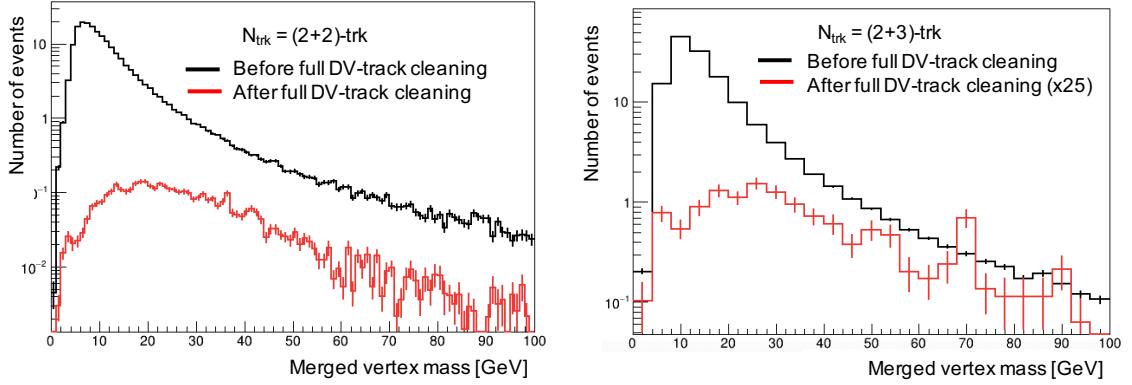
**Figure 7.20:** The distribution of the distance significance of the DV pairs reconstructed from two and three tracks in the same (black) events and different (red) events for events which pass the jet selections of the Trackless SR. The distribution in the different events is normalized to match the distribution in the same events in the  $S > 10$  region.

The mass distribution of the merged DVs is calculated using tracks constructing merged DVs which satisfy  $S < 10$ . The black lines in Figure 7.21 show the mass distributions normalized by the merging rate for merged DVs reconstructed from four and five tracks in events passing the jet selections of the High- $p_T$  SR. The red lines in Figure 7.21 show the mass distributions after applying the DV-track selections and recalculating the DV mass and multiplicity. Finally, the number of the DVs derived from merged vertices is estimated by integrating the red mass distributions of DVs reconstructed from five or more tracks in the  $m_{DV} > 10$  GeV region.

The statistical uncertainty of the number of DV pairs with  $S < 10$  in the same and different events is propagated to the final estimate of number of merged vertices. This uncertainty is 30–50% and 7–13% in the High- $p_T$  and Trackless SR, respectively.

## Combined background

The mass distributions of each background source described above are combined. The uncertainties on each component are assumed to be uncorrelated and are added in quadrature to produce the final uncertainty on the combined estimate. Figure 7.22 shows the expected and observed event for the



(a) The mass of merged DVs reconstructed from two and two tracks. (b) The mass of merged DVs reconstructed from two and three tracks.

**Figure 7.21:** The mass distribution of merged DVs before (black) and after (red) the DV-track selections is applied, for (a) 4-track and (b) 5-track DVs in events passing the jet selections of the High- $p_T$  SR.

DVs reconstructed from 4 tracks. Good agreement is observed across the entire mass range.

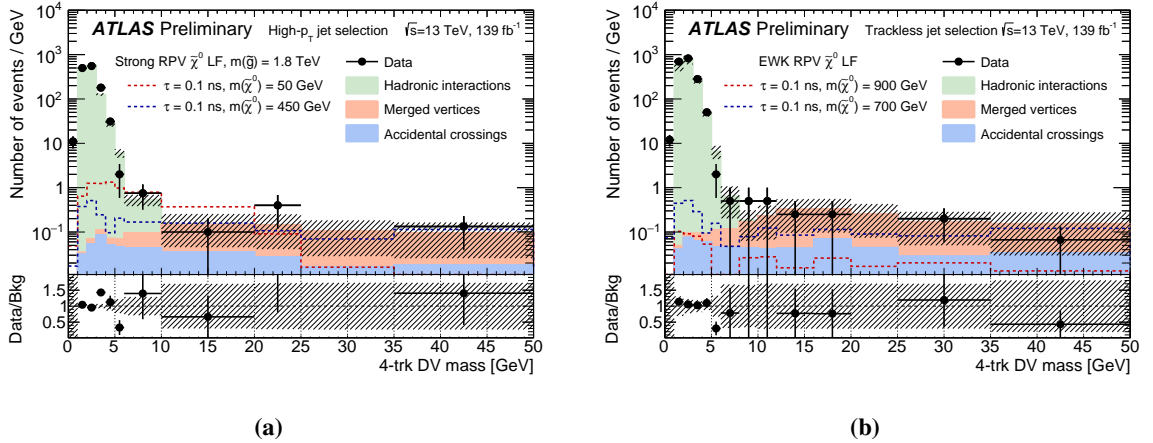


**Figure 7.22:** The expected and observed number of DVs reconstructed from four tracks in events passing the jet selections of (a) High- $p_T$  SR and (b) Trackless SR. The overflow is included in the rightmost bin.

The total expected number of background events in the SRs is shown in Table 7.2. These estimates are consistent within uncertainties with inclusive estimates described in Table 7.3. In this analysis, the inclusive estimation method is used as the primary method because the inclusive estimation method has a smaller uncertainty than the uncertainty of the independent estimation method and is validated in the validation regions that include DVs with a large number of tracks.

#### 7.4.4 Additional systematic uncertainties from the validation results

As the result of the validation in Section 7.4.2, the inconsistency in the number of observed and expected events was observed in the validation region of the inside of material region for the High-

**Table 7.2:** The number of background events in the SRs estimated independently. The uncertainties on the total background estimate are calculated assuming to be uncorrelated between the each estimate.

Region	Merged vertices	Hadronic interactions	Accidental crossings	Combined
High- $p_T$ SR	$0.79 \pm 0.66$	$0.006 \pm 0.018$	$0.28 \pm 0.21$	$1.08 \pm 0.69$
Trackless SR	$1.5 \pm 1.1$	$0.248 \pm 0.077$	$0.32 \pm 0.24$	$2.1 \pm 1.1$

$p_T$  SR. It is understood by the study using MC that this is caused by DVs derived from hadronic interactions. From the results using the independent background estimation method described in Section 7.4.3, the contribution of DVs derived from hadronic interactions is very small in the SR. Therefore, the inconsistency observed in Section 7.4.2 does not adversely affect the number of estimated events in the SR, and it is scaled by the proportion of events attributable to hadronic interactions in the SR and added as the additional systematic uncertainty to the number of predicted events.

In the High- $p_T$  SR, the largest inconsistency is observed for DVs reconstructed from four tracks with mass of 10–15 GeV inside of material as shown in Figure 7.13. In this validation region, the number of background events is underestimated by  $\approx 300\%$ . The fraction of the background from hadronic interactions in the total background in the High- $p_T$  SR is estimated to be  $\approx 0.13\%$  as shown in Table 7.2. When varying the number of estimated events derived from the hadronic interactions and total number of background estimated events within their systematic uncertainties, the maximum fraction of the hadronic Interactions is  $\approx 0.54\%$ . This fraction is rounded up to 1% to produce a conservative uncertainty. Therefore, the additional uncertainty of  $300 \times 0.01 = \pm 3\%$  is assigned to the number of estimated background events in the High- $p_T$  SR.

The final estimated number of background events in the SRs with uncertainties is listed in Table 7.3.

**Table 7.3:** Estimated number of background events in the SR with systematic uncertainties. The "CR statistical" uncertainty refers to the propagation of the statistical uncertainty in the CR to the estimate. The "Non-linearity" uncertainty refers to the impact of the difference in the number of the track jets between the events in the CR and SRs on the track jet-DV probability. The "Pileup" uncertainty is calculated by reweighting events in the CR to match the pileup distribution of events in the SR. "Inconsistent in the VR" uncertainty is additional uncertainty from the validation results. All of uncertainties are assumed to be uncorrelated.

Signal Region	Estimated	Estimate uncertainty				Total
		CR statistical	Non-linearity	Pileup	Inconsistent in the VR	
High- $p_T$ SR	$0.46^{+0.27}_{-0.30}$	$\pm 58\%$	$^{+10\%}_{-27\%}$	$\pm 5.9\%$	$\pm 4\%$	$^{+59\%}_{-64\%}$
Trackless SR	$0.83^{+0.51}_{-0.53}$	$\pm 58\%$	$^{+6.3\%}_{-17\%}$	$\pm 20\%$	-	$^{+62\%}_{-64\%}$

## Chapter 8

# Uncertainties

The systematic uncertainties for the expected number of background events are described in Section 7.3 and 7.4.4. In this chapter, the uncertainties for signal models are described.

The expected number of signal events satisfying the requirements of the signal regions is affected by several sources. First, the uncertainty caused by the difference between data and MC in track and vertex reconstruction efficiency is taken into account. This difference occurs because the MC does not fully reproduce the reconstruction efficiency of the data. This uncertainty is propagated to the vertex selection efficiency, and the estimated number of signal events in the signal region may differ between in MC and data.

Second, the uncertainties from the jet reconstruction and calibration affect the signal selection efficiency, especially, the selection efficiency for the jet selections. To estimate this effects, the jet  $p_T$  is varied within the range of uncertainties of the jet reconstruction and calibration and the changes in signal selection efficiency are considered.

Third, changes in the pile-up may result in changes in the number of DVs, and the signal selection efficiency may be changed. To estimate this effects, signal samples has been reweighted to match the number of interactions per bunch crossing distribution observed in data, and the differences of the selection efficiency between weighted and not weighted samples are assigned as the systematic uncertainty.

Finally, the parameters which are used to create MC samples have uncertainties, and their effects can change the number of signal events. Based on their uncertainty, the signal events were reweighted and their impact on signal selection efficiency was estimated.

### 8.1 Uncertainties from the track reconstruction efficiencies

In this section, the systematic uncertainty from the track reconstruction efficiency is quantified. This uncertainty is taken into account in the following steps:

1. Calculate the difference of the DV reconstruction efficiency between data and MC. From this difference, calculate the probability which tracks or DVs is not reconstructed in data.
2. Based on this probability, remove the track or DV from the signal event in MC and recalculate the signal selection efficiency. The difference in signal selection efficiency before and after

removing the track is added as a systematic uncertainty.

### 8.1.1 Calculation of the probability not to reconstruct tracks or DVs in data

The difference of the track reconstruction efficiency for the standard tracking is determined to be 1.7% [87]. The difference of the track reconstruction efficiency for the large radius tracking have not been studied well and is estimated by comparing the number of reconstructed  $K_S^0$  between data and MC.

Events are required to pass the jet selection of the High- $p_T$  SR described in Section 6.3. The candidates of  $K_S^0$  are required to pass the baseline DV selection described in Section 6.4.1, have exactly two tracks and they satisfy  $\cos(\Delta\phi) > 0.9999$ , and have a mass within 50 MeV of the  $K_S^0$  mass. Tracks derived from  $K_S^0$  which decay before the innermost pixel detector ( $R_{xy} < 22$  mm) are typically reconstructed by standard tracking. Since the difference in reconstruction efficiency of standard tracking is well understood, the number of  $K_S^0$  in MC is normalized to data in this region, and the difference in the region of  $R_{xy} > 22$  mm is determined to be the difference in reconstruction efficiency of LRT.

The number of  $K_S^0$  as a function of radial decay position is shown in Figure 8.1(a). For each radial region being binned, the mass distributions of  $K_S^0$  candidates reconstructed from two tracks are created and fitted, and the flat background distribution is subtracted, and the integrated number in the mass range of  $0.46 < m < 0.54$  as in Figure 7.17 is plotted as the number of  $K_S^0$ . There is good agreement between MC and data in the region of  $R_{xy} < 50$  mm, while the number of  $K_S^0$  is overestimated in MC from ones in data in the region of  $R_{xy} > 50$  mm. This indicates that there is inefficiency in the track or DV reconstruction that is not taken into account in MC.

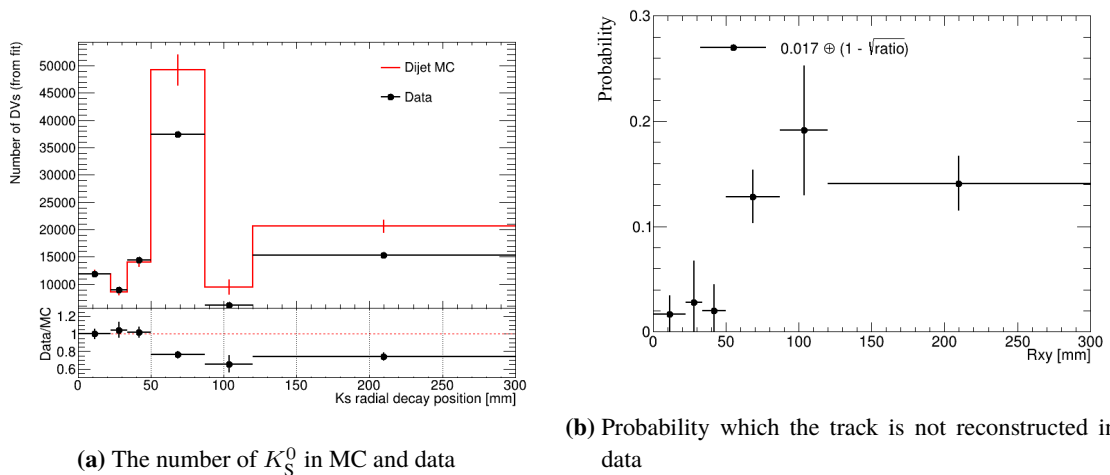


**Figure 8.1:** (a) The number of  $K_S^0$  in different radial regions is compared between data and MC. The MC is normalized to match the data in the innermost radial region (first bin). (b) The probability which the track is not reconstructed in data.

If the case where charged particles interact with the material or undergo large multiple scattering

is not taken into account in MC, the difference in the number of  $K_S^0$  is because some tracks fail to reconstruct due to these in data. This is the inefficiency that occurs independently for each track derived from the  $K_S^0$  decay. This is called an "uncorrelated case". In this case, the probability which the track is not reconstructed in data is calculated as the deviation from 1 of the "Data/MC" ratio in Figure 8.1(a), and adding the 1.7% uncertainty of the standard tracking conservatively. The probability is shown in Figure 8.1(b).

If the decay occurs near disabled modules, some of the tracks constructing the decay vertex may not be reconstructed. This is called a "correlated case". This has little effect on the standard tracking. On the other hand, since the large radius tracking uses a small number of silicon hits, the loss of one hit due to disabled modules has a significant impact on reconstruction efficiency. In this case, assuming that many of the tracks derived from one DV cannot be reconstructed, DVs are removed from the event, using the "data/MC" ratio of the number of reconstructions of  $K_S^0$  in Figure 8.1(a) as the probability which the DV is not reconstructed.

From here, whether to treat the case as a "uncorrelated case" or an "correlated case" is discussed. If this is a "correlated case", the difference in the number of reconstructed Ks is expected to be biased in some  $\eta$ ,  $\phi$  regions. Also, if modules become disabled or has problems during the data taking period, a decrease in the number of Ks should be observed in certain periods. Figure 8.2 shows the ratio of the number of  $K_S^0$  reconstructed in  $R_{xy} > 50$  mm between data and MC in different  $\eta$ - $\phi$  regions. There is no trends which have larger differences in some eta and phi regions clearly. Figure 8.3 shows the number of reconstructed  $K_S^0$  in data collected in early, middle, and late 2017. There is no change in the number of reconstructed  $K_S^0$  over time. Based on the above results, there is no clear evidence which the cause of the difference of the number of Ks in data and MC is due to the "correlated case," and the "uncorrelated case" is considered as the cause of the difference.

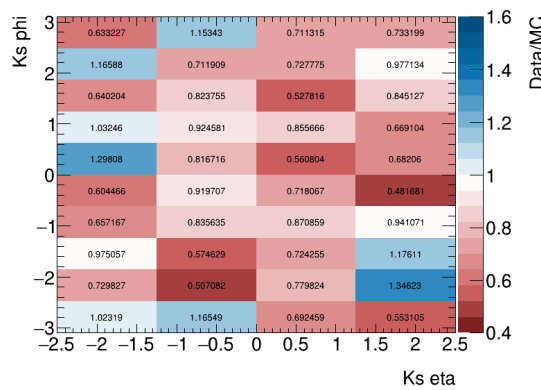


**Figure 8.2:** The data/MC ratio of the number of  $K_S^0$  reconstructed in  $R_{xy} > 50$  mm in different  $\eta$ - $\phi$  regions.

### 8.1.2 Propagation to the systematic uncertainty of the signal efficiency

The probability which tracks are not reconstructed in data is propagated to the signal selection efficiency. Based on the probabilities in Figure 8.1(b), tracks are removed randomly from the DVs

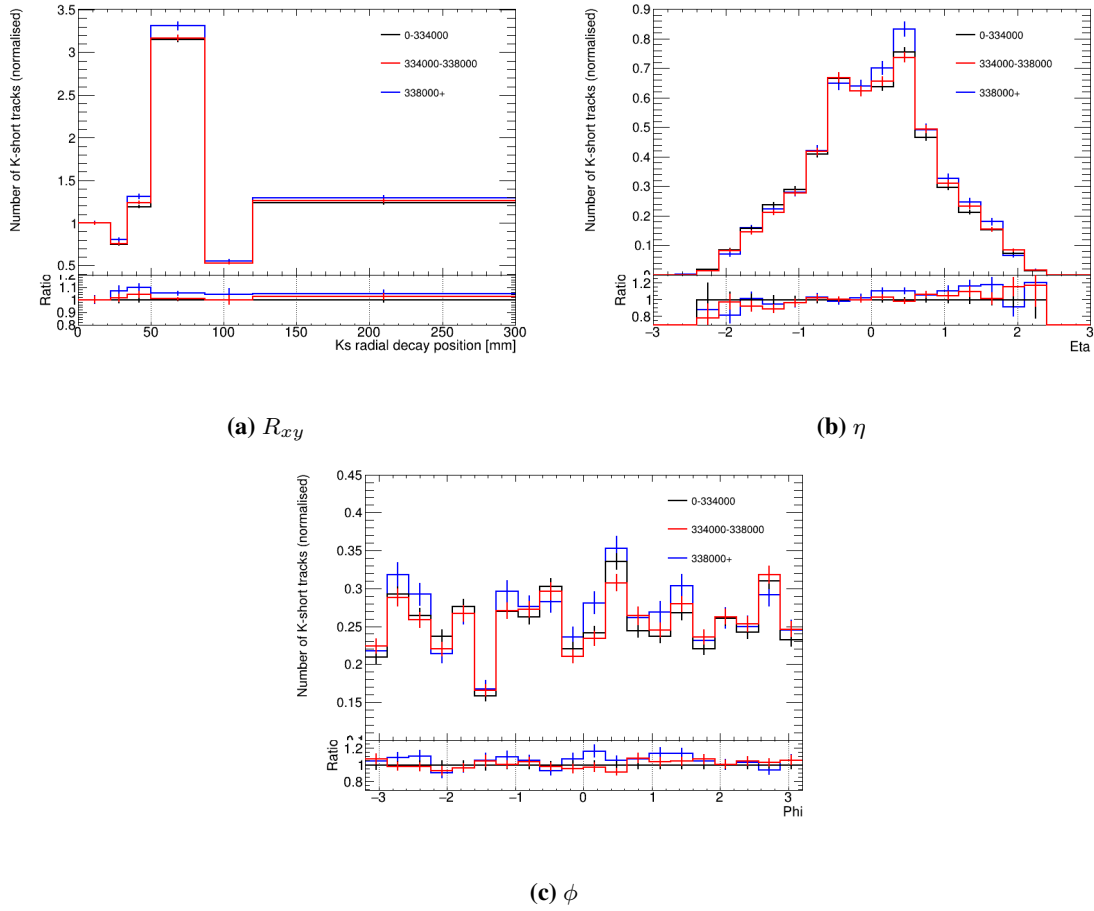


**Figure 8.3:** The comparison of the number of reconstructed  $K_S^0$  in early (black), middle (red) and late (blue) 2017 data as a function of the (a)  $R_{xy}$ , (b)  $\eta$  and (c)  $\phi$  of the reconstructed  $K_S^0$  decay position.

and the changes in signal selection efficiency are calculated.

The signal selection efficiency that satisfy the requirements of either High- $p_T$  or Trackless SR with and without track removal is compared, and the differences are added as a systematic uncertainty for the estimated number of signal events. Figure 8.4 shows the uncertainties propagated to the gluino pair production models and electrowikino pair production models. The uncertainty on the signal efficiency is up to 17% for signals with lower mass and long lifetime neutralinos, while the uncertainty is lower for signals with higher mass neutralinos. This is because the higher mass neutralinos are more likely to be reconstructed with higher track multiplicities, and DVs are not removed from the SRs by removing one track.

## 8.2 Jet uncertainties

The uncertainties of jet energy scale and resolution affect the jet selection efficiency. First, these effects are considered as a systematic uncertainty. In addition, the jets are derived from the long-lived neutralino, and they may not occur near the interaction point. Then, the jet  $p_T$  response ( $= p_T^{\text{reco}} / p_T^{\text{truth}}$ )

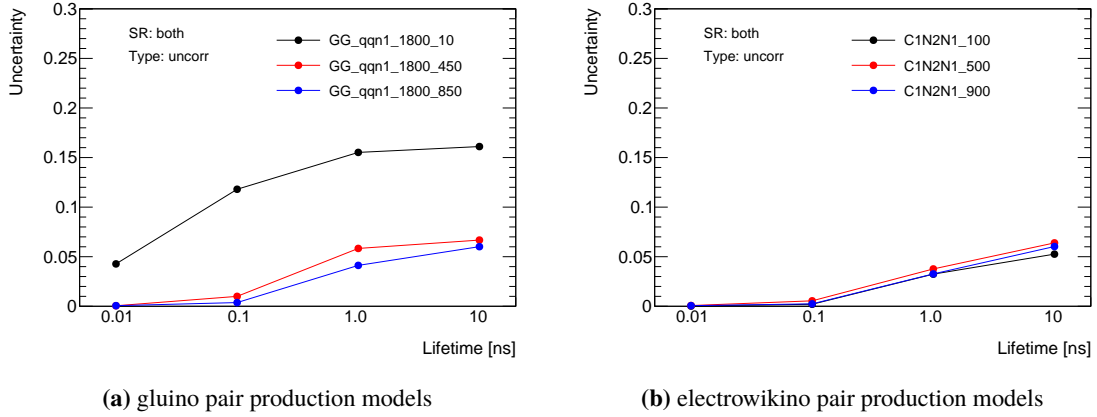


**Figure 8.4:** The uncertainty on the signal efficiency of (a) gluino pair production models with the several neutralino mass and lifetime and fixed gluino mass of 1800 GeV, and (b) electrowikino pair production models with the several neutralino mass and lifetime.

as a function of the jet location is studied to assess if additional uncertainties should be added due to the displacement of the jets.

### 8.2.1 Uncertainties due to the jet energy scale and resolution uncertainties

The uncertainties on the jet energy resolution and jet calibration are described in Figure 5.5 and Figure 5.8, respectively. The jet  $p_T$  is varied within the range of uncertainties of jet energy scale and resolution (JES and JER) uncertainties, and the change in jet selection efficiency is considered.

Table 8.1 shows the uncertainties from the jet energy scale and resolution uncertainties for the gluino pair production models of various gluino mass, neutralino mass, and neutralino lifetime, together with the statistical uncertainty. The uncertainties are only evaluated for the High- $p_T$  SR because Trackless SR doesn't focus on this model.

Figures 8.5 and 8.6 show the uncertainties from the jet energy scale and resolution uncertainties for the electrowikino pair production models, together with the statistical uncertainty for High- $p_T$  and Trackless SR, respectively. The uncertainties due to the jet energy scale and resolution uncertainties are small compared to the uncertainty due to MC statistics in most samples.

### 8.2.2 Jet response due to displacement

The jet energy scale and resolution uncertainty described in Section 8.2.1 have been studied using only jets occurring near the interaction point. Therefore, the jet  $p_T$  response ( $= p_T^{\text{reco}}/p_T^{\text{truth}}$ , corresponding to  $R$  in Eq. (5.3)) in the signal models is studied to investigate the effect of displaced jets on the jet  $p_T$  response.

The gluino pair production models are used in this study. The jet response is calculated using the reconstructed jets after calibration and truth jets. Truth jets are reconstructed using an anti- $k_t$  algorithm of radius  $R = 0.4$  from all stable particles, excluding neutrinos and muons. Only truth



**Table 8.1:** The uncertainties for signal selection efficiency due to jet energy scale and resolution uncertainties (JES and JER) for the gluino pair production model, together with the selection efficiency (Eff.) and the statistical uncertainty (Stat).

$m(\tilde{g})[\text{GeV}]/m(\tilde{\chi}_1^0)[\text{GeV}]/\tau[\text{ns}]$	Eff. [%]	Stat [%]	JES [%]	JER [%]
1600/50/0.01	33.45	1.73	0.37	0.17
1600/50/0.1	15.41	2.55	0.62	0.14
1600/50/1.0	2.05	6.99	0.68	0.68
1600/50/10.0	0.18	23.57	0.00	0.00
1600/1550/0.01	10.33	3.12	0.69	0.64
1600/1550/0.1	69.59	1.20	0.51	0.32
1600/1550/1.0	44.51	1.50	0.46	0.13
1600/1550/10.0	7.21	3.72	0.70	0.73
2000/50/0.01	31.24	1.79	0.40	0.49
2000/50/0.1	13.26	2.75	0.48	0.53
2000/50/1.0	1.78	7.50	1.77	0.00
2000/50/10.0	0.18	24.48	0.00	0.00
2000/850/0.01	27.57	1.90	0.05	0.00
2000/850/0.1	78.04	1.13	0.04	0.00
2000/850/1.0	39.26	1.60	0.00	0.00
2000/850/10.0	5.86	4.14	0.24	0.34
2000/1250/0.01	15.55	2.54	0.00	0.00
2000/1250/0.1	76.27	1.15	0.06	0.06
2000/1250/1.0	45.82	1.48	0.09	0.08
2000/1250/10.0	7.75	3.59	0.59	0.32
2000/1950/0.01	9.17	3.31	0.33	0.22
2000/1950/0.1	73.26	1.17	0.15	0.04
2000/1950/1.0	48.91	1.43	0.24	0.10
2000/1950/10.0	8.23	3.48	0.73	1.00
2600/50/0.01	26.56	1.94	0.16	0.04
2600/50/0.1	10.54	3.08	0.44	0.19
2600/50/1.0	1.28	8.84	0.00	0.00
2600/50/10.0	0.18	30.15	0.00	0.00
2600/1650/0.01	13.03	2.78	0.00	0.00
2600/1650/0.1	77.78	1.13	0.01	0.00
2600/1650/1.0	49.59	1.42	0.03	0.00
2600/1650/10.0	9.07	3.32	0.00	0.00
2600/2550/0.01	6.71	3.87	0.00	0.00
2600/2550/0.1	72.43	1.18	0.11	0.09
2600/2550/1.0	53.07	1.37	0.15	0.07
2600/2550/10.0	10.45	3.09	0.56	0.91

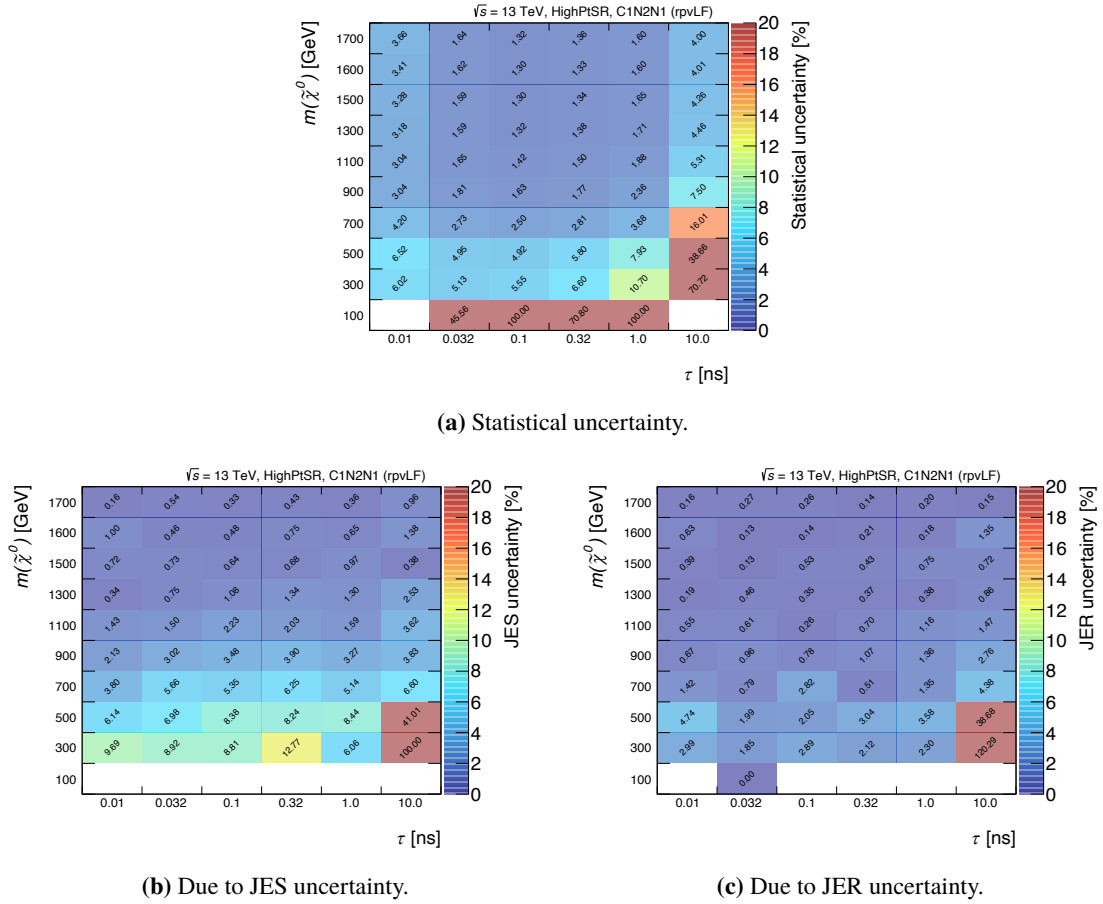


**Figure 8.5:** Uncertainties for the electrowino pair production models in the High- $p_T$  SR.

jets matched with the neutralino decay position, far from the primary vertex at least 1 mm, within  $|\Delta R| < 0.4$  are used. In order to study the dependence of the jet response on the decay topology, the signal simulation samples are divided into two types according to the mass region of the gluinos and neutralinos and studied. The first type considers the regions of small mass difference between the gluinos and neutralinos, which is the neutralino mass of 1250–2550 GeV and the mass difference with the gluinos of 50–350 GeV. In this case, the neutralino is expected to be less boosted, and the decay products are expected to be more likely to emerge in a different direction to the vector direction of the neutralino, which may result in different behaviour from the standard jet. The second type considers the regions of large mass difference and small neutralino mass, which is the neutralino mass of 10–50 GeV and the mass difference with the gluinos of 1590–2550 GeV. In this case, the effect of the difference in the direction between the neutralinos and jets is smaller because the direction between the neutralinos and jets should be more collinear. Also, since the jet  $p_T$  decreases with the mass of the neutralino, it is possible to verify regions of small jet  $p_T$  with large jet energy scale and resolution uncertainty. Lifetimes of 0.01, 0.1, 1, 10 ns are included in both types.

Figure 8.7 and 8.8 show the jet  $p_T$  response as a function of the matched neutralino decay position

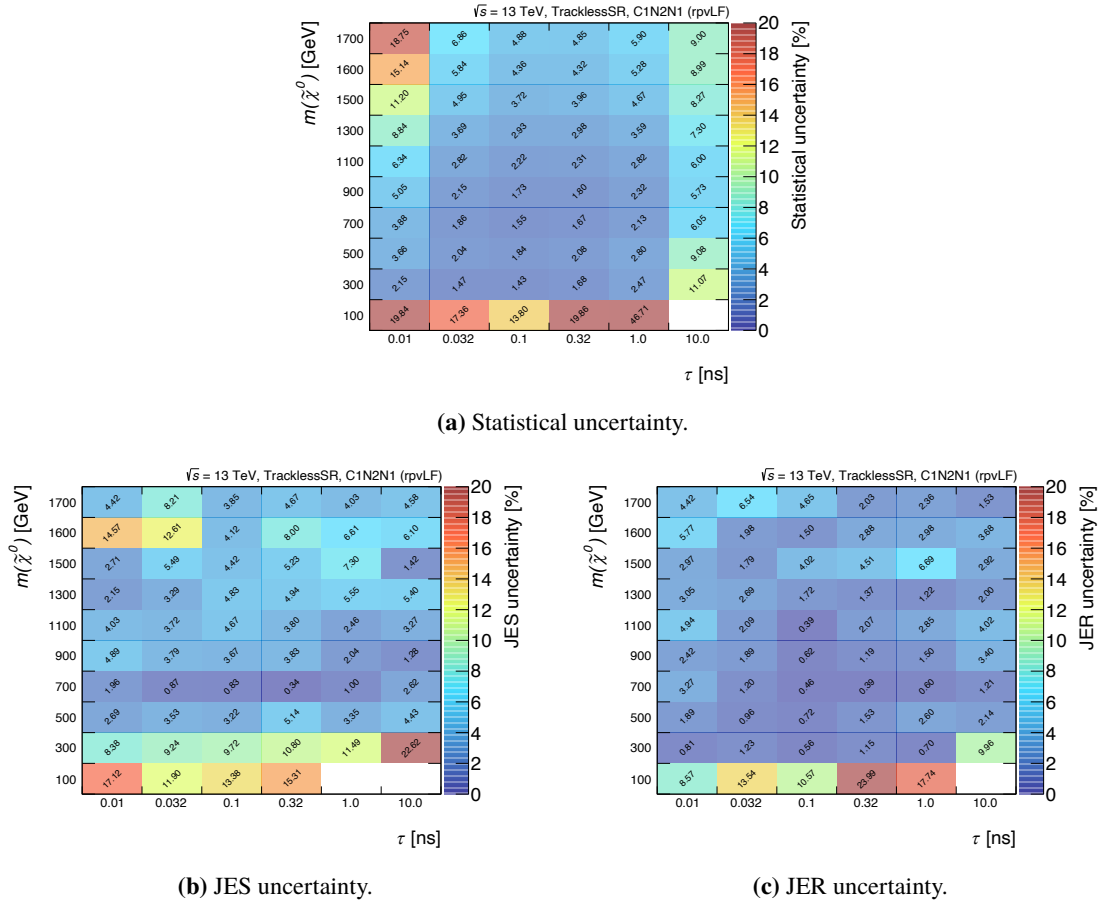


**Figure 8.6:** Uncertainties for the electrowino pair production models in the Trackless SR.

for the small mass difference and the small neutralino mass types. For each bin in radius  $R_{xy}$  and  $z$ , the jet  $p_T$  response distribution is fitted with a gaussian and the mean value and the standard deviation are used as the center value and error bar. In the plots, the value in the bin closest to the interaction point is set to 1 and the difference with this is plotted.

For the small mass difference case, both of the difference from the value in the closest bin and the standard deviation of the jet  $p_T$  response increase with the displacement of the jets. For the large mass difference and small neutralino mass case, the effect is smaller since the direction between the neutralinos and jets should be more collinear.

The distribution of the  $R_{xy}$  and  $z$  positions of the jet was investigated to assess the impact of the difference of the jet  $p_T$  response depending on the jet displacement on the analysis. Figures 8.9 and 8.10 show the distribution of the jet generated position. 90% of the jets originate from the neutralino decays within 300 mm in radius and  $|z|$ . The jet  $p_T$  response is consistent with the value in the closest bin in this region. This implies that the impact of the different of the jet  $p_T$  response due to the jet displacement is a few in this analysis, and no additional uncertainty is assigned to the jet  $p_T$  due to the displacement.

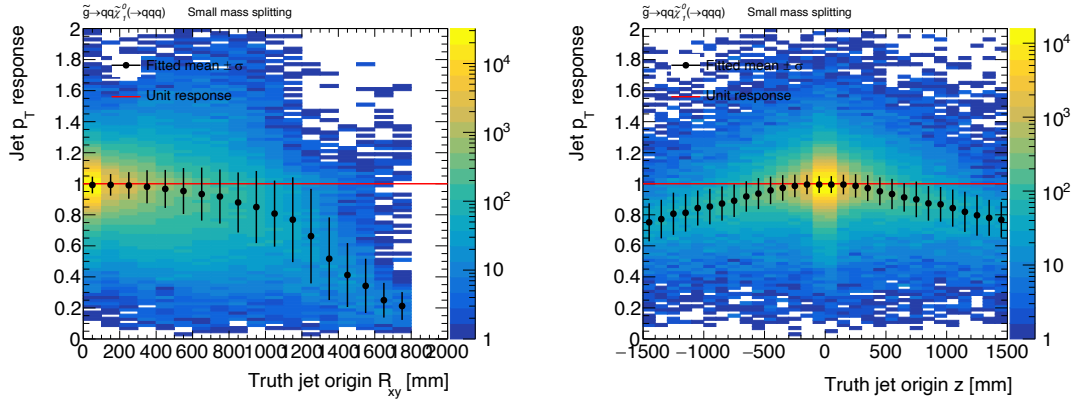


**Figure 8.7:** Jet  $p_T$  response as a function of the decay position radius  $R_{xy}$  (left) and  $z$  (right) of the neutralino matched to the truth jet, for the **small mass difference** case. The value in the bin closest to the interaction point is set to 1.

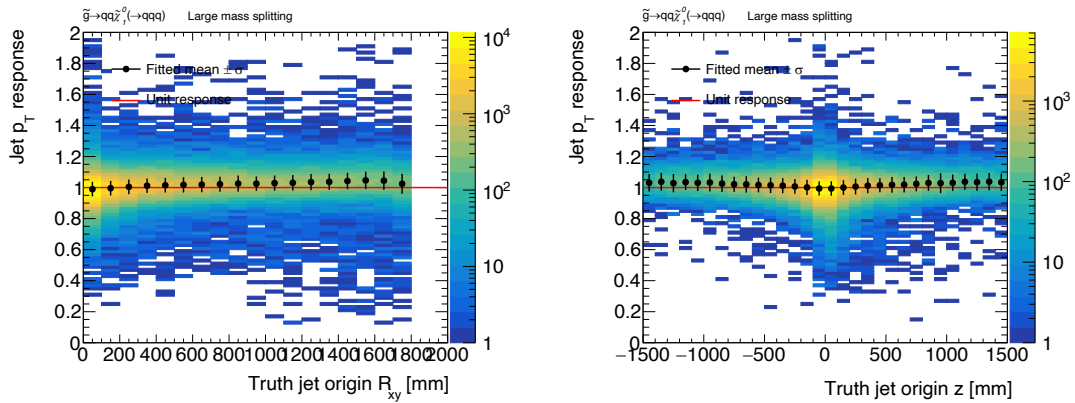


**Figure 8.8:** Jet  $p_T$  response as a function of the decay position radius  $R_{xy}$  (left) and  $z$  (right) of the neutralino matched to the truth jet, for the set of signal samples with **large mass difference and small neutralino mass** case. The value in the bin closest to the interaction point is set to 1.

### 8.3 Pile-up uncertainties

The changes in the pile-up may result in changes in the number of DVs, and the signal selection efficiency may be changed. Therefore, the uncertainty for signal selection efficiency due to change in pileup is calculated. To estimate this effects, signal samples has been reweighted to match the number of interactions per bunch crossing distribution observed in data, and the differences of the selection efficiency between weighted and not weighted samples are assigned as the systematic uncertainty. The relative change on the number of events passing the SR selections is always below 2%, and mostly below 1%, for both signal models and both signal regions. They are much smaller than the statistical uncertainties in the case which the selection efficiency is very low. It means that signal events pass

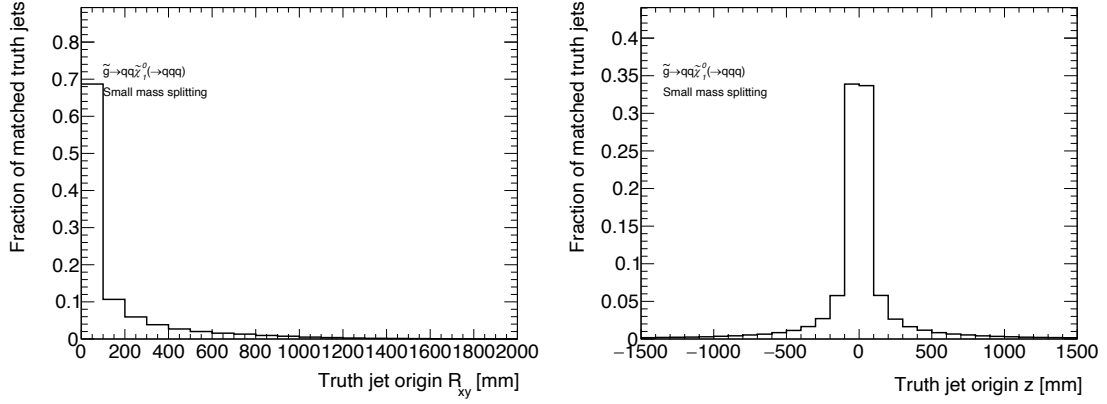


**Figure 8.9:** Fraction of truth jets matched to reconstructed jets in each bin of radius  $R_{xy}$  (left) and  $z$  (right) for the **small mass difference** case.

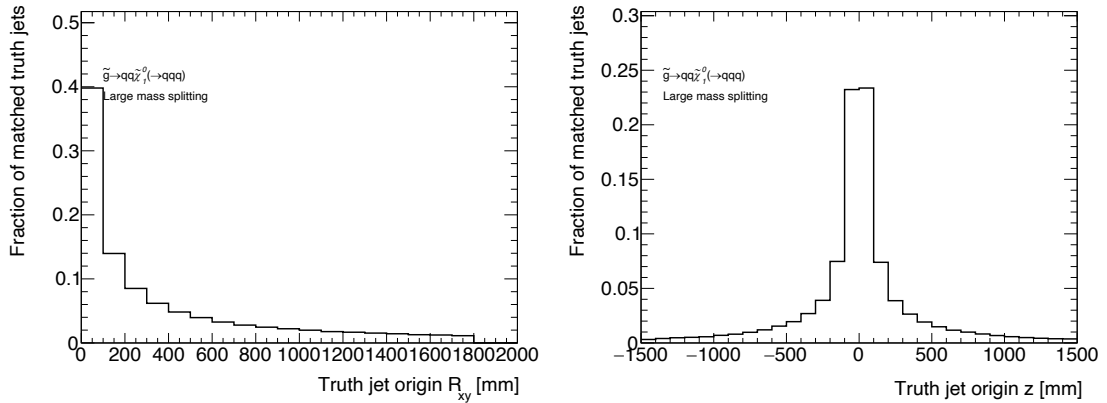


**Figure 8.10:** Fraction of truth jets matched to reconstructed jets in each bin of radius  $R_{xy}$  (left) and  $z$  (right) for the **large mass difference and small neutralino mass** case.

the selection due to the DVs corresponding to a genuine LLP decay.

## 8.4 Theoretical uncertainties

Uncertainties on the inclusive cross section used to normalized the gluino pair production models and electrowino pair production models are taken from Ref. [88]. The uncertainty of the cross section includes the effect of the uncertainties of PDF, QCD factorization factor, QCD renormalization factor, and QCD coupling constant. Based on the uncertainty, the signal events were reweighted and the impact on signal selection efficiency was estimated.

In addition, the uncertainty due to the ISR modeling need to be considered. This is because jet selection efficiency may be affected by uncertainties in the ISR modeling. To estimate this effect, the QCD factorization factor, QCD renormalization factor, and merging scales are varied

in the MADGRAPH5\_AMC@NLO 2.6.2, as well as in the parton showering and radiation tunings. The difference between the number of the events from nominal and varied samples is applied to the systematic uncertainty. The uncertainties for the electrowikino pair production models with the neutralino mass of  $m < 500$  GeV are the largest, about 20%, and the uncertainty decreases as the mass increases. The uncertainties for the gluino pair production models are negligible.

The systematic uncertainties affecting the number of signal events in both signal regions is summarized in Table 8.2.

**Table 8.2:** Summary of the systematic uncertainties on the predicted number of the events for the signal models. These uncertainties apply to both SRs used in the search.

Source of uncertainty	Value of uncertainties [%]	
	Gluino pairs	Electroweakino pairs
Total	17–20	20–31
Tracking and vertex reconstruction		14–17
Jet energy scale and resolution	< 1	1–10
Pile up		< 2
ISR modeling	< 1	1–24
Integrated luminosity of dataset		1.7

## Chapter 9

# Results

### 9.1 Expected signal yields

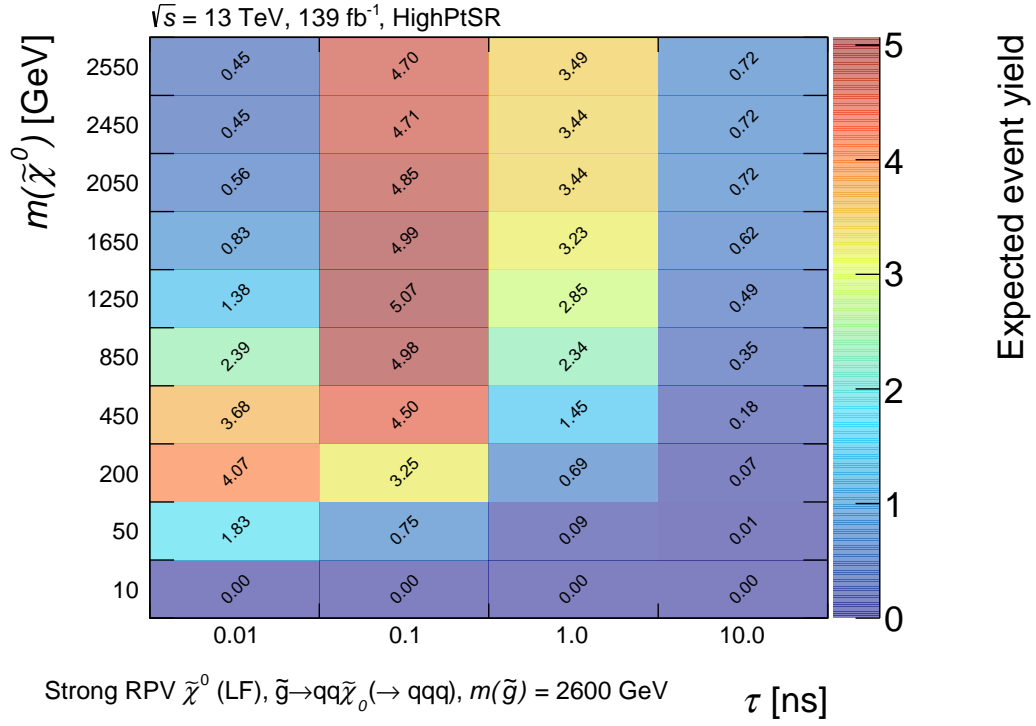
The High- $p_T$  SR is designed to primarily target the gluino pair production model. The expected number of signal events for this model in the High- $p_T$  SR is shown in Figure 9.1(a) for a fixed gluino mass of 2600 GeV, that is close to the expected sensitivity, as a function of the neutralino mass and lifetime. Figure 9.1(b) shows the expected number of signal events when fixing the neutralino lifetime to 0.1 ns, corresponding to the maximum expected sensitivity, and varying the gluino and neutralino masses. The Trackless SR is not sensitive for this model.

For the electrowikino pair production model, both SRs are sensitive for high neutralino mass and low neutralino mass, respectively. The expected number of signal events are shown in Figures 9.2 as a function of the mass and lifetime of the electrowikino.

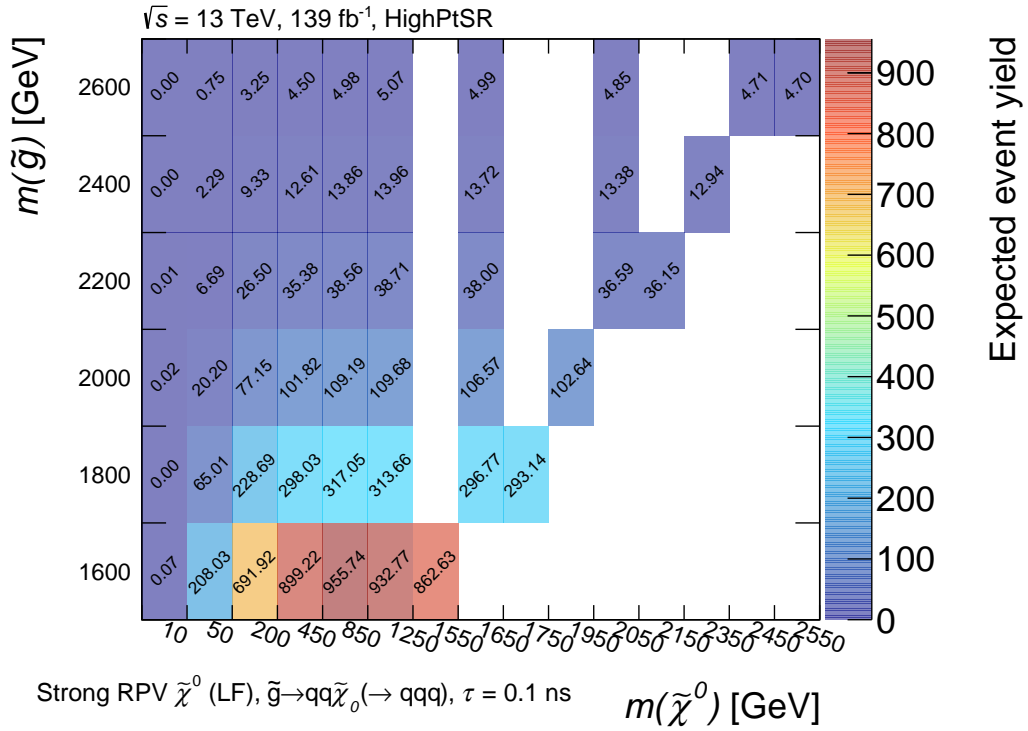
### 9.2 Observed yields

No events are observed in the Trackless SR, while a single event is observed in the High- $p_T$  SR. The observed number of events not significantly deviated from the expected number of background events. Figure 9.3 shows the two-dimensional distributions of the DV mass  $m_{DV}$  and the track multiplicity  $N_{Trk}$  in events passing the jet selections of the High- $p_T$  and Trackless SRs in data and signal MC.

The single event observed in the High- $p_T$  SR contains seven jets with  $p_T$  above 90.8 GeV and 1 DV passing the selections. The DV is reconstructed from five tracks,  $m_{DV} = 32.6$  GeV, and net electric charge of  $-1e$ . An event display of the observed event is shown in Figure 9.4.



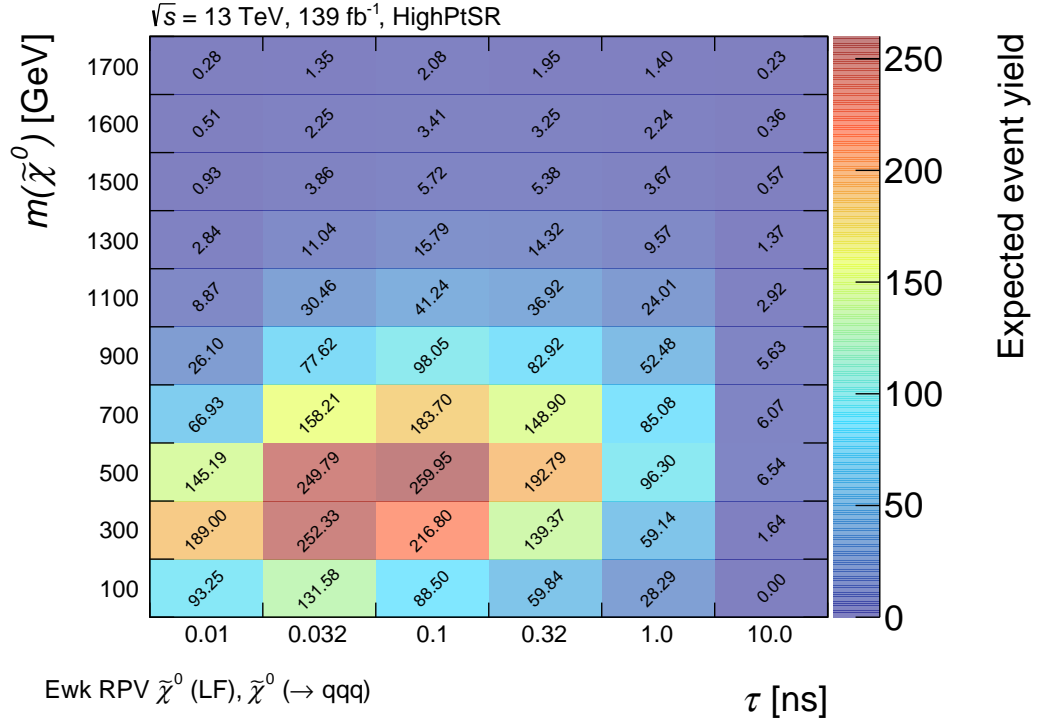
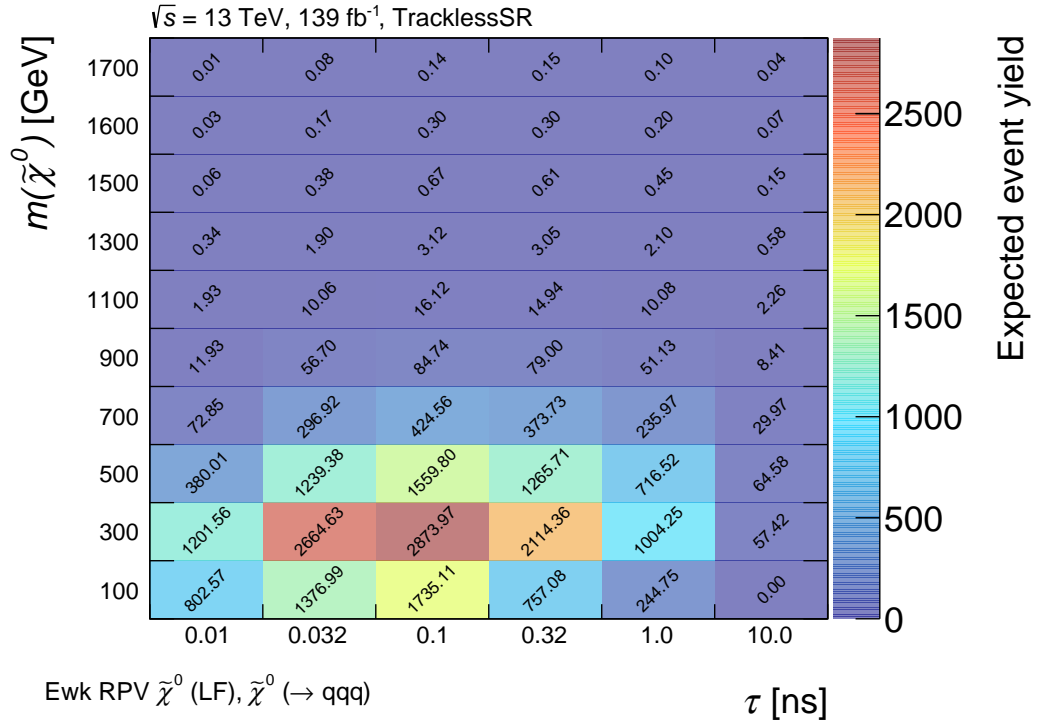
(a) The gluino mass is fixed at 2600 GeV, and the neutralino mass and lifetime are varied.



(b) The neutralino lifetime is fixed at 0.1 ns, the gluino and neutralino masses are varied.

**Figure 9.1:** Expected number of signal events for the gluino pair production model.



(a) High- $p_T$  SR

(b) Trackless SR

**Figure 9.2:** Expected number of signal events for the electrowikino pair production model as a function of the mass and lifetime of the electrowikino.

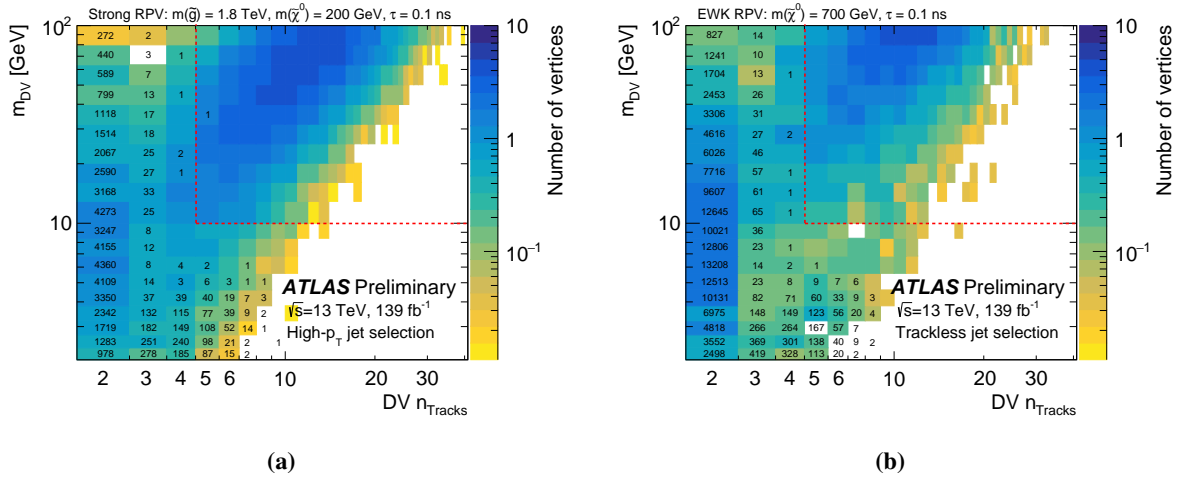


**Figure 9.3:** Two-dimensional distribution of the DV mass  $m_{\text{DV}}$  and the track multiplicity  $N_{\text{Trk}}$  in events passing the jet selections of (a) the High- $p_T$  SR and (b) the Trackless SR in data and signal MC. The shown numbers correspond to the observed number of vertices in data, while the color-representation shows the expected number of vertices of two targeted signal models. The dashed line represents the boundary of the signal region requirements.

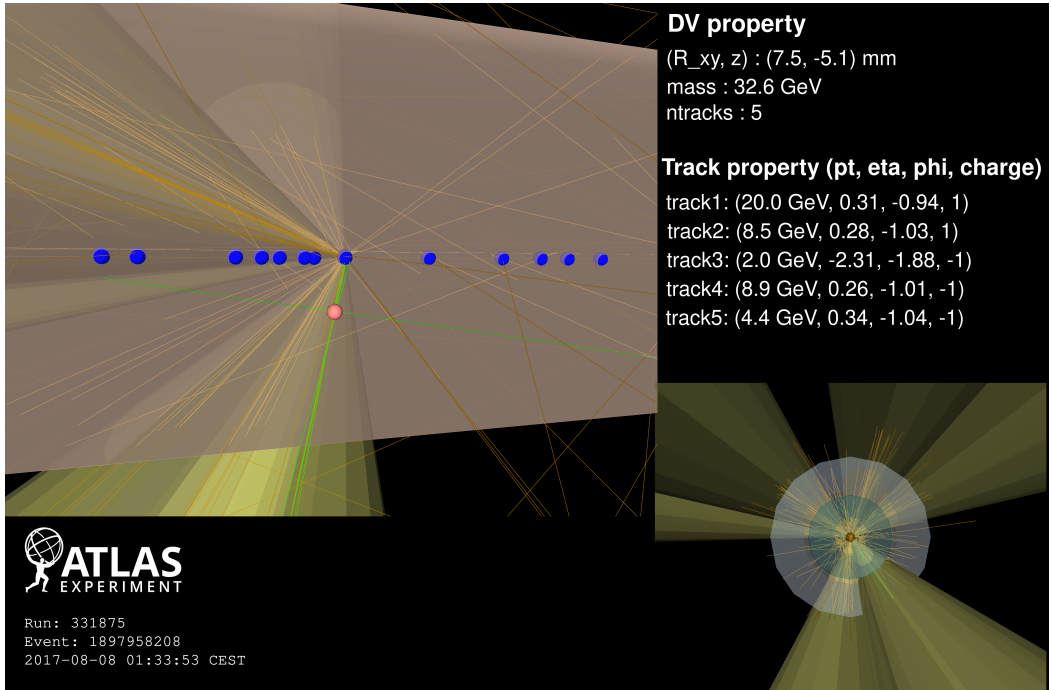


**Figure 9.4:** An event display of the event observed in the SR in data. The display shows primary vertices (blue spheres), the DV (pink sphere), tracks associated with the DV (green lines), other tracks with  $p_T > 2 \text{ GeV}$  and at least 7 SCT hits (orange lines), jets (yellow cones), and the beam pipe (light gray tube).

# Chapter 10

## Discussion

### 10.1 Constraint for the focused RPV SUSY models

The expected number of background events and observed number of events in the two signal regions are used simultaneously to set exclusion limits on the target signal models. The exclusion limits are set using the  $CL_s$  prescription [89]. The exclusion limit setting is implemented in pyhf 0.6.3 [90, 91]. It is done using a two-bin fit, which correspond to the High- $p_T$  and Trackless SRs, respectively.

Figure 10.1 shows the expected and observed 95% CL exclusion limits on the mean proper lifetime of a long-lived neutralino and the gluino mass in gluino pair production events for a fixed neutralino mass of 200 GeV. At 95% confidence level, the gluino mass up to 2600 GeV is excluded for the neutralino lifetime of 0.01 ns. Figure 10.2 shows the expected and observed 95% CL exclusion limits on the mass and mean proper lifetime of a long-lived neutralino in gluino pair production events for a fixed gluino mass of 2400 GeV. The expected and observed 95% CL exclusion limits on the mass of a long-lived electrowikino as a function of lifetime for the electrowikino pair production model are shown in Figure 10.3. For a mean proper electrowikino lifetime of 0.1 ns, electrowikino masses up to 1.58 TeV are excluded independently of the presence of a heavier gluino. The observed limit extends above electrowikino mass of 1.5 TeV for a range of mean proper lifetimes between 0.03 ns and 1 ns. Stronger limits can be set when the neutralino is produced in the decay of a heavier gluino as shown in Figure 10.2. For neutralino masses on the order of a few hundred GeV and below, the sensitivity decreases because the neutralino is Lorenz-boosted and flies to a position where the decay vertex of the neutralino can no longer be reconstructed. In the HL-LHC ATLAS experiment, scheduled to begin in 2029, further search is expected with increased integrated luminosity ( $3000 \text{ fb}^{-1}$ ) and the following inner detector upgrade [92].

- Increasing the detector coverage area from  $|\eta| < 2.5$  to  $|\eta| < 4$  increases the acceptance of the jet and improves signal acquisition efficiency.
- Extension of the silicon detector installation position allows the reconstruction of signals with a longer lifetime. The location of the reconstructable decay point is extended from 300 mm to 400 mm.
- The vertex positional resolution improves from  $O(10) \text{ } \mu\text{m}$  to  $O(1) \text{ } \mu\text{m}$  by pixel detector subdivision, and the signal selection efficiency in the short lifetime region is increased.

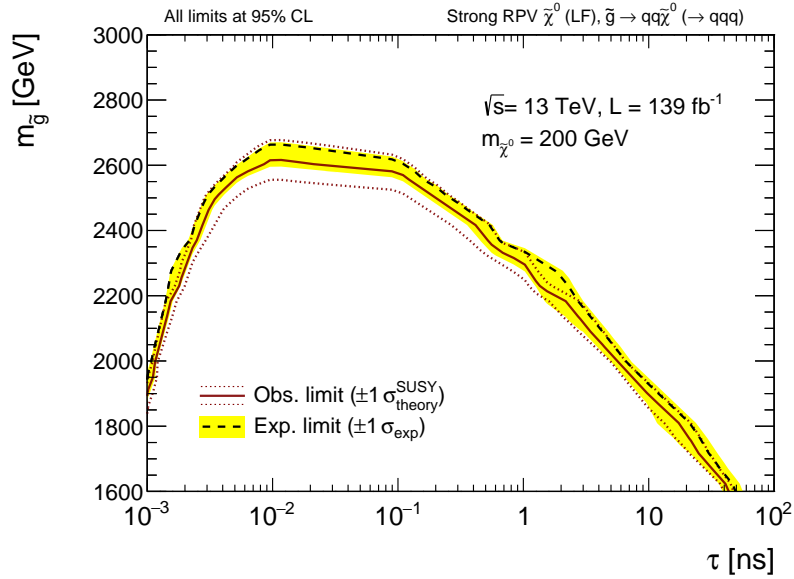


**Figure 10.1:** Exclusion limits at 95% CL on the lifetime of the neutralino and the mass of the gluino in the gluino pair production model for a fixed neutralino mass of 200 GeV. The black dashed line and the yellow shaded band are the expected exclusion limit and its  $\pm 1\sigma$  uncertainty, respectively. The red thick solid line is the observed exclusion limit for the central value of the signal cross section. The expected and observed limits do not include the effect of the theoretical uncertainties in the signal cross section. The red dotted lines show the effect on the observed limit of varying the signal cross section by  $\pm 1\sigma$  of the theoretical uncertainty. The area below the curve line is the excluded parameter space.

In addition, in Figure 10.4, 95% CL upper limits on the production cross section of these signal models are shown as a function of gluino masses for various values of neutralino lifetimes. For the neutralino lifetime of 0.1 ns, cross section upper limit is set below 40 ab.

Model-independent upper limits at 95% CL on the number of BSM events in the signal region are also derived, assuming no significant contamination from alternate signal models in the CRs used to derive the background estimations. Normalizing these limits by the integrated luminosity of the data sample, these numbers can be interpreted as upper limits on the visible cross section for any BSM models, denoted by  $\sigma_{\text{vis}}$ . This is defined as the product of signal acceptance, reconstruction efficiency, and production cross section, and the results are shown in Table 10.1.

## 10.2 Reinterpretation of the results

There are various models other than the models focused on in this analysis, in which the BSM particles have a long lifetime. There are not enough CPU resources to perform special reconstructions on all of these models and interpret the results, and the reconstruction itself can only be performed by ATLAS collaborators. In this section, the study is described that allows people including those who are not members of the ATLAS collaboration to reinterpret the results of this search in many models predicting displaced vertices in multi-jet events.

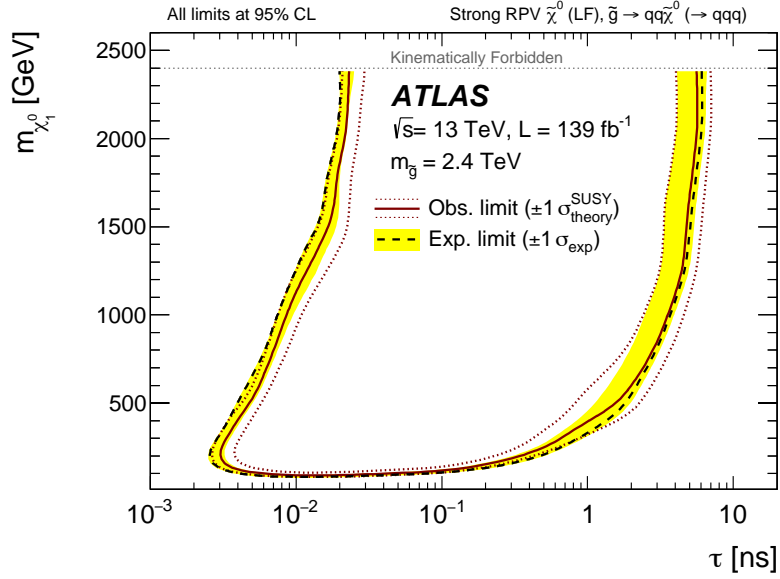


**Figure 10.2:** Exclusion limits at 95% CL on the lifetime and mass of the neutralino in the gluino pair production model for a fixed gluino mass of 2400 GeV. The black dashed line and the yellow shaded band are the expected exclusion limit and its  $\pm 1\sigma$  uncertainty, respectively. The red thick solid line is the observed exclusion limit for the central value of the signal cross section. The expected and observed limits do not include the effect of the theoretical uncertainties in the signal cross section. The red dotted lines show the effect on the observed limit of varying the signal cross section by  $\pm 1\sigma$  of the theoretical uncertainty. The area between the two solid curves is the excluded parameter space.

**Table 10.1:** The expected and observed number of events, observed ( $S_{\text{obs}}^{95}$ ) and expected ( $S_{\text{exp}}^{95}$ ) limits on the number of signal events to exclude the model, and 95% CL upper limits on the visible cross section  $\langle \sigma_{\text{vis}} \rangle_{\text{obs}}^{95}$ .

Signal Region	Observed	Expected	$S_{\text{obs}}^{95}$	$S_{\text{exp}}^{95}$	$\langle \sigma_{\text{vis}} \rangle_{\text{obs}}^{95}$ [fb]
High- $p_T$ SR	1	$0.46_{-0.30}^{+0.27}$	4.5	$4.0_{-1.4}^{+0.7}$	0.032
Trackless SR	0	$0.83_{-0.53}^{+0.51}$	3.3	$4.4_{-0.4}^{+0.6}$	0.024

To reinterpret the results, the number of events remaining in the SRs are needed for each model. This is derived using only particle-level information from before the detector simulation and called *parameterized efficiencies*. The efficiencies should be applied to vertices and events which pass certain acceptance requirements at particle-level in Monte Carlo simulations.

The parameterized efficiencies pseudo-calculate the fractions of events passing the SR selection ( $P$ ), given symbolically by:

$$P = \mathcal{A}_{\text{event}} \varepsilon_{\text{event}} \times \left( 1 - \prod_{\text{vertices}} (1 - \mathcal{A}_{\text{vertex}} \varepsilon_{\text{vertex}}) \right), \quad (10.1)$$

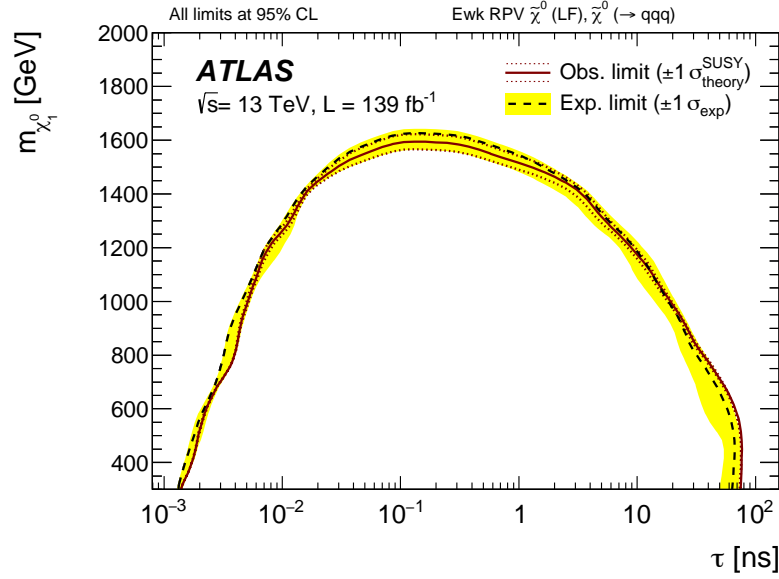


**Figure 10.3:** Exclusion limits at 95% CL on the lifetime and mass of the electrowikino in the electroweakino pair production model. The black dashed line and the yellow shaded band are the expected limit and its  $\pm 1\sigma$  uncertainty, respectively. The red thick solid line is the observed limit for the central value of the signal cross section. The expected and observed limits do not include the effect of the theoretical uncertainties in the signal cross section. The red dotted lines show the effect on the observed limit of varying the signal cross section by  $\pm 1\sigma$  of the theoretical uncertainty. The area below the curve line is the excluded parameter space.

where  $\mathcal{A}_{\text{event}}$  and  $\mathcal{A}_{\text{vertex}}$  are the fractions of events passing the event-level and vertex-level acceptance requirements described in Section 10.2.1. The  $\varepsilon_{\text{event}}$  and  $\varepsilon_{\text{vertex}}$  factors are the parameterized efficiencies passing the event-level and vertex-level selections defined in Section 10.2.2, provided the acceptance is fulfilled.

### 10.2.1 Definition of acceptances

The event-level and vertex-level parameterized efficiencies are provided for events passing the event-level and vertex-level acceptance requirements, respectively. The event-level acceptance requirements are prepared for the High- $p_T$  SR and the Trackless SR separately. The event-level acceptance requires the presence of several truth jets. Truth jets are reconstructed using an anti- $k_t$  algorithm of radius  $R = 0.4$  from all stable particles, excluding neutrinos and muons. Note that this definition includes particles from the long-lived particle (LLP) decay. We additionally define displaced truth jets as those reconstructed only using decay products of the LLP decay, with the same parameters and selections above and the additional requirement that particles have  $|\eta| < 2.5$ . All displaced truth jets that originate from LLPs decaying outside the calorimeter ( $R > 3870$  mm) are not used for the selections. Table 10.2 summarizes the selections on truth jets for the event-level acceptance calculation.

The common vertex-level acceptance requirements are provided for the two SRs. The vertex-level

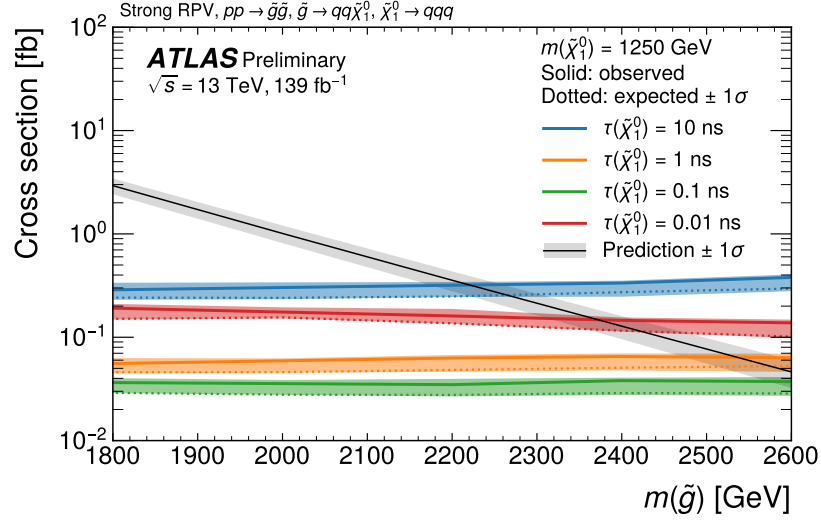


**Figure 10.4:** Exclusion limits at 95% CL on the production cross section of the gluino pairs as a function of gluino mass are shown for several values of neutralino lifetime along with the expected (dotted lines) and observed (solid lines) signal production cross section and its theoretical uncertainty in the signal cross section (colored shaded band).

**Table 10.2:** Summary of the truth jet selections. The  $x$  in the  $n_{\text{jet/displaced jet}}^x$  notation refers to the jet  $p_T$  threshold in GeV.

Signal Region	High- $p_T$ SR	Trackless SR
Truth jet selection	$n_{\text{jet}}^{250} \geq 4$ or $n_{\text{jet}}^{195} \geq 5$ or $n_{\text{jet}}^{116} \geq 6$ or $n_{\text{jet}}^{90} \geq 7$	$n_{\text{jet}}^{137} \geq 4$ or $n_{\text{jet}}^{101} \geq 5$ or $n_{\text{jet}}^{83} \geq 6$ or $n_{\text{jet}}^{55} \geq 7$ , $n_{\text{displaced jet}}^{70} \geq 1$ or $n_{\text{displaced jet}}^{50} \geq 2$

acceptance requires a displaced decay vertex of the heavy long-lived particle to have the following properties:

- The transverse distance between the primary vertex and the decay position must be greater than 4 mm.
- The decay position must lie within the fiducial volume of  $R_{xy} < 300$  mm and  $|z| < 300$  mm.
- At least 1 charged particle in the displaced heavy particle decay must have an approximate transverse impact parameter  $|d_0| \equiv R_{\text{decay}} \times \sin \Delta\phi > 2$  mm, where  $R_{\text{decay}}$  is the transverse distance between the interaction point and the massive particle decay, and  $\Delta\phi$  is the azimuthal angle between the particle momentum at its creation and the vector from the primary vertex to the position of the displaced decay.
- The number of *selected decay products* (described below) must be at least 5.
- The invariant mass of the displaced heavy particle must be larger than 10 GeV. The invariant mass of the displaced heavy particle decay vertex is constructed using the momenta of the

*selected decay products* with a charged-pion mass (consistent with the assumptions in the DV reconstruction used in the analysis).

The selected decay products used in the decay vertex construction of the displaced heavy particle are those decay products of a given massive particle decay that satisfy the following conditions:

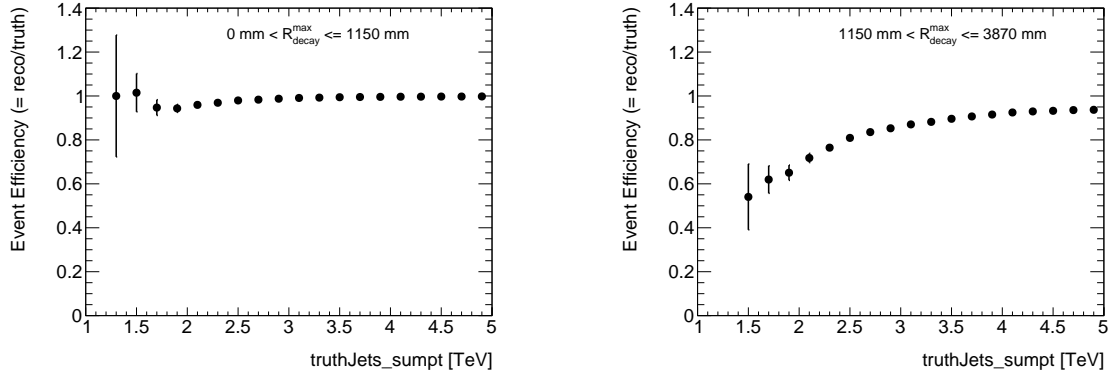
- The particle is charged and stable for timescales required to traverse the tracking volume.
- The particle has transverse momentum  $p_T$  and electric charge  $q$  such that  $p_T / |q| > 1$  GeV.

### 10.2.2 Efficiencies

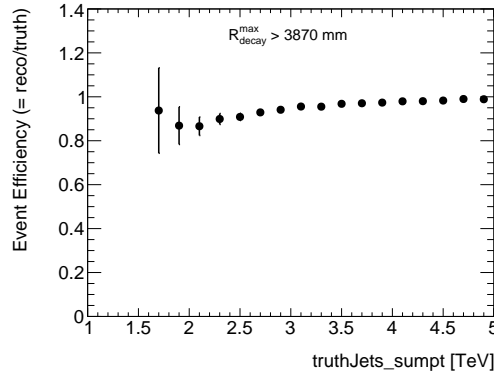
The parameterized efficiencies are provided at the event-level and vertex-level, respectively. Because of the inability for the ATLAS detector to fully measure the energy of jets that are produced within or beyond the calorimeter, the event-level efficiency  $\varepsilon_{\text{event}}$  is provided as a function of the sum of truth jets  $p_T$  and the transverse distance of the furthest long-lived particle decay. The event-level efficiencies for the High- $p_T$  SR are defined as the number of reconstructed events that pass the multi-jet trigger, high- $p_T$  jet filter, and the high- $p_T$  jet selection defined in Section 6, divided by the number of events which satisfy the event-level acceptance requirements for the High- $p_T$  SR. The number of events is calculated using the gluino pair production model targeted by the High- $p_T$  SR. Similarly, the efficiencies for the Trackless SR are defined as the number of reconstructed events that pass the multi-jet trigger, low- $p_T$  and trackless jet filter, and the low- $p_T$  and trackless jet selection, divided by the number of events which satisfy the event-level acceptance requirements for the Trackless SR. The number of events is calculated using the electrowino pair production model targeted by the Trackless SR. These efficiencies can be found in Figures 10.5 and 10.6. In Figure 10.6, the efficiency requirements include the requirement that the events "fail the high- $p_T$  jet selection", but it is not included in the acceptance requirements, resulting in lower efficiencies in regions where the sum of truth jets  $p_T$  is large.

In addition to this event-level efficiency, events entering the SR are required to have at least one selected decay vertex of the displaced heavy particle. For each heavy particle decay, the vertex-level efficiencies  $\varepsilon_{\text{vertex}}$  are provided as a function of the invariant mass of the decay vertex of the displaced heavy particle and the number of selected decay products using events which pass the event-level acceptance requirements. Considering the effects of the material map veto, the efficiencies are binned by the transverse distance of the long-lived particle decay. The per-vertex efficiency is defined as the number of decay vertices of the displaced heavy particle that can be matched to a reconstructed DV which passes the full DV selection as defined in Section 6, divided by the number of decay vertices of the displaced heavy particle which satisfy the vertex-level acceptance requirements. The number of vertices are calculated using the gluino pair production samples due to high statistics. These efficiencies can be found in Figures 10.7 and 10.8.





(a) All displaced heavy particle decay occurring before the start of the calorimeter. (b) The farthest displaced heavy particle decay occurring inside the calorimeter.

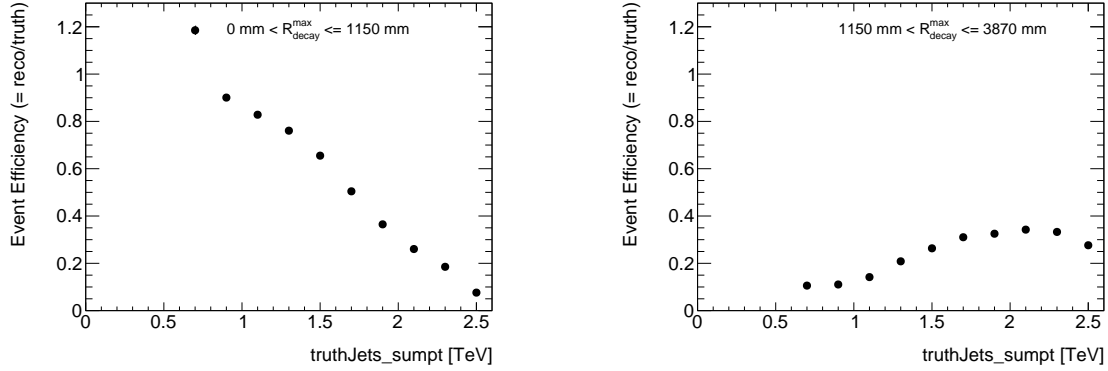


(c) The farthest displaced heavy particle decay occurring after the end of the calorimeter.

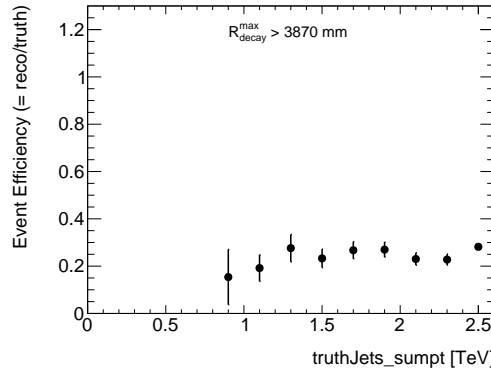
**Figure 10.5:** Parameterized event-level efficiencies for the High- $p_T$  SR are shown as a function of the sum of truth jets  $p_T$ . The event-level efficiencies are evaluated separately for events which have all displaced heavy particle decay occurring before the start of the ATLAS calorimeter, the farthest displaced heavy particle decay occurring inside the calorimeter, and the farthest displaced heavy particle decay occurring after the end of the calorimeter.

### 10.2.3 Validation

To test the accuracy of these parameterized efficiencies, validations are performed. The probability which the events pass the SR selections is calculated using the fraction of the number of events passing the acceptance requirements, as well as the event-level and vertex-level efficiency histograms. The number of events passing the selection predicted by the fraction of the number of events passing the acceptance requirements and the parameterized efficiencies (*Param.  $\mathcal{A}\varepsilon$* ) is defined as the sum of the per-event probabilities in the sample. This prediction is compared to the actual number of events passing the full SR selections using reconstructed quantities (*Full Reco.  $\mathcal{A}\varepsilon$* ). Figure 10.9 shows the validation results of the parameterized efficiencies for the High- $p_T$  SR using the gluino pair production model which are the same models used to derive parameterized efficiencies for the High- $p_T$  SR. For



(a) All displaced heavy particle decay occurring before the start of the calorimeter. (b) The farthest displaced heavy particle decay occurring inside the calorimeter.



(c) The farthest displaced heavy particle decay occurring after the end of the calorimeter.

**Figure 10.6:** Parameterized event-level efficiencies for the Trackless SR are shown as a function of the sum of truth jets  $p_T$ . The event-level efficiencies are evaluated separately for events which have all displaced heavy particle decay occurring before the start of the ATLAS calorimeter, the farthest displaced heavy particle decay occurring inside the calorimeter, and the farthest displaced heavy particle decay occurring after the end of the calorimeter.

each signal samples with various gluino mass, neutralino mass, and neutralino lifetime, the *relative difference* defined as  $[(\text{Param. } \mathcal{A}_\varepsilon - \text{Full Reco. } \mathcal{A}_\varepsilon) / \text{Full Reco. } \mathcal{A}_\varepsilon]$  is displayed at the event-level, vertex-level, and total  $\mathcal{A}_\varepsilon$ . For the event-level, the Full Reco.  $\mathcal{A}_\varepsilon$  is defined as the ratio of the number of reconstructed events passing the jet selections as expected by the full ATLAS simulation and the total number of generated events. The Param.  $\mathcal{A}_\varepsilon$  is defined as the ratio of the number of events passing the jet selections estimated using the set of parameterized efficiencies and the total number of events. The number of events passing the jet selections is estimated by weighting each event that satisfies the acceptance requirement with a parameterized efficiency according to the sum of truth jet  $p_T$  and summing the weighted number of events. For the vertex-level, the Full Reco.  $\mathcal{A}_\varepsilon$  is defined as the ratio of the number of the decay vertices of the displaced heavy particle matched to a reconstructed DV which passes the full DV selections and the total number of the decay vertices of the displaced

heavy particle in the event passing the event-level acceptance requirements. The Param.  $\mathcal{A}_\varepsilon$  is defined as the ratio of the number of the decay vertices of the displaced heavy particle passing the full DV selections estimated using the set of parameterized efficiencies and the total number of the decay vertices of the displaced heavy particle in the event passing the event-level acceptance requirements. The the number of the decay vertices of the displaced heavy particle passing the full DV selections is estimated by weighting each vertex that satisfies the acceptance requirement with a parameterized efficiency according to the invariant mass of the decay vertices of the displaced heavy particle and the number of selected decay products and summing the weighted number of vertices. The total Full Reco.  $\mathcal{A}_\varepsilon$  is defined as the ratio of the number of reconstructed events passing the *High- $p_T$*  SR defined in the Section 6.1 and the total number of generated events. The total Param.  $\mathcal{A}_\varepsilon$  is calculated by the Equation 10.1.

In Figure 10.10, the value of the *difference* is shown in one dimension with only signal grids which satisfy the following considerations, which indicate requirements for models that the efficiencies can safely.

1. Parameterized efficiencies are calculated for sensitive regions in this analysis, so they may not adapt well to regions with low sensitivity. Therefore, the parameterized efficiencies are recommended to be applied to models with a fraction of 10% or more vertices that satisfy the event-level acceptance requirements and also satisfy the vertex-level acceptance requirements ( $\mathcal{A}_{\text{event}}\mathcal{A}_{\text{vertex}} > 10\%$ ).
2. The event-level acceptance requirements for the Trackless SR do not include the "fail high- $p_T$  jet selection" requirement. Therefore, in addition to the conditions for  $\mathcal{A}_{\text{event}}\mathcal{A}_{\text{vertex}}$  above, the parameterized efficiencies of the Trackless SR should not be used for models where 90% or more of the events pass the event-level acceptance requirements for the High- $p_T$  SR.
3. LLP lifetimes of less than 10 ns are recommended for models where jets primarily originate from the decay of LLPs. This is because the parameterization is not accurate in cases where all LLPs decay inside or after the calorimeter.

Similarly, Figures 10.11 and 10.12 show the validation results of the efficiencies for the Trackless SR using the MC samples of the electroweakino pair production model which are the same samples used to derive parameterized efficiencies for the Trackless SR.

From these results, the expected numbers of events passing the selection at the High- $p_T$  and the Trackless SR both agree within 13%. This value should be taken into account as a systematic uncertainty to the expected number of signal events when using this reinterpretation method.

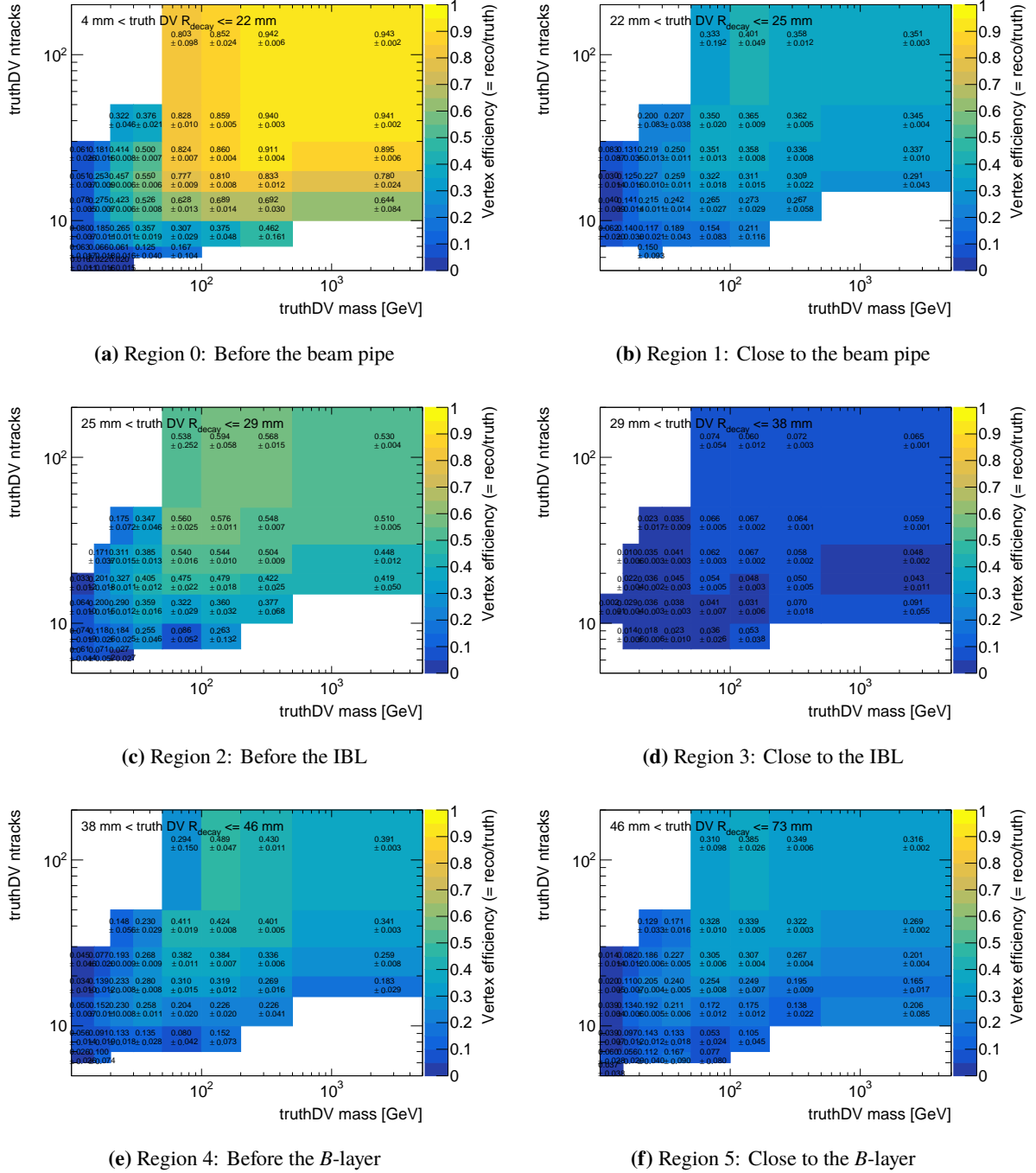


**Figure 10.7:** Parameterized vertex-level efficiencies as a function of the invariant mass of the decay vertex of the displaced heavy particle and the number of selected decay products. Selected decay products are required to have nonzero electric charge and  $p_T > 1$  GeV as described in the text. Vertex-level efficiencies are given separately for 11 radial region.

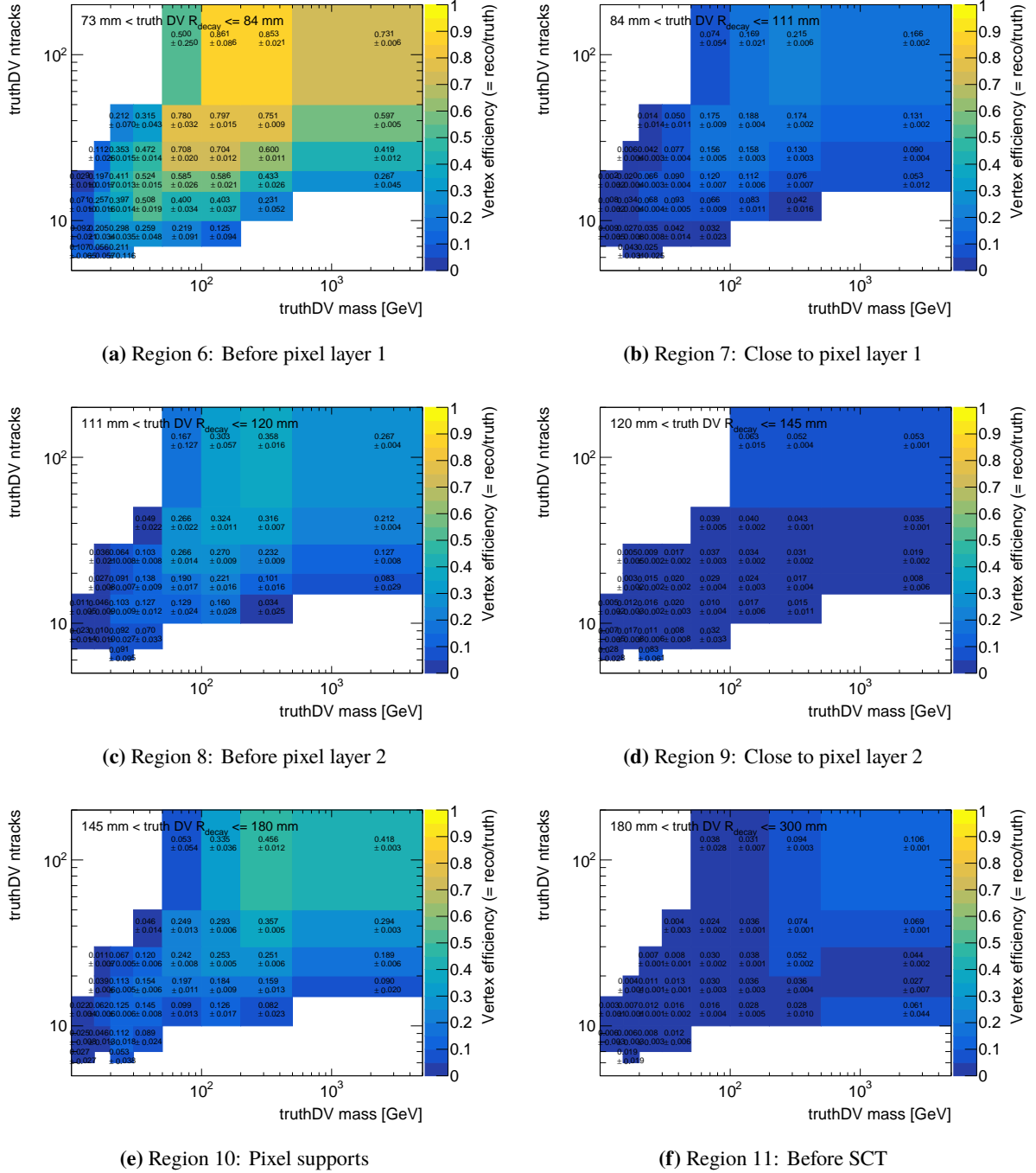


**Figure 10.8:** (Cont'd) Parameterized vertex-level efficiencies as a function of the invariant mass of the decay vertex of the displaced heavy particle and the number of selected decay products. Selected decay products are required to have nonzero electric charge and  $p_T > 1$  GeV as described in the text. Vertex-level efficiencies are given separately for 11 radial region.

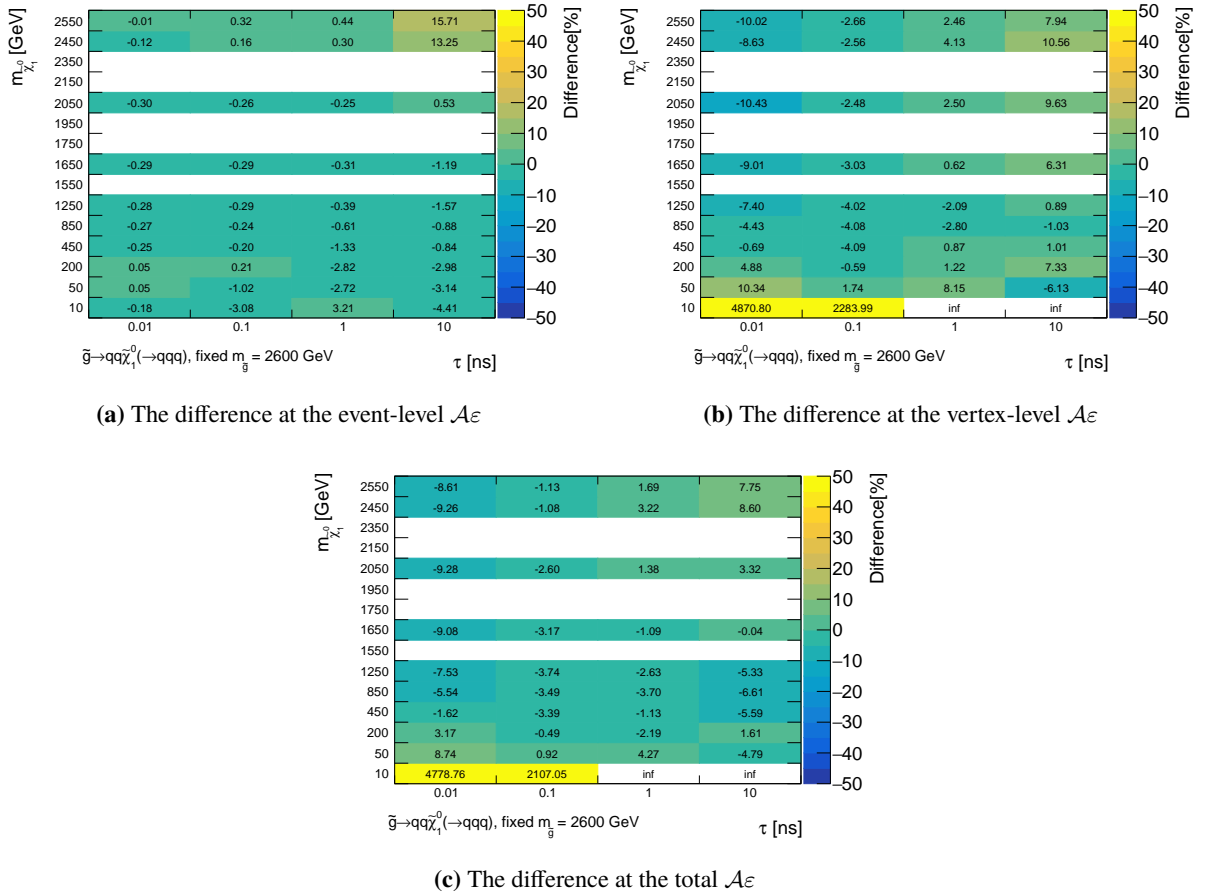


**Figure 10.9:** The value of the *difference* at the event-level, vertex-level, and total  $\mathcal{A}_\varepsilon$  in the High- $p_T$  SR for the signal scenarios with neutralinos produced via gluinos. The gluino mass is fixed at 2.6 TeV. The highest non-closure signal grid is the 10 GeV neutralino with a lifetime of 0.01 ns that has the difference of 4779%, the Full Reco.  $\mathcal{A}_\varepsilon$  is 0.01% and the Param.  $\mathcal{A}_\varepsilon$  is 0.6%.

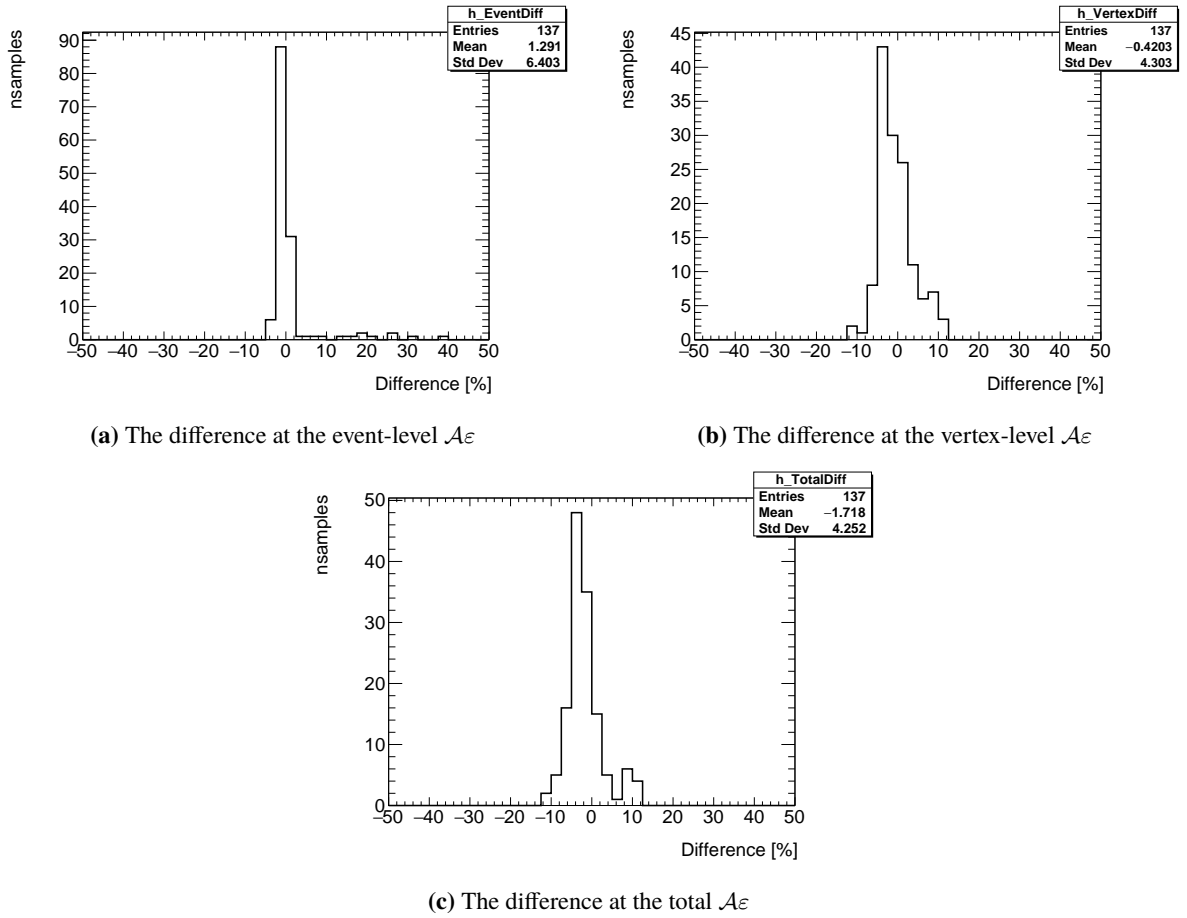


**Figure 10.10:** One dimensional histograms of the *difference* in Figure 10.9 for only signal grids with total Full Reco.  $\mathcal{A}\varepsilon$  larger than 10%.

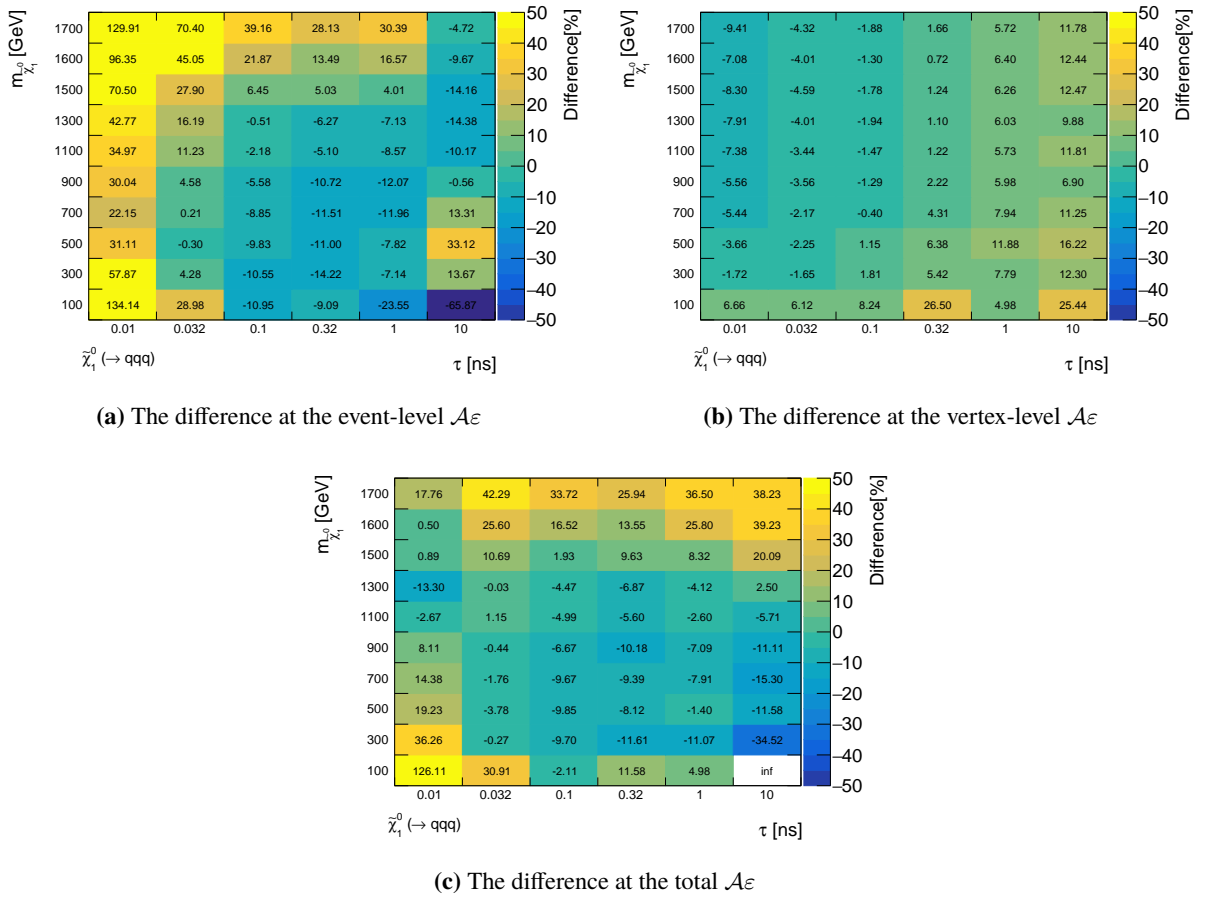


**Figure 10.11:** The value of the *difference* at the event-level, vertex-level, and total  $\mathcal{A}_\varepsilon$  in the Trackless SR for the signal scenarios of the direct electroweak production of pure higgsinos. The highest non-closure signal grid is the 100 GeV neutralino with a lifetime of 0.01 ns that has the difference of 126%, the Full Reco.  $\mathcal{A}_\varepsilon$  is 0.03% and the Param.  $\mathcal{A}_\varepsilon$  is 0.07%.



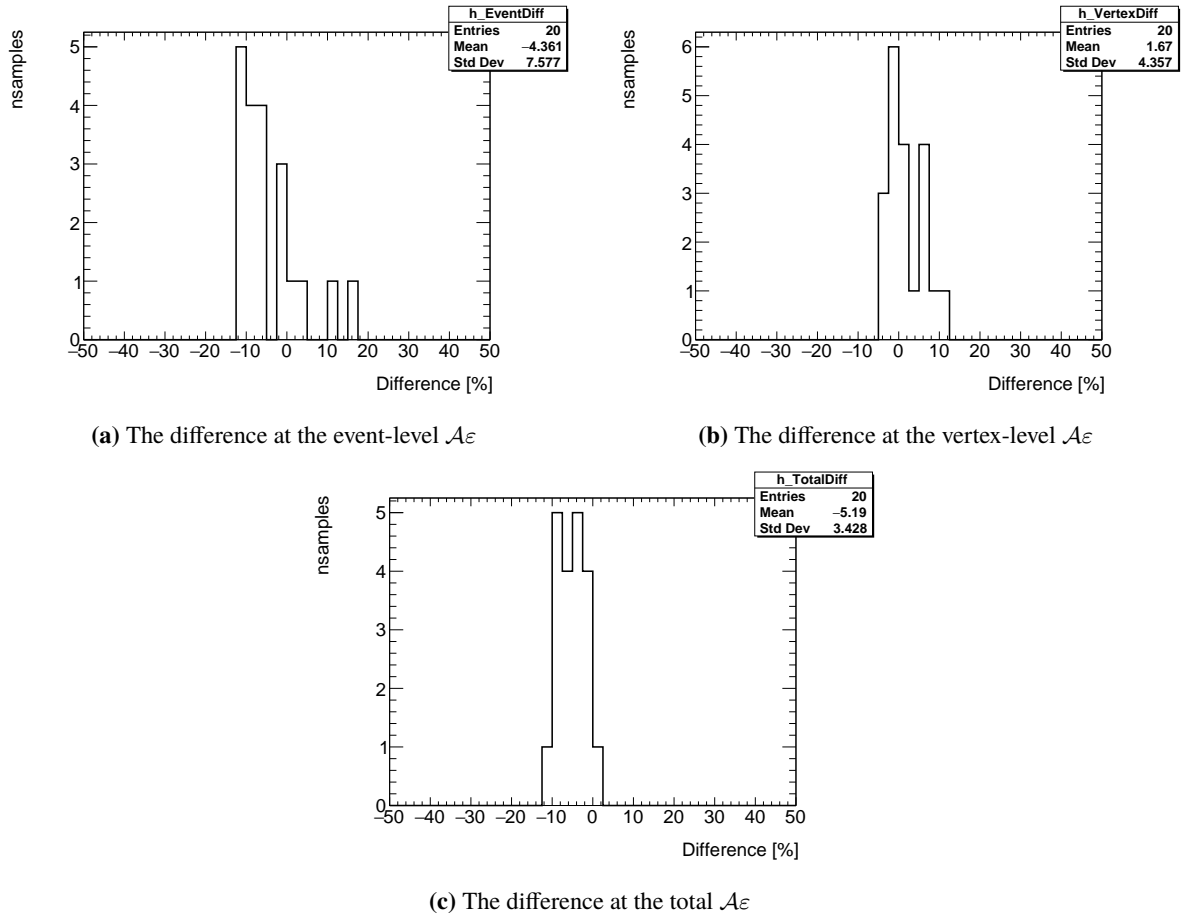


**Figure 10.12:** One dimensional histograms of the *difference* in Figure 10.11 for only signal grids with total Full Reco.  $\mathcal{A}\varepsilon$  larger than 10%.

# Chapter 11

## Conclusion

This thesis presents a search for long-lived SUSY particles in events with displaced vertices and multiple jets using the  $139 \text{ fb}^{-1}$  of  $pp$  collision data collected at  $\sqrt{s} = 13 \text{ TeV}$  by the ATLAS detector at the LHC. We focused on the SUSY model, which breaks  $R$ -parity with small coupling constant between SM and SUSY particles  $\lambda'' = O(10^{-4}) - O(10^{-3})$ . This model does not allow SUSY particles to be dark matter candidates, but keeps the benefits for the fine tuning problem of the Higgs boson mass and the grand unification. Two scenarios are searched for, which are the gluino pair production model ( $pp \rightarrow \tilde{g}\tilde{g}, \tilde{g} \rightarrow qq\tilde{\chi}_1^0 (\rightarrow qq\tilde{q})$ ) and the electrowikino pair production model ( $pp \rightarrow \tilde{\chi}_1^0\tilde{\chi}_1^\pm, \tilde{\chi}_1 \rightarrow qq\tilde{q}$ ). The lightest electrowikino has a long lifetime due to the small  $R$ -parity violating coupling.

These models are characterized by the inclusion of multiple jets and the decay vertex of the long-lived electrowikino being  $O(1)$ – $O(100)$  mm away from the interaction point, which are called displaced vertices. We established the analysis method using the dedicated techniques to reconstruct the tracks derived from the long-lived electrowikino decay and the decay vertex of the electrowikino. By using these techniques, the reconstruction efficiency for the decay vertex of the long-lived electrowikino with the flying distance within 300 mm is improved by up to 300%. Two SRs that require at least one displaced vertex and multiple jets are prepared. The first SR is called High- $p_T$  SR and targets the gluino pair production model, in which high momentum jets are formed by the decay of heavy gluino. The other SR is called Trackless SR and targets the case in which the low momentum jets are formed by the decay of light electrowikino in the electrowikino pair production model. Trackless SR requires an additional jet displaced from the interaction point derived from the neutralino decay in order to reduce the required momentum of the jets. The displaced vertex must be reconstructed from five or more tracks and the invariant mass calculated from the four-momenta of these tracks, assuming the pion mass, must be larger than 10 GeV.

The dominant background events are due to accidental reconstruction of displaced vertices by some sources. The displaced vertices are accidentally reconstructed by three main sources: interaction between particles and nuclei in the detector material, accidental crossing of unrelated tracks, and merging of vertices occurring close together. I established a new method to estimate background events inclusively using the correlation between the number of displaced vertices and the number of track jets and achieved accurate estimation.

The expected numbers of background events are  $0.46^{+0.27}_{-0.30}$  and  $0.83^{+0.51}_{-0.53}$  in the High- $p_T$  and Trackless SRs, respectively. There is no significant excess of data from the expected number of background events, with one and zero event passing the High- $p_T$  and Trackless SR requirements, respectively. These results are interpreted in targeted SUSY models. At 95% confidence level, the neutralino mass up to 1.58 TeV are excluded for lifetime of 0.1 ns, and the limit surpasses 1.5 TeV for all lifetimes in the range from 0.03 ns to 1 ns for the electrowikino pair production model. For the gluino pair production model, the neutralino lifetime up to 0.02 ns to 4 ns assuming the gluino mass of 2.4 TeV are excluded at 95% confidence level. The gluino mass up to 2600 GeV is excluded for the neutralino lifetime of 0.01 ns assuming the neutralino mass of 200 GeV. Upper limits on the visible cross section for any processes with the characteristics of displaced vertices and multiple jets are 0.03 fb and 0.02 fb in the High- $p_T$  and Trackless SRs, respectively.

The results of this search are the first results at the ATLAS experiment for SUSY particles with  $\lambda''$  couplings of  $O(10^{-4})$ – $O(10^{-3})$  magnitude. This analysis has enabled search in new phase spaces where SUSY particles are long-lived. Further search is expected with increased integrated luminosity and the inner detector upgrade in the HL-LHC ATLAS experiment. In addition, I established a reinterpretation method of this analysis using the only particle level information. This method allows those outside the ATLAS collaboration to reinterpret the results for any model predicting displaced vertices in multi-jet events. By reinterpreting various models, we can understand the phase space that has not been covered by the model-dependent searches so far, and develop a new specialized analysis for the discovery of BSM particles.

# Acknowledgments

This thesis could not have been completed without the support of many people and research grant such as JSPS KAKENHI and an operating grant from Nagoya University. I appreciate all people and research grant.

First of all, I would like to express my deepest gratitude to my supervisor, Makoto Tomoto. He supported me in many ways over the six years since I joined the N Lab, and thanks to him I was able to lead my research life comfortably. He also inspired me when my motivation was low due to the Covid-19 disaster, and thanks to him, I was able to work hard to the point of writing my doctoral thesis.

I would also like to express my deepest gratitude to Yu Nakahama for practically supervising me. She supported me in contacting the relevant people at the start of both my master's and doctoral researches to ensure that I could join the research team smoothly, and she also supported in ensuring that the research proceeded smoothly afterwards. I am also grateful for her advice and support, in terms of research, life at CERN and career. In addition, I would like to express my great appreciation for encouraging me to present our work at international conferences and important presentation opportunities at the ATLAS experiment. Presenting at such a big event was a very valuable experience in my life and will give me confidence for the future.

I would also like to express my gratitude to Christian Ohm, Simone Pagan Griso, Emily Anne Thompson, Federico Meloni, Giulia Ripellino, Stefan Richter, Karl Filip Backman, David Rousso, Yvonne Ng, and all of SUSY DV team members. They supported my analysis with many discussions. Thanks to them, I was able to contribute to the ATLAS paper made by the SUSY DV group.

I would also like to express my gratitude to Yasuyuki Horii, Yuya Kano, and all of N-ATLAS members. Discussions at the N-ATLAS meetings helped me to better understand and do improve my research.

I would also like to express my gratitude to Hideyuki Oide, Masahiro Morinaga, and all of ATLAS Japan BSM long-lived group members. The opportunity to have professional discussions in Japanese was useful and helped me to improve my research.

I would like to thank everyone at the N Lab, especially Toru Iijima and Kenji Inami, for organizing a wonderful lab. I would also like to thank my friends for their emotional support.

Finally, I would like to express my greatest gratitude to my family, who have always supported me spiritually and in life, as well as financially.

# References

- [1] STEPHEN P. MARTIN. A SUPERSYMMETRY PRIMER. In *Perspectives on Supersymmetry*, pages 1–98. WORLD SCIENTIFIC, jul 1998. URL: [https://doi.org/10.1142/2F9789812839657\\_0001](https://doi.org/10.1142/2F9789812839657_0001), doi:10.1142/9789812839657\_0001.
- [2] Christoph Borschensky, Michael Krämer, Anna Kulesza, Michelangelo Mangano, Sanjay Padhi, Tilman Plehn, and Xavier Portell. Squark and gluino production cross sections in pp collisions at  $\sqrt{s} = 13, 14, 33$  and 100 TeV. *Eur. Phys. J. C*, 74:3174, 2014. [arXiv:1407.5066](https://arxiv.org/abs/1407.5066), doi:10.1140/epjc/s10052-014-3174-y.
- [3] ATLAS Collaboration. SUSY March 2022 Summary Plot Update. ATL-PHYS-PUB-2022-013, 2022. URL: <https://cds.cern.ch/record/2805985>.
- [4] Super-Kamiokande Collaboration. Search for proton decay via  $p \rightarrow e^+\pi^0$  and  $p \rightarrow \mu^+\pi^0$  in 0.31 megaton · years exposure of the super-kamiokande water cherenkov detector. *Phys. Rev. D*, 95:012004, Jan 2017. URL: <https://link.aps.org/doi/10.1103/PhysRevD.95.012004>, doi:10.1103/PhysRevD.95.012004.
- [5] R. Barbier et al. R-parity violating supersymmetry. *Phys. Rept.*, 420:1–202, 2005. [arXiv:hep-ph/0406039](https://arxiv.org/abs/hep-ph/0406039), doi:10.1016/j.physrep.2005.08.006.
- [6] ATLAS Collaboration. Observation of a new particle in the search for the Standard Model Higgs boson with the ATLAS detector at the LHC. *Phys. Lett. B*, 716:1, 2012. [arXiv:1207.7214](https://arxiv.org/abs/1207.7214), doi:10.1016/j.physletb.2012.08.020.
- [7] CMS Collaboration. Observation of a new boson at a mass of 125 GeV with the CMS experiment at the LHC. *Phys. Lett. B*, 716:30, 2012. [arXiv:1207.7235](https://arxiv.org/abs/1207.7235), doi:10.1016/j.physletb.2012.08.021.
- [8] A.B. Arbuzov. Quantum Field Theory and the Electroweak Standard Model. (arXiv:1801.05670):1–34. 35 p, Jan 2018. 35 pages. doi:10.23730/CYRSP-2017-004.1.
- [9] Standard Model Summary Plots February 2022. Technical report, CERN, Geneva, 2022. All figures including auxiliary figures are available at <https://atlas.web.cern.ch/Atlas/GROUPS/PHYSICS/PUBNOTES/ATL-PHYS-PUB-2022-009>. URL: <https://cds.cern.ch/record/2804061>.
- [10] ATLAS and CMS Collaborations. Combined Measurement of the Higgs Boson Mass in  $pp$  Collisions at  $\sqrt{s} = 7$  and 8 TeV with the ATLAS and CMS Experiments. *Phys. Rev. Lett.*, 114:191803, 2015. [arXiv:1503.07589](https://arxiv.org/abs/1503.07589), doi:10.1103/PhysRevLett.114.191803.
- [11] C. N. Yang and R. L. Mills. Conservation of isotopic spin and isotopic gauge invariance. *Phys.*

- Rev., 96:191–195, Oct 1954. URL: <https://link.aps.org/doi/10.1103/PhysRev.96.191>, doi:10.1103/PhysRev.96.191.
- [12] R.D. Ball. Chiral gauge theory. *Phys. Rep.*, 182:1–186, 1989. URL: <https://www.sciencedirect.com/science/article/pii/0370157389900276>, doi:[https://doi.org/10.1016/0370-1573\(89\)90027-6](https://doi.org/10.1016/0370-1573(89)90027-6).
- [13] E. Corbelli and P. Salucci. The extended rotation curve and the dark matter halo of m33. *Monthly Notices of the Royal Astronomical Society*, 311(2):441–447, jan 2000. URL: <https://doi.org/10.1046%2Fj.1365-8711.2000.03075.x>, doi:10.1046/j.1365-8711.2000.03075.x.
- [14] N°7-2013: Planck reveals an almost perfect Universe. [https://www.esa.int/Newsroom/Press\\_Releases/Planck\\_reveals\\_an\\_almost\\_perfect\\_Universe](https://www.esa.int/Newsroom/Press_Releases/Planck_reveals_an_almost_perfect_Universe).
- [15] P. Serra, F. Zalamea, A. Cooray, G. Mangano, and A. Melchiorri. Constraints on neutrino – dark matter interactions from cosmic microwave background and large scale structure data. 2009. URL: <https://arxiv.org/abs/0911.4411>, doi:10.48550/ARXIV.0911.4411.
- [16] Y.A. Golfand and E.P. Likhtman. Extension of the Algebra of Poincare Group Generators and Violation of P Invariance. *JETP Lett.*, 13:323, 1971. [Pisma Zh. Eksp. Teor. Fiz. **13** (1971) 452].
- [17] D.V. Volkov and V.P. Akulov. Is the neutrino a goldstone particle? *Phys. Lett. B*, 46:109, 1973. doi:10.1016/0370-2693(73)90490-5.
- [18] J. Wess and B. Zumino. Supergauge transformations in four dimensions. *Nucl. Phys. B*, 70:39, 1974. doi:10.1016/0550-3213(74)90355-1.
- [19] J. Wess and B. Zumino. Supergauge invariant extension of quantum electrodynamics. *Nucl. Phys. B*, 78:1, 1974. doi:10.1016/0550-3213(74)90112-6.
- [20] S. Ferrara and B. Zumino. Supergauge invariant Yang-Mills theories. *Nucl. Phys. B*, 79:413, 1974. doi:10.1016/0550-3213(74)90559-8.
- [21] Abdus Salam and J. Strathdee. Super-symmetry and non-Abelian gauges. *Phys. Lett. B*, 51:353, 1974. doi:10.1016/0370-2693(74)90226-3.
- [22] Pierre Fayet. Supersymmetry and weak, electromagnetic and strong interactions. *Phys. Lett. B*, 64:159, 1976. doi:10.1016/0370-2693(76)90319-1.
- [23] Pierre Fayet. Spontaneously broken supersymmetric theories of weak, electromagnetic and strong interactions. *Phys. Lett. B*, 69:489, 1977. doi:10.1016/0370-2693(77)90852-8.
- [24] Looking for SUSY at the LHC. <https://www2.kek.jp/proffice/archives/feature/2010/SUSY.html>.
- [25] Ian J R Aitchison. Supersymmetry and the mssm: An elementary introduction, 2005. URL: <https://arxiv.org/abs/hep-ph/0505105>, doi:10.48550/ARXIV.HEP-PH/0505105.
- [26] ATLAS Collaboration. Reinterpretation of searches for supersymmetry in models with variable  $R$ -parity-violating coupling strength and long-lived  $R$ -hadrons. ATLAS-CONF-2018-003, 2018. URL: <https://cds.cern.ch/record/2308391>.
- [27] ATLAS Collaboration. Search for displaced vertices of oppositely charged leptons from decays

- of long-lived particles in  $pp$  collisions at  $\sqrt{s} = 13$  TeV with the ATLAS detector. *Phys. Lett. B*, 801:135114, 2020. [arXiv:1907.10037](#), [doi:10.1016/j.physletb.2019.135114](#).
- [28] ATLAS Collaboration. Search for long-lived, massive particles in events with a displaced vertex and a muon with large impact parameter in  $pp$  collisions at  $\sqrt{s} = 13$  TeV with the ATLAS detector. *Phys. Rev. D*, 102:032006, 2020. [arXiv:2003.11956](#), [doi:10.1103/PhysRevD.102.032006](#).
- [29] J.L. Goity and Marc Sher. Bounds on  $\delta b = 1$  couplings in the supersymmetric standard model. *Physics Letters B*, 346(1-2):69–74, 3 1995. [arXiv:hep-ph/9412208](#), [doi:10.1016/0370-2693\(94\)01688-9](#).
- [30] F. Zwirner. Observable  $\delta b = 2$  transitions without nucleon decay in a minimal supersymmetric extension of the standard model. *Physics Letters B*, 132(1):103–106, 1983. [doi:https://doi.org/10.1016/0370-2693\(83\)90230-7](#).
- [31] G.P. Salam. Elements of qcd for hadron colliders. *Vol. 5 (2020): Proceedings of the 2018 Asia–Europe–Pacific School of High-Energy Physics, Quy Nhon, Vietnam, 12–25 September 2018*. [doi:https://doi.org/10.23730/CYRSP-2020-005.1](#).
- [32] Richard D. Ball, Valerio Bertone, Stefano Carrazza, Luigi Del Debbio, Stefano Forte, Patrick Groth-Merrild, Alberto Guffanti, Nathan P. Hartland, Zahari Kassabov, JoséI. Latorre, Emanuele R. Nocera, Juan Rojo, Luca Rottoli, Emma Slade, and Maria Ubiali. Parton distributions from high-precision collider data. *The European Physical Journal C*, 77:663, 2017. [doi:10.1140/epjc/s10052-017-5199-5](#).
- [33] Lyndon Evans and Philip Bryant. LHC Machine. *JINST*, 3:S08001, 2008. [doi:10.1088/1748-0221/3/08/S08001](#).
- [34] Cinzia De Melis. The CERN accelerator complex. Complexe des accélérateurs du CERN. 2016. General Photo. URL: <https://cds.cern.ch/record/2119882>.
- [35] Joao Pequeno. Computer generated image of the whole ATLAS detector. 2008. URL: <https://cds.cern.ch/record/1095924>.
- [36] Joao Pequeno and Paul Schaffner. How ATLAS detects particles: diagram of particle paths in the detector. 2013. URL: <https://cds.cern.ch/record/1505342>.
- [37] A. Yamamoto, Y. Makida, and R. Ruber et al. The atlas central solenoid. *Nuclear Instruments and Methods in Physics Research Section A: Accelerators, Spectrometers, Detectors and Associated Equipment*, 584(1):53 – 74, 2008. URL: <http://www.sciencedirect.com/science/article/pii/S0168900207020414>, [doi:https://doi.org/10.1016/j.nima.2007.09.047](#).
- [38] ATLAS Collaboration. The ATLAS Experiment at the CERN Large Hadron Collider. *JINST*, 3:S08003, 2008. [doi:10.1088/1748-0221/3/08/S08003](#).
- [39] ATLAS Collaboration. ATLAS Insertable B-Layer: Technical Design Report, 2010. URL: <https://cds.cern.ch/record/1291633>.
- [40] ATLAS Collaboration. Track Reconstruction Performance of the ATLAS Inner Detector at  $\sqrt{s} =$

- 13 TeV. ATL-PHYS-PUB-2015-018, 2015. URL: <https://cds.cern.ch/record/2037683>.
- [41] ATLAS Collaboration. Study of the material of the ATLAS inner detector for Run 2 of the LHC. *JINST*, 12:P12009, 2017. [arXiv:1707.02826](https://arxiv.org/abs/1707.02826), doi:[10.1088/1748-0221/12/12/P12009](https://doi.org/10.1088/1748-0221/12/12/P12009).
- [42] The Inner Detector. <https://atlas.cern/discover/detector/inner-detector>.
- [43] ApprovedPlotsDAQ. <https://twiki.cern.ch/twiki/bin/view/AtlasPublic/ApprovedPlotsDAQ>.
- [44] ATLAS Collaboration. The new LUCID-2 detector for luminosity measurement and monitoring in ATLAS. *JINST*, 13:P07017, 2018. doi:[10.1088/1748-0221/13/07/P07017](https://doi.org/10.1088/1748-0221/13/07/P07017).
- [45] ATLAS collaboration. Public ATLAS Luminosity Results for Run-2 of the LHC. <https://twiki.cern.ch/twiki/bin/view/AtlasPublic/LuminosityPublicResultsRun2>.
- [46] ATLAS Collaboration. The Pythia 8 A3 tune description of ATLAS minimum bias and inelastic measurements incorporating the Donnachie–Landshoff diffractive model. ATL-PHYS-PUB-2016-017, 2016. URL: <https://cds.cern.ch/record/2206965>.
- [47] A. D. Martin, W. J. Stirling, R. S. Thorne, and G. Watt. Parton distributions for the LHC. *Eur. Phys. J. C*, 63:189, 2009. [arXiv:0901.0002](https://arxiv.org/abs/0901.0002), doi:[10.1140/epjc/s10052-009-1072-5](https://doi.org/10.1140/epjc/s10052-009-1072-5).
- [48] ATLAS Collaboration. The ATLAS Simulation Infrastructure. *Eur. Phys. J. C*, 70:823, 2010. [arXiv:1005.4568](https://arxiv.org/abs/1005.4568), doi:[10.1140/epjc/s10052-010-1429-9](https://doi.org/10.1140/epjc/s10052-010-1429-9).
- [49] GEANT4 Collaboration, S. Agostinelli, et al. GEANT4 – a simulation toolkit. *Nucl. Instrum. Meth. A*, 506:250, 2003. doi:[10.1016/S0168-9002\(03\)01368-8](https://doi.org/10.1016/S0168-9002(03)01368-8).
- [50] J. Alwall, R. Frederix, S. Frixione, V. Hirschi, F. Maltoni, O. Mattelaer, H. S. Shao, T. Stelzer, P. Torrielli, and M. Zaro. The automated computation of tree-level and next-to-leading order differential cross sections, and their matching to parton shower simulations. *JHEP*, 07:079, 2014. [arXiv:1405.0301](https://arxiv.org/abs/1405.0301), doi:[10.1007/JHEP07\(2014\)079](https://doi.org/10.1007/JHEP07(2014)079).
- [51] Torbjörn Sjöstrand, Stefan Ask, Jesper R. Christiansen, Richard Corke, Nishita Desai, Philip Ilten, Stephen Mrenna, Stefan Prestel, Christine O. Rasmussen, and Peter Z. Skands. An introduction to PYTHIA 8.2. *Comput. Phys. Commun.*, 191:159, 2015. [arXiv:1410.3012](https://arxiv.org/abs/1410.3012), doi:[10.1016/j.cpc.2015.01.024](https://doi.org/10.1016/j.cpc.2015.01.024).
- [52] Richard D. Ball et al. Parton distributions with LHC data. *Nucl. Phys. B*, 867:244, 2013. [arXiv:1207.1303](https://arxiv.org/abs/1207.1303), doi:[10.1016/j.nuclphysb.2012.10.003](https://doi.org/10.1016/j.nuclphysb.2012.10.003).
- [53] ATLAS Collaboration. ATLAS Pythia 8 tunes to 7 TeV data. ATL-PHYS-PUB-2014-021, 2014. URL: <https://cds.cern.ch/record/1966419>.
- [54] Leif Lönnblad. Correcting the Colour-Dipole Cascade Model with Fixed Order Matrix Elements. *JHEP*, 05:046, 2002. [arXiv:hep-ph/0112284](https://arxiv.org/abs/hep-ph/0112284), doi:[10.1088/1126-6708/2002/05/046](https://doi.org/10.1088/1126-6708/2002/05/046).
- [55] Leif Lönnblad and Stefan Prestel. Matching tree-level matrix elements with interleaved showers. *JHEP*, 03:019, 2012. [arXiv:1109.4829](https://arxiv.org/abs/1109.4829), doi:[10.1007/JHEP03\(2012\)019](https://doi.org/10.1007/JHEP03(2012)019).
- [56] Wim Beenakker, Christoph Borschensky, Michael Krämer, Anna Kulesza, and Eric Laenen. NNLL-fast: predictions for coloured supersymmetric particle production at the LHC with threshold and Coulomb resummation. *JHEP*, 12:133, 2016. [arXiv:1607.07741](https://arxiv.org/abs/1607.07741), doi:[10.1007/JHEP12\(2016\)133](https://doi.org/10.1007/JHEP12(2016)133).



- 1007/JHEP12(2016)133.
- [57] Wim Beenakker, Christoph Borschensky, Michael Krämer, Anna Kulesza, Eric Laenen, Vincent Theeuwes, and Silja Thewes. NNLL resummation for squark and gluino production at the LHC. *JHEP*, 12:023, 2014. [arXiv:1404.3134](#), [doi:10.1007/JHEP12\(2014\)023](#).
- [58] Wim Beenakker, Tim Janssen, Susanne Lepoeter, Michael Krämer, Anna Kulesza, Eric Laenen, Irene Niessen, Silja Thewes, and Tom Van Daal. Towards NNLL resummation: hard matching coefficients for squark and gluino hadroproduction. *JHEP*, 10:120, 2013. [arXiv:1304.6354](#), [doi:10.1007/JHEP10\(2013\)120](#).
- [59] Wim Beenakker, Silja Brensing, Michael Krämer, Anna Kulesza, Eric Laenen, and Irene Niessen. NNLL resummation for squark-antisquark pair production at the LHC. *JHEP*, 01:076, 2012. [arXiv:1110.2446](#), [doi:10.1007/JHEP01\(2012\)076](#).
- [60] Wim Beenakker, Silja Brensing, Michael Krämer, Anna Kulesza, Eric Laenen, and Irene Niessen. Soft-gluon resummation for squark and gluino hadroproduction. *JHEP*, 12:041, 2009. [arXiv:0909.4418](#), [doi:10.1088/1126-6708/2009/12/041](#).
- [61] A. Kulesza and L. Motyka. Soft gluon resummation for the production of gluino-gluino and squark-antisquark pairs at the LHC. *Phys. Rev. D*, 80:095004, 2009. [arXiv:0905.4749](#), [doi:10.1103/PhysRevD.80.095004](#).
- [62] A. Kulesza and L. Motyka. Threshold Resummation for Squark-Antisquark and Gluino-Pair Production at the LHC. *Phys. Rev. Lett.*, 102:111802, 2009. [arXiv:0807.2405](#), [doi:10.1103/PhysRevLett.102.111802](#).
- [63] W. Beenakker, R. Höpker, M. Spira, and P.M. Zerwas. Squark and gluino production at hadron colliders. *Nucl. Phys. B*, 492:51, 1997. [arXiv:hep-ph/9610490](#), [doi:10.1016/S0550-3213\(97\)00084-9](#).
- [64] Jon Butterworth et al. PDF4LHC recommendations for LHC Run II. *J. Phys. G*, 43:023001, 2016. [arXiv:1510.03865](#), [doi:10.1088/0954-3899/43/2/023001](#).
- [65] W. Beenakker et al. Production of Charginos, Neutralinos, and Stopped at Hadron Colliders. *Phys. Rev. Lett.*, 83:3780, 1999. [arXiv:hep-ph/9906298](#), [doi:10.1103/PhysRevLett.83.3780](#).
- [66] Jonathan Debove, Benjamin Fuks, and Michael Klasen. Threshold resummation for gaugino pair production at hadron colliders. *Nucl. Phys. B*, 842:51, 2011. [arXiv:1005.2909](#), [doi:10.1016/j.nuclphysb.2010.08.016](#).
- [67] Benjamin Fuks, Michael Klasen, David R. Lamprea, and Marcel Rothering. Gaugino production in proton-proton collisions at a center-of-mass energy of 8 TeV. *JHEP*, 10:081, 2012. [arXiv:1207.2159](#), [doi:10.1007/JHEP10\(2012\)081](#).
- [68] Benjamin Fuks, Michael Klasen, David R. Lamprea, and Marcel Rothering. Precision predictions for electroweak superpartner production at hadron colliders with RESUMINO. *Eur. Phys. J. C*, 73:2480, 2013. [arXiv:1304.0790](#), [doi:10.1140/epjc/s10052-013-2480-0](#).
- [69] Juri Fiaschi and Michael Klasen. Neutralino-chargino pair production at NLO+NLL with

- resummation-improved parton density functions for LHC Run II. *Phys. Rev. D*, 98(5):055014, 2018. [arXiv:1805.11322](#), [doi:10.1103/PhysRevD.98.055014](#).
- [70] ATLAS Collaboration. Performance of the ATLAS Silicon Pattern Recognition Algorithm in Data and Simulation at  $\sqrt{s} = 7$  TeV. ATLAS-CONF-2010-072, 2010. URL: <https://cds.cern.ch/record/1281363>.
- [71] R. Fruhwirth. Application of kalman filtering to track and vertex fitting. *Nuclear Instruments and Methods in Physics Research Section A: Accelerators, Spectrometers, Detectors and Associated Equipment*, 262:444–450, 1987. [doi:https://doi.org/10.1016/0168-9002\(87\)90887-4](#).
- [72] ATLAS Collaboration. The Optimization of ATLAS Track Reconstruction in Dense Environments. ATL-PHYS-PUB-2015-006, 2015. URL: <https://cds.cern.ch/record/2002609>.
- [73] S Boutle and D Casper and B Hooberman and K Grimm and B Gui and G Lee and J Maurer and A Morley and S Pagan Griso and B Petersen and K Prokofiev and L Shan and D Shope and A Wharton and B Whitmore and M Zhang and on behalf of the ATLAS Collaboration. Primary vertex reconstruction at the ATLAS experiment. *Journal of Physics: Conference Series*, 898:042056, 2017. [doi:10.1088/1742-6596/898/4/042056](#).
- [74] ATLAS Collaboration. Performance of the reconstruction of large impact parameter tracks in the inner detector of ATLAS. ATL-PHYS-PUB-2017-014, 2017. URL: <https://cds.cern.ch/record/2275635>.
- [75] Jackson Carl Burzynski. Improved Track Reconstruction Performance for Long-lived Particles in ATLAS. Technical report, CERN, Geneva, 2022. URL: <https://cds.cern.ch/record/2815527>.
- [76] ATLAS Collaboration. Performance of vertex reconstruction algorithms for detection of new long-lived particle decays within the ATLAS inner detector. ATL-PHYS-PUB-2019-013, 2019. URL: <https://cds.cern.ch/record/2669425>.
- [77] ATLAS Collaboration. Electron reconstruction and identification in the ATLAS experiment using the 2015 and 2016 LHC proton–proton collision data at  $\sqrt{s} = 13$  TeV. *Eur. Phys. J. C*, 79:639, 2019. [arXiv:1902.04655](#), [doi:10.1140/epjc/s10052-019-7140-6](#).
- [78] ATLAS Collaboration. Muon reconstruction and identification efficiency in ATLAS using the full Run 2  $pp$  collision data set at  $\sqrt{s} = 13$  TeV. *Eur. Phys. J. C*, 81:578, 2021. [doi:10.1140/epjc/s10052-021-09233-2](#).
- [79] Matteo Cacciari, Gavin P. Salam, and Gregory Soyez. The anti- $k_t$  jet clustering algorithm. *JHEP*, 04:063, 2008. [arXiv:0802.1189](#), [doi:10.1088/1126-6708/2008/04/063](#).
- [80] ATLAS Collaboration. Properties of jets and inputs to jet reconstruction and calibration with the ATLAS detector using proton–proton collisions at  $\sqrt{s} = 13$  TeV. ATL-PHYS-PUB-2015-036, 2015. URL: <https://cds.cern.ch/record/2044564>.
- [81] ATLAS Collaboration. Jet energy scale and resolution measured in proton–proton collisions at  $\sqrt{s} = 13$  TeV with the ATLAS detector. *Eur. Phys. J. C*, 81:689, 2020. [arXiv:2007.02645](#),

- doi:[10.1140/epjc/s10052-021-09402-3](https://doi.org/10.1140/epjc/s10052-021-09402-3).
- [82] ATLAS Collaboration. Selection of jets produced in 13 TeV proton–proton collisions with the ATLAS detector. ATLAS-CONF-2015-029, 2015. URL: <https://cds.cern.ch/record/2037702>.
- [83] ATLAS Collaboration. Jet energy scale measurements and their systematic uncertainties in proton–proton collisions at  $\sqrt{s} = 13$  TeV with the ATLAS detector. *Phys. Rev. D*, 96:072002, 2017. [arXiv:1703.09665](https://arxiv.org/abs/1703.09665), doi:[10.1103/PhysRevD.96.072002](https://doi.org/10.1103/PhysRevD.96.072002).
- [84] ATLAS Collaboration. 2015 start-up trigger menu and initial performance assessment of the ATLAS trigger using Run-2 data. ATL-DAQ-PUB-2016-001, 2016. URL: <https://cds.cern.ch/record/2136007>.
- [85] ATLAS Collaboration. Trigger Menu in 2016. ATL-DAQ-PUB-2017-001, 2017. URL: <https://cds.cern.ch/record/2242069>.
- [86] ATLAS Collaboration. Trigger Menu in 2017. ATL-DAQ-PUB-2018-002, 2018. URL: <https://cds.cern.ch/record/2625986>.
- [87] ATLAS Collaboration. Early Inner Detector Tracking Performance in the 2015 Data at  $\sqrt{s} = 13$  TeV. ATL-PHYS-PUB-2015-051, 2015. URL: <https://cds.cern.ch/record/2110140>.
- [88] LHC SUSY Cross Sections Working Group. Susy cross sections and uncertainties. URL: <https://twiki.cern.ch/twiki/bin/view/LHCPhysics/SUSYCrossSections>.
- [89] Alexander L. Read. Presentation of search results: the  $CL_S$  technique. *J. Phys. G*, 28:2693, 2002. doi:[10.1088/0954-3899/28/10/313](https://doi.org/10.1088/0954-3899/28/10/313).
- [90] Lukas Heinrich, Matthew Feickert, Giordon Stark, and Kyle Cranmer. pyhf: pure-python implementation of histfactory statistical models. *Journal of Open Source Software*, 6(58):2823, 2021. doi:[10.21105/joss.02823](https://doi.org/10.21105/joss.02823).
- [91] Glen Cowan, Kyle Cranmer, Eilam Gross, and Ofer Vitells. Asymptotic formulae for likelihood-based tests of new physics. *The European Physical Journal C*, 71(2), 2 2011. URL: <https://doi.org/10.1140/epjc/s10052-011-1554-0>, doi:[10.1140/epjc/s10052-011-1554-0](https://doi.org/10.1140/epjc/s10052-011-1554-0).
- [92] Technical Design Report for the ATLAS Inner Tracker Strip Detector. Technical report, CERN, Geneva, 2017. URL: <https://cds.cern.ch/record/2257755>.